# A MATHEMATICAL MODEL OF BLOOD COAGULATION AND PLATELET DEPOSITION UNDER FLOW

by

Karin Leiderman Gregg

A dissertation submitted to the faculty of
The University of Utah
in partial fulfillment of the requirements for the degree of

Doctor of Philosophy

Department of Mathematics

The University of Utah

December 2010

**The University of Utah Graduate School**

# STATEMENT OF DISSERTATION APPROVAL

The dissertation of **Karin Leiderman**

has been approved by the following supervisory committee members:

| | | |
|---|---|---|
| **Aaron L.** , Chair | **6/26/2010** Date Approved |
| **James P. Keener** , Member | **6/26/2010** Date Approved |
| **Robert D.** , Member | **6/26/2010** Date Approved |
| **Robert M.** , Member | **6/26/2010** Date Approved |
| **Alisa** , Member | **6/26/2010** Date Approved |

and by

the Department of **Mathematics**

and by Charles A. Wight, Dean of The Graduate School.

# ABSTRACT

The body responds to vascular injury with two intertwined processes: platelet aggregation and coagulation. Platelet aggregation is a predominantly physical process, whereby platelets clump together, and coagulation is a cascade of biochemical enzyme reactions. Thrombin, the major product of coagulation, directly couples the biochemical system to platelet aggregation by activating platelets and by cleaving fibrinogen into fibrin monomers that polymerize to form a mesh that stabilizes platelet aggregates. Transport of coagulation proteins and platelets to and from an injury is controlled largely by the dynamics of the blood flow. To explore how blood flow affects the growth of thrombi and how the growing masses, in turn, feed back and affect the flow, we have developed the first spatial-temporal mathematical model of platelet aggregation and blood coagulation under flow that includes detailed descriptions of coagulation biochemistry, chemical activation and deposition of blood platelets, as well as the two-way interaction between the fluid dynamics and the growing platelet mass. We present this model and use it to explain what underlies the threshold behavior of the coagulation systems production of thrombin and to show how wall shear rate and near-wall enhanced platelet concentrations affect the development of growing thrombi. By accounting for the porous nature of the thrombus, we also demonstrate how advective and diffusive transport to and within the thrombus affects its growth at different stages and spatial locations.

We also present a modification of this model in which flow is removed. This is so we may replicate results from cell-based experiments. This set-up allows for the systematic examination of the effect of individual procoagulant proteins on thrombin production. We highlight the qualitative agreement of our results with those from the experiments.

To my husband, Benjamin, and my family
for their tireless love and support.

# CONTENTS

**ABSTRACT** . . . . . **iii**

**LIST OF TABLES** . . . . . **vii**

**ACKNOWLEDGEMENTS** . . . . . **viii**

**CHAPTERS**

**1. INTRODUCTION** . . . . . **1**

1.1 The Clotting System . . . . . 2
1.2 Previous Models . . . . . 5

**2. MODEL** . . . . . **8**

2.1 Fluid . . . . . 9
2.2 Platelets . . . . . 10
2.3 Platelet-bound Chemical Species . . . . . 13
2.4 Subendothelium-bound Chemical Species . . . . . 14
2.5 Fluid-phase Chemical Species . . . . . 14
2.5.1 ADP . . . . . 16
2.6 Near-Wall Excess of Platelets . . . . . 16

**3. MODEL RESULTS** . . . . . **18**

3.1 Thrombin Production Dependence on Tissue Factor Density . . . . . 19
3.2 Thrombus Growth Dependence on Wall Shear Rate and Near-Wall Excess of Platelets . . . . . 24
3.3 Platelet Activation by Chemical Agonists . . . . . 29
3.4 Porosity and Intrathrombus Transport . . . . . 31
3.5 Flow Boundary Conditions . . . . . 40
3.6 Limitations and Extensions . . . . . 40

**4. ACCOUNTING FOR THE FINITE SIZE OF PLATELETS** . . . . . **42**

4.1 The Spatial Parameter $k_{adh}(\mathbf{x})$ . . . . . 42
4.2 Three Forms of $W(\phi^T)$ . . . . . 43
4.3 Platelet-Platelet Cohesion: $k_{coh}$ and $g(\eta)$ . . . . . 45

**5. LONGER VESSEL EXPERIMENTS** . . . . . **49**

5.1 Two Thrombi . . . . . 49
5.2 Activated Protein C and the Endothelium . . . . . 53
5.2.1 Model Extension . . . . . 53
5.2.2 Results . . . . . 55
5.2.3 Discussion . . . . . 57

**6. STIRRING MODEL** . . . . . **59**
6.1 Physical Experiments and Results . . . . . 59
6.2 Mathematical Model . . . . . 61
6.2.1 Algorithm . . . . . 65
6.2.2 Equations and Parameters . . . . . 66
6.3 Comparing Model to Experiment . . . . . 68
6.4 Discussion . . . . . 72

**7. NUMERICAL METHODS** . . . . . **75**
7.1 Projection Method for Fluid Equations . . . . . 76
7.1.1 SOR . . . . . 80
7.1.2 Multigrid . . . . . 81
7.2 Mobile Chemical Species . . . . . 82
7.2.1 Advection Equation . . . . . 82
7.2.2 Diffusion Equation . . . . . 85
7.2.3 Reaction Equation . . . . . 87
7.3 Mobile Platelets . . . . . 87
7.3.1 Mobile Platelet Advection . . . . . 88
7.3.2 Mobile Platelet Diffusion . . . . . 89
7.4 Convergence Study . . . . . 89

**8. FUTURE DIRECTIONS** . . . . . **94**
8.1 New Platelet Species . . . . . 94
8.1.1 Bound Unactivated Platelets, $P^{b,u}$ . . . . . 95
8.1.2 ADP-Activated Platelets, $P^{m,adp}$ and $P^{b,adp}$ . . . . . 95
8.1.3 Changes to old equations . . . . . 96
8.2 A Simpler Model for Shear Rate-Dependent Cohesion . . . . . 97
8.3 Platelet-Density-Dependent Diffusion . . . . . 99

**APPENDIX: MODEL EQUATIONS AND PARAMETERS** . . . . . **102**

**REFERENCES** . . . . . **117**

# LIST OF TABLES

2.1 Descriptions of selected model variables and parameters. . . . . 9

6.1 Amount or concentration of components used in the cell-based model. . . . . 60

6.2 Area under the thrombin concentration curve and total thrombin produced for variations in concentration of plasma factors VIII and IX. . . . . 69

6.3 Area under the thrombin concentration curve and total thrombin produced for variations in concentration of prothrombin and plasma factor V. . . . . 71

6.4 Area under the thrombin concentration curve and total thrombin produced for variations in concentration of plasma factor X. . . . . 73

A.1 Diffusion coefficients for platelets and mobile chemical species. . . . . 109

A.2 Normal concentrations and surface binding site numbers. . . . . 110

A.3 Reactions of subendothelium. . . . . 111

A.4 Reactions in the plasma. . . . . 112

A.5 Binding to platelet surfaces. . . . . 113

A.6 Reactions of platelet surfaces. . . . . 114

A.7 Inhibition reactions. . . . . 115

A.8 Platelet transitions. . . . . 116

# ACKNOWLEDGEMENTS

First, I would like to acknowledge my entire committee, Aaron Fogelson, James Keener, Robert Guy, Mike Kirby, and Alisa Wolberg for meaningful discussions, reading my thesis, asking questions and making me explain things, and for giving me valuable feedback. Thanks to the National Science Foundation for funding my work through the following grants: NSF DGE-0217424, DMS-0354259 and DMS-0540779.

The accomplishment of this thesis would not have been possible without the support and direction of my advisor, Aaron Fogelson. I am extremely grateful to him for always opening his door to me, considering my ideas and listening to my concerns. For the countless discussions about interesting science and mathematics; thanks for making work so much more fun! I only hope that in the future I may provide students with the same encouragement, professionalism, and guidance that Aaron has given to me.

I would like to thank James Keener for keeping the University of Utah Mathematical Biology group alive with his constant and contagious excitement for mathematics. My time as a graduate student in Utah would not have been the same without his graduate program vision, group meetings, and of course, cabin parties.

I also want to thank Robert Guy for being a wonderful mentor and role model. At his office door, no matter what the question, Bob always greeted me with a welcoming smile. His light-hearted approach to work and life is admirable and helped me through many frustrating times as a graduate student.

Special thanks to Laura Miller for being a truly inspirational woman, scientist, mathematician, friend and role model. Without her, I may not have made it this far.

To my girls! Lindsay, Courtney, Liz, and Nessy. Where would we all be without each other? Words cannot express how important these amazing women have been in my life. I deeply thank them for their support, encouragement, laughter, and love!

A bottom-of-my-heart thanks to my husband and my family who have been there for me through it all; through every struggle, every tear, and every accomplishment. They gave me the work ethic I needed to survive graduate school but also helped me to enjoy life and find happiness outside of work.

# CHAPTER 1

# INTRODUCTION

The hemostatic system, which consists of coagulation, platelet aggregation and fibrinolysis, is responsible for healing injured blood vessels and preventing bleeding. This system responds to vascular damage with multiple interactions between blood vessel walls, circulating blood platelets and the clotting factors inherent to the coagulation reactions. The response consists of formation of a blood clot at the injury to prevent excessive bleeding, followed by break-down of the clot (fibrinolysis) to avoid vessel occlusion. The hemostatic interactions, although numerous and complex, must localize to the site of injury while in a dynamic fluid environment. The flowing blood regulates the rate at which blood-borne components (clotting factors and cells) are delivered to the injury site and also the rate at which they leave. Clotting factors and platelets become 'procoagulant' at the injury site in order to form a thrombus, but if they leave the injury site in this same activated state, they may trigger unnecessary procoagulant events away from the injury. The normal balance of hemostasis is delicate and may falter due to certain blood pathologies or disorders, surgical procedures or massive injuries. One side of the imbalance could lead to persistent bleeding and hemorrhage, while the other could give rise to thrombosis with possible vessel occlusion.

The clotting interactions are extremely complex and multiple temporal and spatial scales are important in them and these features make it very difficult, using traditional experimental approaches alone, to piece together a quantitative picture of how the system as a whole functions. For example, in order to further some coagulation reactions that take place on active, phospholipid membranes, chemicals must be transported through a moving fluid, between distinct geographical locations. A question which has, in part, motivated this work is: how does flow affect the growth of a thrombus, and how does this thrombus growth, in turn, affect the surrounding and intrathrombus fluid environment? In this dissertation, we present a mathematical model aimed at integrating together the knowledge obtained from laboratory experimentation to develop a quantitative understanding of how the many

pieces of the clotting system function together, and, ultimately, to develop the ability to make accurate quantitative predictions of this behavior under flow.

Although hemostasis involves both the formation and dissolution of blood clots, the content of this dissertation focuses on formation of a thrombus. The rest of this chapter consists of a biological overview of the clotting system and a brief review of previous mathematical models of portions of this system. In Chapter 2, we describe in detail a spatial-temporal model and the formulation of its equations. In Chapter 3, we present results and hypotheses derived from this model followed by a short discussion. In Chapter 4, we explain how we account for the finite size of the platelets in a continuum model. Chapters 5 and 6 contain two different model extensions, each with results and discussions. Chapter 7 contains a description of the numerical methods used to solve the equations in the spatial-temporal model and the results of the convergence studies. Finally, in Chapter 8, we briefly describe the future directions of this research.

## 1.1 The Clotting System

Healthy blood vessel walls are lined with a single layer of endothelial cells that act as an anticoagulant surface; normal, unactivated endothelial cells do not support coagulation reactions on their surface, and blood platelets do not adhere to them. When this layer of cells is disrupted or removed as in the event of a vascular injury, the normal anticoagulant behavior is lost and the coagulation response is initiated. Tissue factor (TF), a membrane protein embedded in the subendothelium beneath the endothelial cells, is thought to be responsible for initiating this process [53]. A tissue factor molecule acts as receptor and cofactor for clotting factor VII (FVII) which once bound to TF, may become activated to catalyze the activation of two other clotting factors. The two clotting factors activated by the TF:FVIIa complex, FIX, and FX are extremely important to further coagulation reactions, as described below.

Circulating blood platelets may directly bind to collagen, another molecule embedded in the subendothelium. When platelets adhere to collagen they become activated and undergo a number of important changes: their physical shape changes, they secrete chemical agonists that partially activate neighboring platelets, and they expose or activate receptors bound to their surface. These receptors are important in that some provide a localized reactive surface that supports many of the coagulation reactions and others support the mechanism by which platelets cohere with one another and aggregate. The exposed subendothelium

together with adhered, partially-activated platelets create the necessary ingredients for small amounts of thrombin production (the key enzyme and final product of coagulation). Thrombin is a potent activator of platelets and thrombin-activated platelets have increased procoagulant activity compared to that of platelets partially-activated by collagen [3] or by their own secreted chemical agonists. Thrombin also acts on the plasma protein fibrinogen to produce fibrin monomers which polymerize in a process that leads to a stabilizing fibrin gel within and surrounding the platelet aggregates.

The two subprocesses of hemostasis and thrombosis, platelet aggregation and blood coagulation, are intertwined. A schematic is given in Fig. 1.1, and a detailed discussion of the reactions and interactions can be found in [38]. Excellent reviews can be found in [27, 32, 47]. Here, we outline the salient features of the coagulation and platelet deposition processes as incorporated in our model. We use the following abbreviations: TF, tissue factor; APC, activated protein C; TFPI, tissue factor pathway inhibitor; ADP, adenosine diphosphate; ATIII, antithrombin-III.

- Each of the coagulation proteins has an inactive and an active form. The inactive zymogens are factors VII, IX, X, and II (prothrombin) and have corresponding active enzymes factors VIIa, IXa, Xa, and IIa (thrombin), respectively. The inactive/active cofactor pairs are factors V and Va, and factors VIII and VIIIa.

- Three enzyme complexes play major parts in coagulation, the tissue factor complex on the subendothelium (TF:VIIa) and the tenase (VIIIa:IXa) and prothrombinase (Va:Xa) complexes on the surface of activated platelets. In these complexes, a cofactor TF, VIIIa or Va helps to increase tremendously the catalytic effectiveness of the corresponding enzyme (VIIa, IXa and Xa, respectively) compared to that of the same enzyme molecule without its cofactor.

- The reactions are initiated when VIIa binds to TF molecules exposed to the blood by the injury. The complex TF:VIIa activates zymogens IX and X to enzymes IXa and Xa, respectively. Each of these enzymes can become part of an enzyme complex on the surface of an activated platelet. For these complexes to form, there must be activated platelets nearby, the enzymes must make their way through the fluid from the subendothelial surface to the surface of one of the activated platelets, and the active cofactor molecules, VIIIa and Va, must be available and bound to that

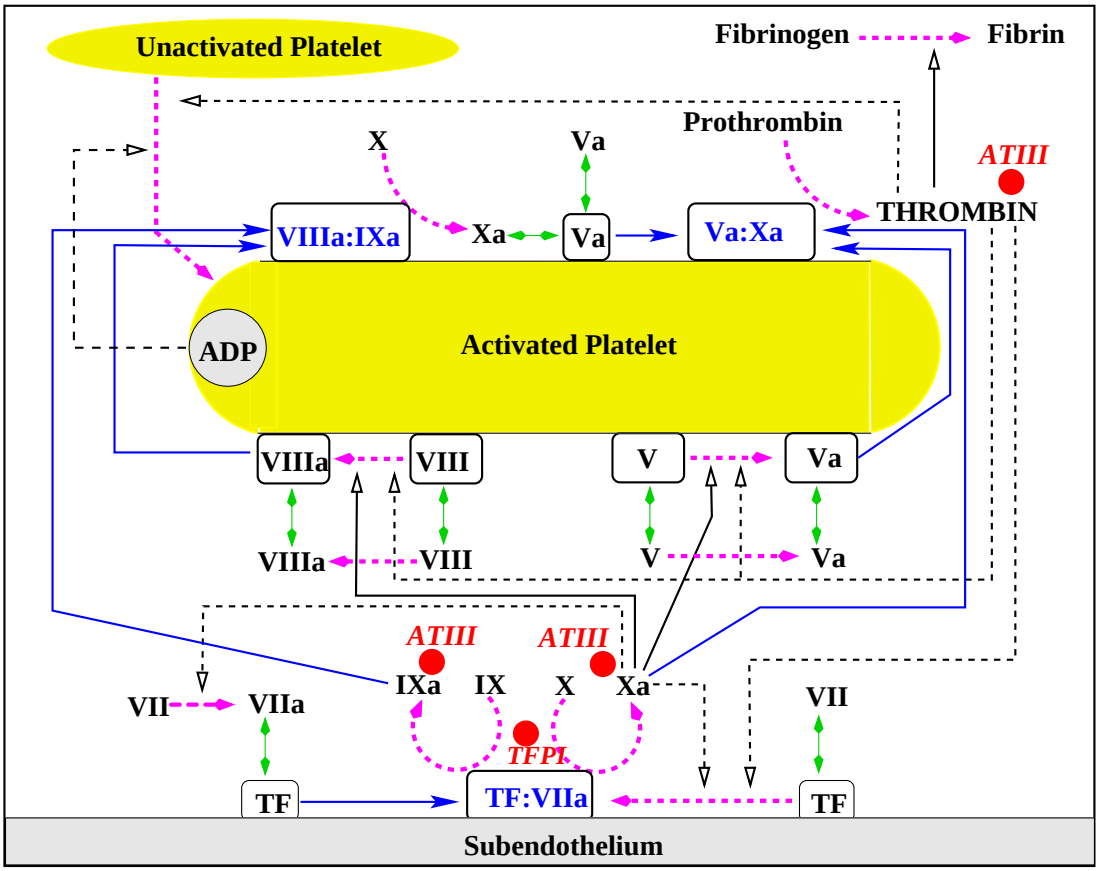


**Figure 1.1**. Schematic of coagulation reactions. Dashed magenta arrows show cellular or chemical activation processes. Blue arrows indicate chemical transport in the fluid or on a surface. Green segments with two arrowheads depict binding and unbinding from a surface. Rectangular boxes indicate surface-bound species. Solid black lines with open arrows show enzyme action in a forward direction, while dashed black lines with open arrows show feedback action of enzymes. Red disks indicate chemical inhibitors.

activated platelet's surface. Early in the process, platelet-bound Xa activates the cofactors VIIIa and Va on the platelet surface.

- When a tenase (VIIIa:IXa) complex is formed on the activated platelet surface, it can activate platelet bound X to Xa (this is a second mechanism for Xa activation in addition to its activation by TF:VIIa on the subendothelium). A Xa molecule can bind with a platelet-bound Va molecule to form a prothrombinase (Va:Xa) complex on the platelet surface. Prothrombinase can activate platelet-bound prothrombin to the enzyme thrombin.

- Thrombin released from the activated platelet's surface activates other platelets.

It also activates cofactor molecules Va and VIIIa both in the plasma and on the surface of activated surfaces. It converts fibrinogen into fibrin monomers which then polymerize into a fibrin gel. (We do not model the conversion of fibrinogen to fibrin monomer or fibrin polymerization.)

- Upon a platelet's activation, specific binding sites become expressed on its surface for each of the zymogen/enzyme pairs IX/IXa, X/Xa, prothrombin/thrombin, and for each of the inactive/active cofactor pairs V/Va and VIII/VIIIa. The number of these binding sites that are available controls the formation and/or activity of the platelet-bound enzyme complexes.

- Platelets can be activated by contact with the subendothelium (not shown), or by exposure to thrombin or ADP. A finite quantity of ADP is released by a platelet during a time interval following the platelet's activation.

- Several chemical inhibitors (AT, TFPI, and APC) act on various species in the reaction network. A platelet adhering to the subendothelium inhibits the activity of the molecules on the portion of subendothelium it covers (not shown).

- All fluid-phase chemical species and unactivated platelets move with the fluid and diffuse relative to it (not shown).

- Activated platelets can bind to other activated platelets. A cluster of bound platelets generates resistance to the local fluid motion (not shown).

## 1.2 Previous Models

Numerous models of *portions* of the above system have been presented, e.g., [6, 8, 9, 19, 77, 78, 40, 41, 81, 34, 29, 20, 21], but, to our knowledge, the only one that couples a comprehensive model of coagulation biochemistry to models of platelet deposition and flow is that introduced by Kuharsky and Fogelson [38]. The 'KF model' considers the physical and chemical platelet and coagulation events that occur in a thin layer, called the reaction zone, just above a small vascular injury. The KF model takes into account plasma-phase, subendothelial-bound, and platelet-bound enzymes and zymogens, as well as activated and unactivated platelets. All species in the reaction zone are assumed to be well mixed; each species is characterized by its concentration which is tracked in time using an ordinary differential equation. Advective and diffusive transport of fluid-phase species (chemicals

and platelets) into or out of the reaction zone is modeled by a mass-transfer term in which the mass-transfer coefficient depends on flow and diffusion parameters.

Studies of the KF model revealed a sharp threshold in thrombin production in response to different densities of TF exposure and showed that the threshold level of TF and the concentration of thrombin produced were modified only moderately by large changes in the flow shear rate. The model studies provided kinetic explanations of the reduced thrombin production with hemophilia and thrombocytopenia. This work also led to the hypothesis that as platelets adhere to the subendothelium, they cover and so physically inhibit subendothelial-bound enzymes. This hypothesis was later given experimental support by studies conducted at the Nemerson lab [26], and the predicted threshold and its dependence on shear rate were seen experimentally in the Diamond lab [57]. Studies of an extended version of the model [22] highlighted the role of physical factors (fluid flow and platelet deposition) in establishing the TF threshold, and indicated that, for small injuries ($\approx 10\mu$m in length), flow-mediated dilution is a much more potent inhibitor than the well-studied chemical inhibitors TFPI and APC.

There have been a few other recent models that incorporate the mechanics of the blood flow together with a growing blood clot. Anand et al. (2003) modeled both blood and blood clots as shear-thinning viscoelastic fluids [6]. Partial differential equations were used to track the advection and diffusion of concentrations of resting and activated platelets. The platelets were assumed activated after contact with other activated platelets or thrombin, or if under prolonged exposure to certain levels of shear stress. The model included reaction-convection-diffusion equations to reflect components *in plasma* that make up the enzymatic cascade of reactions leading to clot formation and fibrinolysis. However, the included reactions did not represent all of those that occur as part of the normal coagulation system. Prothrombinase and tenase were the only membrane-bound chemicals that were considered. The generation and depletion of these two membrane-bound species was dependent on reactions of certain plasma components assumed to have linear dependence on activated platelet concentrations. In no other equations was there any dependence on activated platelet concentration. Binding sites on the platelets were not accounted for, and therefore, competition for these binding sites was excluded. The TF:VIIa complex, known to be important in the initiation of the clotting response [53], was assumed constant and simply incorporated into flux boundary conditions for factors XIa and Xa.

In the studies by Anand et al. the physical domain was one-dimensional; an infinitely

long rigid-walled cylindrical pipe was considered. As fibrin concentration reached above 600nM, a clot was assumed to form, and similarly, if the fibrin concentration decreased below that same value at a later time, clot dissolution was assumed to begin. The boundary between the growing blood clot and the fluid was considered as the height of the clot. The authors were able to predict the size (height) and velocity of the clot, as well as the shear and normal stress on the clot.

Later in 2008, Bodnar and Sequeira used a simplified version of this model in order to simulate clotting in three dimensions [9]. The simplification was the removal of the viscoelastic nature of the fluid and clot. As in the previous model, the only difference between the fluid and clot was the viscosity. This study, although largely focused on the numerical aspects of the project, incorporated the same biochemical equations and was able to provide quantitative predictions of fibrin and clot build-up in a fluid environment.

The KF model shows the importance of both platelet interaction with subendothelium-bound chemicals and competition for cell-surface binding sites for the maintenance and tight regulation of the coagulation cascade. The work of Anand et al. (2003) and Bodnar and Sequeira (2008) included flow and transport, but failed to include these two crucial biological mechanisms. However, because it describes a well-mixed system, the KF model is limited to describing events near small injuries. Further, because of its simple treatment of flow, it cannot account for significant growth of a thrombus and the effect of this on local flow and transport. The model we describe in the following chapter overcomes both of these challenges.

# CHAPTER 2

# MODEL

We consider a rectangular domain $[0, x_{max}] \times [0, y_{max}]$, in which the top and bottom vessel walls are represented by $y = 0$ and $y = y_{max}$, respectively, and we assume that blood enters at $x = 0$ with a specified velocity profile, and leaves at $x = x_{max}$. A section of the bottom wall $x_1 < x < x_2$ is taken to represent subendothelial material exposed by vessel injury. Fluid and blood-borne species (chemicals and cells) may be present anywhere in the domain. Their concentrations at the upstream boundary $x = 0$ are set to their normal blood concentrations. We track four groups of platelets: mobile and unactivated, mobile and activated, bound and activated, and subendothelial-bound and activated. Mobile platelets are advected by the fluid and diffuse through it. They may bind to the subendothelium or, if activated, to already bound and activated platelets of either type. We distinguish between three types of chemical species: fluid-phase chemicals which advect with the fluid and diffuse through it, chemicals bound to the subendothelium, which are immobile as long as they remain bound, and chemicals bound to bound platelets, which also are immobile while they remain bound to the platelets.

Although platelets are described in the model in terms of number densities (number/volume), the size of a platelet enters into the model in several ways. One is in terms of a maximum number density for platelets, $P_{max}$, which we set to $6.67 \times 10^7$ platelets per mm$^3$ based on the assumption that 20 platelets fit tightly into 300 $\mu m^3$. The total platelet fraction $\phi^T(\mathbf{x}, t)$ is the ratio of the sum of the four platelet number densities at $\mathbf{x}$ to this maximum density. The bound platelet fraction $\phi^B(\mathbf{x}, t)$ is similarly the ratio of the sum of bound activated and subenthelium-bound activated platelet number densities to the maximum density. The bound platelet fraction $\phi^B$ determines the resistance to flow in the corresponding portion of a thrombus. The total platelet fraction $\phi^T$ in a piece of the thrombus determines how easily, if at all, platelets may move into that piece of thrombus. Platelets may be excluded from regions into which the fluid can move if $\phi^T$ is sufficiently high. Platelet size also enters through a variable $\eta$, which determines a region around

the thrombus in which mobile activated platelets are deemed sufficiently close to bound platelets to bind. Finally, through the parameter $k_{adh}(\mathbf{x})$, the size of a platelet determines the region in which a platelet is sufficiently close to the subendothelium to adhere to it. These manifestations of platelet size are discussed further below. For easy reference to these important variables and parameters, they are listed in Table 2.1.

## 2.1 Fluid

We assume that the fluid motion is described by a modified version of the Navier Stokes equations for incompressible viscous flow:

$$\rho\ (\ \mathbf{u}_t + \mathbf{u}\cdot\nabla\mathbf{u}\ ) \;=\; -\nabla p + \mu\Delta\mathbf{u} \;-\; \mu\ \alpha(\phi^B)\ \mathbf{u}, \tag{2.1}$$

$$\nabla\cdot\mathbf{u} \;=\; 0. \tag{2.2}$$

Here, $\mathbf{u}(\mathbf{x},t)$ and $p(\mathbf{x},t)$ are the fluid velocity and pressure, respectively, at location $\mathbf{x}$ at time $t$, $\rho$ is the fluid mass density, and $\mu$ the dynamic viscosity. The term $-\mu\ \alpha(\phi^B)$, called the Brinkman term, is the modification we make to the standard Navier Stokes equations. It represents frictional resistance to the fluid motion past point $\mathbf{x}$ due to bound platelets there and relates to the inverse permeability of the growing platelet mass. In this term, $\phi^B(\mathbf{x},t)$ is the bound platelet fraction defined earlier, and the frictional resistance is assumed to increase with $\phi^B(\mathbf{x},t)$ according to the function $\alpha(\phi^B) = \alpha_{max}\ (\phi^B)^2/\left((\phi_0^B)^2 + (\phi^B)^2\right)$.

**Table 2.1**. Descriptions of selected model variables and parameters.

| Name | Description |
|---|---|
| $\phi^T$ | Total platelet fraction including bound and mobile. |
| $\phi^B$ | Bound platelet fraction. |
| $P_{max}$ | Maximum number density for platelets. |
| $P^{m,u}$ | Number density of mobile unactivated platelets. |
| $P^{m,a}$ | Number density of mobile activated platelets. |
| $P^{b,a}$ | Number density of bound activated platelets. |
| $P^{se,a}$ | Number density of subendothelium-bound activated platelets. |
| $k_{adh}(\mathbf{x})$ | Binding region above subendothelium. |
| $\eta$ | Virtual substance which determines binding region around thrombus. |
| $k_{coh}$ | Rate that mobile activated platelets cohere to thrombus. |
| $u, v$ | Fluid velocities. |
| $\rho$ | Fluid mass density. |
| $\alpha(\phi^B)$ | Relates bound platelet fraction to amount of fluid resistance. |
| $\alpha_{max}$ | Maximum value assigned to function, $\alpha(\phi^B)$. |
| $W(\phi^T)$ | Relates total platelet fraction to amount of flux impairment. |

We set $\phi_0^B = 0.5$ to be the bound platelet fraction at which the frictional resistance reaches half of its maximum value. We set $\alpha_{max}$ sufficiently large that there is little flow through a thrombus with $\phi^B \approx 1$.

To supplement these equations, there are no-slip boundary conditions on the top and bottom (vessel walls), a prescribed Poiseuille inflow at the left boundary, and homogeneous Neumann outflow at the right boundary.

## 2.2 Platelets

We denote by $P^{m,u}, P^{m,a}, P^{b,a}$ and $P^{se,a}$ the number densities of four classes of platelets we track, mobile unactivated, mobile activated, platelet-bound activated and subendothelium-bound activated, respectively. Each of the these is a function of $\mathbf{x}$ and $t$, and their evolution equations are

$$\begin{aligned}
\frac{\partial P^{m,u}}{\partial t} &= \underbrace{-\nabla\cdot\left\{\, W(\phi^T)\,\left(\mathbf{u}\,P^{m,u} - D\,\nabla P^{m,u}\right)\,\right\}}_{\text{Transport by advection and 'diffusion'}} \qquad (2.3)\\
&- \underbrace{k_{adh}(\mathbf{x})\;\{P_{max} - P^{se,a}\}\;P^{m,u}}_{\text{Adhesion to subendothelium}} - \underbrace{\{A_1(e_2) + A_2([\text{ADP}])\}\,P^{m,u}}_{\text{Activation by thrombin or ADP}}\\
\frac{\partial P^{m,a}}{\partial t} &= -\nabla\cdot\left\{\, W(\phi^T)\big(\mathbf{u}\,P^{m,a} - D\,\nabla P^{m,a}\big)\,\right\} \qquad (2.4)\\
&- k_{adh}(\mathbf{x})\,\{P_{max} - P^{se,a}\}\,P^{m,a} + \{A_1(e_2) + A_2([\text{ADP}])\}\,P^{m,u}\\
&- \underbrace{k_{coh}\;g(\eta)\;P_{max}\;P^{m,a}}_{\text{Cohesion to bound platelets}}\\
\frac{\partial P^{b,a}}{\partial t} &= -k_{adh}(\mathbf{x})\;\left(P_{max} - P^{se,a}\right)\;P^{b,a} \;+ k_{coh}\;g(\eta)\;P_{max}\;P^{m,a} \qquad (2.5)\\
\frac{\partial P^{se,a}}{\partial t} &= k_{adh}(\mathbf{x})\;\left(P_{max} - P^{se,a}\right)\;\left(P^{m,a} + P^{m,u} + P^{b,a}\right). \qquad (2.6)
\end{aligned}$$

For the mobile unactivated platelets, the term $\mathbf{J}^{m,u} = \mathbf{u}P^{m,u} - D\nabla P^{m,u}$ is the flux of these platelets due to advection with the fluid and diffusion. Real platelets have size and may not move as readily as fluid through a region already occupied in part by thrombus-bound platelets. To account for this in our model which tracks only the number density of platelets, not individual platelets of finite size, we multiply the flux vector $\mathbf{J}^{m,u}$ by a function $W(\phi^T)$

which is a monotonically decreasing function of the total platelet fraction with $W(0) = 1$ and $W(1) = 0$. We used the specific function $W(\phi^T) = \tanh(\pi(1 - \phi^T))$ which is depicted in Fig. 2.1. In using this shape of function we have assumed that the ability of mobile platelets to move into a region is only gradually impaired until $\phi^T$ reaches approximately 0.5, and then drops quickly. We discuss other choices for this function later in Chapter 4. This limitation on advective and diffusive motion is imposed on both populations of mobile platelets. The second term in each of equations (2.3) and (2.4) describes platelet adhesion to the exposed subendothelial material. The parameter $k_{adh}(\mathbf{x})$ is assumed to be a positive constant for points $\mathbf{x}$ within one platelet diameter's distance of the subendothelium and zero elsewhere. Since $P_{max}$ is the maximum number density of platelets, $P_{max} - P^{se,a}$ indicates the portion of the space just over the injury available for platelets to bind to the subendothelium. The rate of binding is assumed to be proportional to this value and to the local density of platelets that are sufficiently close to the subendothelium to be able to bind to it.

The third group of terms on the right side of equations (2.3) and (2.4) account for the activation of platelets by the chemical agonists thrombin and ADP. The activation rate functions $A_1(e_2)$ and $A_2([\text{ADP}])$ are each assumed to have the form $k_c^{pla}\frac{c}{c^*+c}$ where $c$ is the agonist concentration and $k_c^{pla}$ and $c^*$ are positive constants.

Equation (2.4) has one additional term that models platelet-platelet cohesion. Mobile activated platelets are able to bind to bound activated platelets to which they are sufficiently close and should bind at a rate that depends on the number of nearby bound activated platelets. We use the function $\eta(\mathbf{x}, t)$ to indicate both proximity to bound platelets and

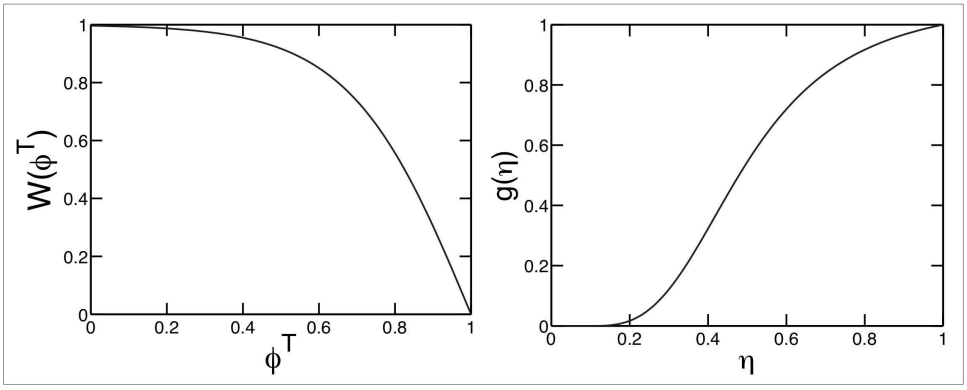


**Figure 2.1**. Left: Platelet density-dependent mobility limitation function. Right: Binding affinity function $g(\eta)$

the density of nearby bound platelets. The function $\eta$ is required to satisfy the partial differential equation:

$$\frac{\partial \eta}{\partial t} \;=\; D_\eta \,\Delta\, \eta \;-\; \gamma\, \eta \;+\; \gamma \,\left(\frac{P^{b,a} + P^{se,a}}{P_{max}}\right). \tag{2.7}$$

The virtual substance $\eta$ is produced by bound platelets at rate $\gamma$, decays at the same rate and diffuses with diffusion coefficient $D_\eta$. The value of $\eta$ drops substantially over a distance $(D_\eta/\gamma)^{1/2}$ from the thrombus-bound platelets. We choose $D_\eta$ and $\gamma$ so that this distance is comparable to a platelet diameter. By using the same rate constant $\gamma$ in both the production and decay terms in the equation for $\eta$, at steady state, the level of $\eta$ should be approximately the concentration of bound platelets in locations where there are bound platelets. The function $\eta$ is used in the model solely to indicate for any location $\mathbf{x}$ how many bound platelets are nearby. We assume that the rate at which activated platelets bind is proportional to both their own concentration and to the value of the 'binding affinity' function $g(\eta)$ shown in Fig. 2.1: $g(\eta) \;=\; g_0 \max\big(0,\; (\eta-\eta_t)^3/(\eta_*^3 + (\eta-\eta_t)^3)\big)$, where $\eta_t$ is a threshold level below which there is no binding, $\eta_* + \eta_t$ indicates the value of $\eta$ for which $g(\eta)$ changes rapidly, and $g_0$ is chosen so that $g(1) = 1$. We discuss how other choices for this function affect growth of the thrombus in Chapter 4. The terms in the equations for $P^{b,a}$ and $P^{se,a}$ are similar to those already described.

The full set of chemical equations that comprise the model are given in the Appendix, as are values of the rate constants and the sources of these values. In the next few sections we illustrate the types of chemical equations that appear in the full model. In this discussion, we use the following notation: for zymogen $i$ and enzyme $i$, $Z_i$ and $E_i$, $Z_i^{se}$ and $E_i^{se}$, and $Z_i^m$ and $E_i^m$ refer to these proteins in the fluid, bound to the subendothelium, or bound to the membrane of activated platelets, respectively. For example, $E_7^{se}$ refers to the TF:VIIa complex on the subendothelium and $E_5^m$ refers to Factor Va bound to the platelet surface. Concentrations are denoted in a similar way but with lower-case $z$ and $e$. A complex of $Z_i$ and $E_j$ is denoted by $Z_i : E_j$ and its concentration by $[Z_i : E_j]$. Special symbols are used for the platelet-bound 'tenase' VIIIa:IXa and 'prothrombinase' Va:Xa complexes, TEN = VIIIa:IXa and PRO = Va:Xa, and [TEN] and [PRO] denote their respective concentrations. The inhibitors are denoted APC and TFPI and their concentrations are denoted [APC] and [TFPI]. We denote the complex of TFPI and Xa by TFPIa, because this is the 'active' form of the inhibitor, and its concentration by [TFPIa].

## 2.3 Platelet-bound Chemical Species

We now illustrate the different types of terms that appear in the model's equations for chemical species bound to activated platelets. To do this, we consider the equation for the platelet bound enzyme $E_2^m$ (thrombin).

$$\begin{aligned}\frac{\partial e_2^m}{\partial t} &= \underbrace{k_{e_2}^{on}\ e_2\ \left(N_2^b\ P^{b,a} + N_2^{se}\ P^{se,a} - z_2^{mtot} - e_2^{mtot}\right) - k_{e_2}^{off}\ e_2^m}_{\text{Binding with receptors on platelet surface}} \\ &+ \underbrace{(k^-_{z_5^m:e_2^m} + k^{cat}_{z_5^m:e_2^m})\ [Z_5^m : E_2^m] - k^+_{z_5^m:e_2^m}\ z_5^m\ e_2^m}_{\text{Activation of Va by thrombin}} \\ &+ \underbrace{(k^-_{z_8^m:e_2^m} + k^{cat}_{z_8^m:e_2^m})\ [Z_8^m : E_2^m] - k^+_{z_8^m:e_2^m}\ z_8^m\ e_2^m}_{\text{Activation of VIIIa by thrombin}} \\ &+ \underbrace{k^{cat}_{z_2^m:PRO}\ [Z_2^m : \text{PRO}]}_{\text{Activation by prothrombinase}}.\end{aligned} \tag{2.8}$$

The term $k_{e_2}^{on}\ e_2\ (N_2^b P^{b,a} + N_2^{se} P^{se,a} - z_2^{mtot} - e_2^{mtot})$ gives the rate at which the fluid-phase enzyme thrombin binds to the specific binding sites for prothrombin and thrombin on the surfaces of activated platelets while $k_{e_2}^{off}\ e_2^m$ is the rate at which thrombin dissociates from the binding sites. The quantities $N_2^b$ and $N_2^{se}$ denote the total number of binding sites per platelet specific for thrombin and prothrombin for each type of bound platelet, so that $N_2^b\ P^{b,a}$ and $N_2^{se}\ P^{se,a}$ are the volume concentrations of binding sites for those chemicals on the platelet-bound and subendothelium-bound platelets, respectively. The concentration of occupied binding sites $z_2^{mtot} + e_2^{mtot}$ is subtracted from this quantity to give the concentration of available binding sites. The concentrations of occupied binding sites account for platelet bound prothrombin and thrombin as well as with their platelet-bound complexes: $z_2^{mtot} = z_2^m + [Z_2^m : \text{PRO}]$ and $e_2^{mtot} = e_2^m + [Z_5^m : E_2^m] + [Z_8^m : E_2^m]$. The terms $(k^-_{z_5^m:e_2^m} + k^{cat}_{z_5^m:e_2^m})\ [Z_5^m : E_2^m]$ and $k^+_{z_5^m:e_2^m}\ z_5^m\ e_2^m$ pertain to the association and dissociation of $Z_5^m$ with $E_2^m$ on the platelet surface and the enzymatic activation of $Z_5^m$ to $E_5^m$. The terms $(k^-_{z_8^m:e_2^m} + k^{cat}_{z_8^m:e_2^m})\ [Z_8^m : E_2^m] - k^+_{z_8^m:e_2^m}\ z_8^m\ e_2^m$ play a similar role, but for $Z_8^m$. Platelet-bound chemicals are considered only in locations where $P^{b,a}$ or $P^{se,a}$ is non-zero.

## 2.4 Subendothelium-bound Chemical Species

We use the following equation for the concentration, $e_7^{se}$, of the enzyme complex TF:VIIa to illustrate the terms that appear in equations for chemical species bound to the subendothlium:

$$\begin{aligned}
\frac{\partial e_7^{se}}{\partial t} &= \underbrace{k_{e_7}^{on}\ e_7\ (TF - e_7^{se,tot} - z_7^{se,tot}) - k_{e_7}^{off}\ e_7^{se}}_{\text{Binding with TF}} \\
&+ \underbrace{k_{z_7^{se}:e_{10}}^{cat}\ [Z_7^{se} : E_{10}] + k_{z_7^{se}:e_2}^{cat}\ [Z_7^{se} : E_2]}_{\text{Activation by Xa or thrombin}} \\
&+ \underbrace{(k_{z_{10}:e_7^{se}}^{-} + k_{z_{10}:e_7^{se}}^{cat})\ [Z_{10} : E_7^{se}] - k_{z_{10}:e_7^{se}}^{+}\ z_{10}\ e_7^{se}}_{\text{Activation of X to Xa}} \\
&+ \underbrace{(k_{z_9:e_7^{se}}^{-} + k_{z_9:e_7^{se}}^{cat})\ [Z_9 : E_7^{se}] - k_{z_9:e_7^{se}}^{+}\ z_9\ e_7^{se}}_{\text{Activation of IX to IXa}} \\
&+ \underbrace{k_{tfpia:e_7^{se}}^{-}\ [\text{TFPIa} : E_7^{se}] - k_{tfpia:e_7^{se}}^{+}\ [\text{TFPIa}]\ e_7^{se}}_{\text{Binding with TFPI:Xa}} \\
&- \underbrace{k_{adh}(\mathbf{x})\ (P^{se,a} + P^{se,u} + P^{b,a})\ e_7^{se}}_{\text{Coverage by Platelet Deposition}}.
\end{aligned} \tag{2.9}$$

As indicated by the labels under the terms, the first five groups of terms describe the binding of fluid-phase factor VIIa molecules to available TF molecules or the unbinding of VIIa from TF; the activation of TF:VII to TF:VIIa by factor Xa or thrombin; the binding of factor X to TF:VIIa and its unbinding from or activation by this complex; the binding of factor IX to TF:VIIa an its unbinding from or activation by the complex; and the interaction of the inhibitor complex TFPIa (i.e, TFPI:Xa) with TF:VIIa. The only new type of term is the last one which describes the decrease of accessible TF:VIIa molecules at a rate proportional to the rate at which platelets become subendothelium-bound and thus cover a portion of the subendothelium. A similar platelet deposition term appears in each of the subendothelium-bound chemical equations.

## 2.5 Fluid-phase Chemical Species

Each of the fluid-phase chemicals advects with the fluid and diffuses through it. Some fluid-phase chemicals bind to bound platelets and some bind to the subendothelium, but there are no species that do both. We use fluid-phase factor Xa to illustrate the types

of terms that appear in the differential equations and boundary conditions for fluid-phase chemicals:

$$\begin{aligned}\frac{\partial e_{10}}{\partial t} \quad = \quad & \underbrace{-\mathbf{u}\cdot\nabla e_{10} + \nabla\cdot(D\nabla e_{10})}_{\text{Transport by advection and diffusion}} \\ + \quad & \underbrace{(k^{-}_{z_7:e_{10}} + k^{cat}_{z_7:e_{10}})[Z_7 : E_{10}] \;-\; k^{+}_{z_7:e_{10}}\; z_7\; e_{10}}_{\text{Activation of VII}} \\ & \underbrace{-\; k^{in}_{e_{10}}\; e_{10} \;+\; k^{-}_{tfpi:e_{10}}\;[\text{TFPIa}] \;-\; k^{+}_{tfpi:e_{10}}\;[\text{TFPI}]\; e_{10}}_{\text{Inhibition by ATIII or by binding to TFPI}} \\ & \underbrace{-\; k^{on}_{e_{10}}\; e_{10}\; \left(N^{b}_{10}P^{b,a} + N^{se}_{10}P^{se,a} - z^{ptot}_{10} - e^{ptot}_{10}\right) + k^{off}_{e_{10}}\; e^{m}_{10}.}_{\text{Binding to platelet receptor for X and Xa}}\end{aligned} \tag{2.10}$$

The first group of terms on the right hand side of this equation represent advection and diffusion. The next group of terms concerns activation of fluid-phase factor VII by fluid-phase factor Xa. The third group has a term $-\; k^{in}_{e10}\; e_{10}$ representing inhibition of factor Xa by the fluid-phase inhibitor ATIII, and a set of terms describing the interaction of factor Xa with the fluid-phase inhibitor TFPI. The last group of terms represents binding and unbinding of Xa with the platelet surface receptors shared by factors X and Xa. Similarly to the discussion of platelet-bound thrombin above, $N^{b}_{10}P^{b,a}+N^{se}_{10}P^{se,a}-z^{ptot}_{10}-e^{ptot}_{10}\big)+k^{off}_{e_{10}}\; e^{m}_{10}$ is the total concentration of platelet binding sites for X/Xa $N^{b}_{10}P^{b,a} + N^{se}_{10}P^{se,a}$ less the concentration of those already occupied by either X or Xa, $z^{ptot}_{10} + e^{ptot}_{10}$.

For a fluid-phase chemical which can be produced on the subendothelium and which can bind to molecules on the subendothelium, these interactions are incorporated in the boundary condition for that chemical's concentration. For $e_{10}$, the boundary condition at each point of the injured portion of the vessel wall is

$$-D\frac{\partial e_{10}}{\partial y} = \underbrace{k^{cat}_{z_{10}:e^{se}_7}\;[Z_{10} : E^{se}_7]}_{\text{Activation by TF:VIIa}} + \underbrace{\left(k^{-}_{z^{se}_7:e_{10}} + k^{cat}_{z^{se}_7:e_{10}}\right)\;[Z^{se}_7 : E_{10}] - k^{+}_{z^{se}_7:e_{10}}\; z^{se}_7\; e_{10}}_{\text{Binding to and activation of TF:VII}} \tag{2.11}$$

while on the remaining portions of the vessel walls, the boundary condition is

$$-D\frac{\partial e_{10}}{\partial y} = 0. \tag{2.12}$$

As indicated earlier, the concentration of a fluid-phase chemical such as factor Xa is set to its normal plasma concentration at the upstream end of the domain and is assumed to satisfy the condition $\partial e_{10}/\partial x = 0$ at the downstream boundary.

### 2.5.1 ADP

An unactivated platelet contains quantities of the activating chemical ADP stored within its dense granules. Upon activation, the dense granules fuse with the platelet's membrane and release their contents into the surrounding fluid. To represent this, we assume that ADP is released over a period of one to five seconds after platelet activation. Once released, ADP molecules move through the fluid and can activate nearby platelets. Embodying these assumptions, the ADP concentration, [ADP], satisfies the equation

$$\frac{\partial[\text{ADP}]}{\partial t} \;=\; -\,\mathbf{u}\cdot\nabla[\text{ADP}] \;+\; \nabla\cdot(D\nabla[\text{ADP}]) \;+\; \sigma_{release}. \tag{2.13}$$

which says that ADP moves by advection and diffusion. The source term $\sigma_{release}$ describes the release of ADP from bound activated platelets.

We define the source term from ADP release as

$$\sigma_{release}(\mathbf{x},t) = \int_0^\infty \hat{A}R(\tau)\frac{\partial}{\partial t}(P^{b,a}+P^{se,a})(\mathbf{x},t-\tau)d\tau, \tag{2.14}$$

where $\hat{A}$ is the total quantity of ADP released by an activated platelet, and $R(\tau)$ is the rate of release at an *elapsed time* $\tau$ since the platelet was activated, normalized so that $\int_0^\infty R(\tau)d\tau = 1$. To understand Equation (2.14), note that $\frac{\partial}{\partial t}(P^{b,a}+P^{se,a})(\mathbf{x},t-\tau)d\tau$ is the number of platelets newly activated and bound at location $\mathbf{x}$ in the time interval $[t-\tau, t-\tau+d\tau]$ and that $\hat{A}R(\tau)$ is the rate of release of ADP by these platelets $\tau$ time units later, *i.e.* at time $t$. We choose $R(\tau)$ to have value zero up to one second after activation, to be a positive bell-shaped function for the time interval $1 < \tau < 5$ seconds, and to have a peak at three seconds, consistent with observations reported in the literature [61]. Since $R(\tau)$ is nonzero only in the time interval $0 < \tau < 5$ sec, formula Eqation (2.14) actually involves an integral over that finite time interval.

## 2.6 Near-Wall Excess of Platelets

Observations *in vivo* [67] revealed that the near-wall platelet concentration in arterioles can be two to three times higher than that in the center of the vessel, and *in vitro* experiments demonstrated with platelet-sized beads that the near-wall concentration can be three to eight times that in the central region, depending on wall shear rate and hematocrit [18]. Based on his observations, Eckstein [17] presented a concentration profile function that is the basis for the inlet profile we prescribe for mobile unactivated platelets. Figure 2.2 shows the four inlet platelet concentration profiles that result from our synthesis of data in [18, 68, 79] and which we used in our simulations.

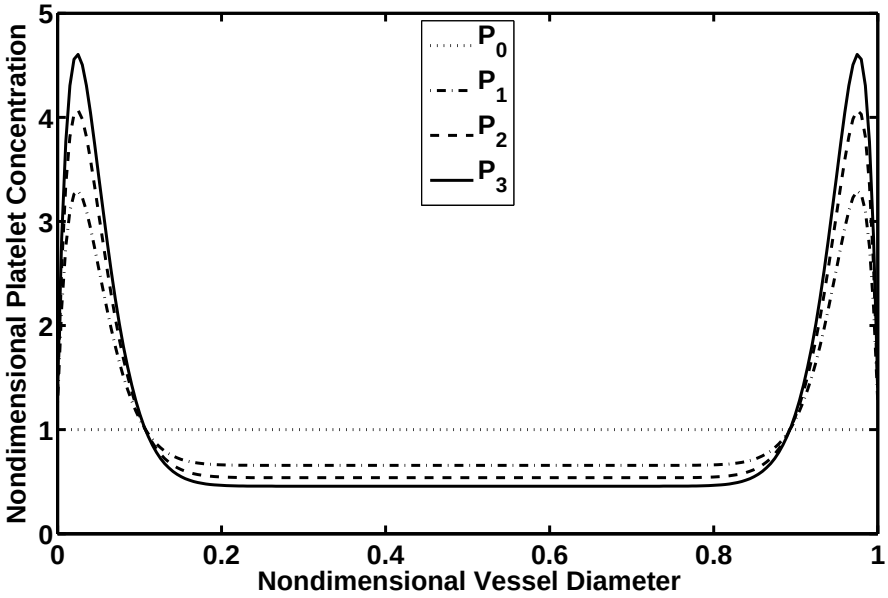


**Figure 2.2**. Platelet inlet concentration profiles. Peak-to-center ratios are set to approximately 1, 5, 7.5, and 10 for platelet profiles $P_0, P_1, P_2$ and $P_3$ respectively.

The simulations described below were carried out on a $32 \times 128$ grid and with a variable timestep set to 3/4 of the Courant number. For simulations carried out on a $64 \times 256$ grid, the bound platelet and thrombin concentrations after 600 seconds were very similar to those shown.

# CHAPTER 3

# MODEL RESULTS

The following results are reproduced with kind permission from Oxford University Press: *Mathematical Medicine and Biology*, Grow with the flow: a spatialtemporal model of platelet deposition and blood coagulation under flow, 2010, DOI: 10.1093/imammb/dqq005, K. Leiderman and A.L. Fogelson.

To familiarize the reader with the basic model results, Figure 3.1 shows 12 snapshots from a simulation of 10 min of clotting activity. Blood flows from left to right with a prescribed parabolic inflow velocity profile. Platelets and fluid-phase clotting chemicals have prescribed concentrations at the inlet and move downstream with the flow. The channel has height 60 $\mu$m, length 240 $\mu$m and there is an injury of length 90 $\mu$m centered at the midpoint of the bottom wall. The Brinkman coefficient, $\alpha_{max}$, is set to 400 and the initial TF density in the injury is set to 15 fmol/cm$^2$. (For the next three sections, this will be the setup for each simulation described.) After 50 seconds, platelets partially cover the injury site, but there is little effect as yet on the overall flow. As the thrombus grows

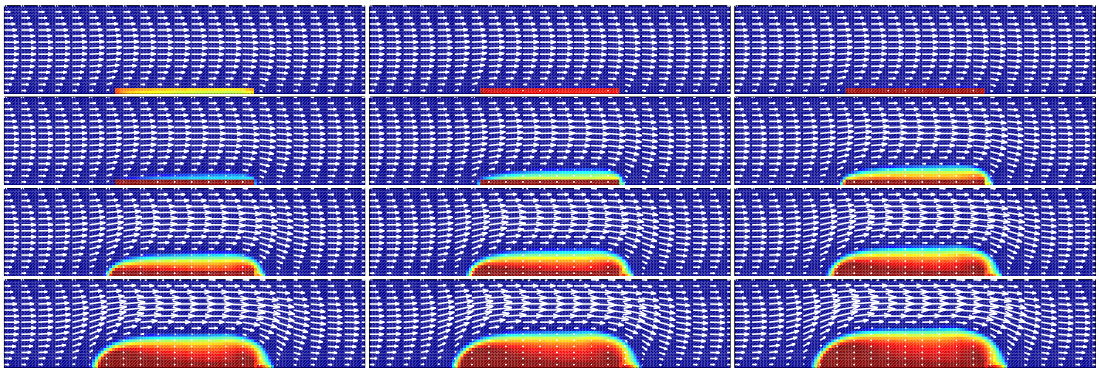

**Figure 3.1**. Time sequence of growing thrombus, at times 50, 100, 150, ..., 600 seconds (from left to right, top to bottom) for initial TF density 15 fmol/cm$^2$, shear rate 1500 s$^{-1}$, and platelet profile $P_3$. The arrows show the fluid velocity and have a uniform scaling throughout the sequence. Bound platelet concentrations vary from 0 (dark blue) to $P_{max}$ (dark red).

beyond the initial subendothelial-bound platelets, it begins to noticably perturb the flow. By 600 seconds, the thrombus has grown substantially and, as indicated by the uneven distribution of dark-red patches, the platelet distribution in the thrombus has significant spatial heterogeneity. The flow has been largely diverted around the thrombus accelerating as it passes over the thrombus and then slowing when the vessel lumen widens downstream of the thrombus. The velocity within the thrombus is much less than that in the bulk flow, but has a significant impact on thrombus growth as discussed below.

## 3.1 Thrombin Production Dependence on Tissue Factor Density

Figure 3.2 shows that the concentration of thrombin that is obtained after 10 minutes of clotting activity has a sharp threshold dependence on the density of TF initially exposed to the blood. This prediction is in agreement with results from the well-mixed KF model [38, 22]. The threshold behavior can also be seen in the thrombin concentration distribution and in the accumulation of bound platelets for different initial TF exposures as also shown in Figure 3.3. For a TF density of 1 fmol/cm$^2$, thrombin production is insignificant, while for a slightly larger TF density of 3 fmol/cm$^2$, the thrombin concentration reaches levels of 10-50 nM. Once the TF exposure is sufficiently high, there is little change in the amount of thrombin produced or in the size of the thrombus that develops. This can be seen in the results for TF densities of 15 and 30 fmol/cm$^2$ shown in the bottom two panels in the left

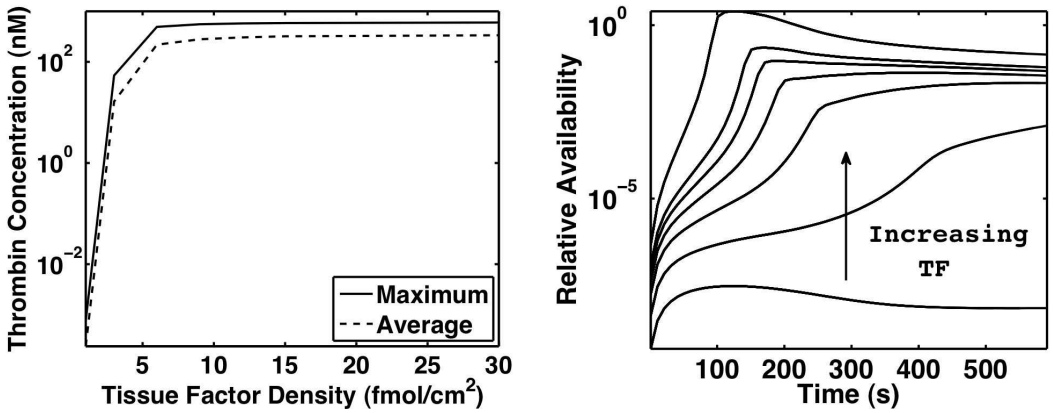


**Figure 3.2**. The left plot shows the spatial maximum and mean thrombin concentrations within the thrombus 10 min after TF exposure as a function of the density of exposed TF. The right plot shows the relative simultaneous availability of $e_9$ and $e_8^m$ as a function of time for TF densities (bottom to top) 1,3,6,9,12,15, and 30 fmol/cm$^2$.

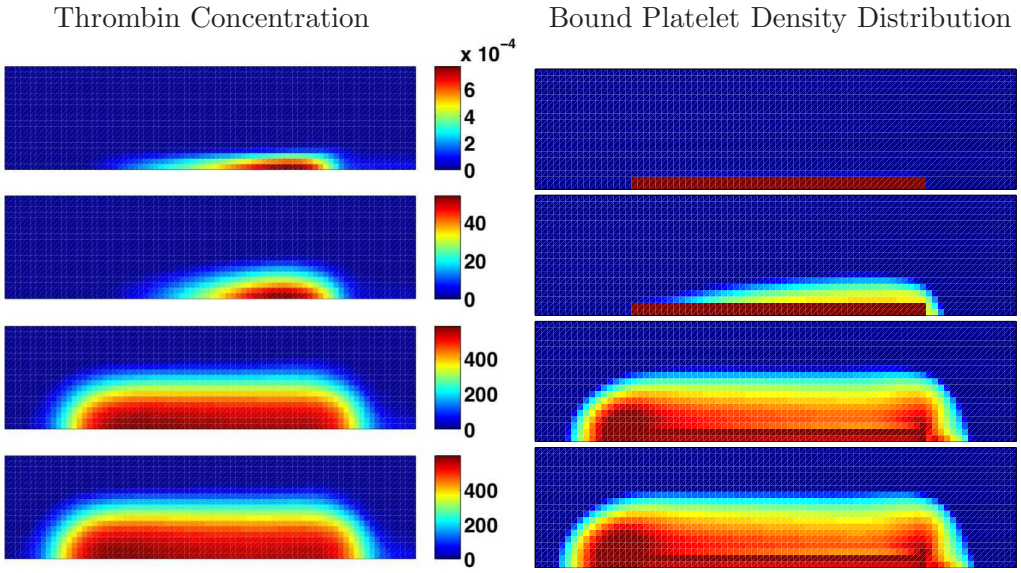


**Figure 3.3**. The plots in columns 1 and 2 are the spatial concentrations of fluid-phase thrombin ($e_2$) in nM and bound platelets ($P^{b,a}+P^{se,a}$) that vary from 0 (dark blue) to $P_{max}$ (dark red). From top to bottom, the density of TF exposed is 1, 3, 15, and 30 fmol/cm$^2$. For all cases, the wall shear rate is 500 s$^{-1}$ and the platelet profile is $P_1$.

and right of Figure 3.3.

Using an extension of the KF model, Fogelson and Tania [22] showed that an insignificant amount of thrombin was produced if there was only a short 'overlap time' during which substantial amounts of fluid-phase IXa and platelet-bound VIIIa both existed. Both of these concentrations depend on the level of TF exposure, factor IXa because it is produced by the TF:VIIa complex, and platelet-bound VIIIa because the dominant activator of this cofactor during the first 60 seconds of clotting activity is factor Xa also produced by the TF:VIIa complex. Since the current model gives spatial information, we quantified the overlap time by summing, over all spatial points, the product of the fluid-phase IXa and the platelet-bound VIIIa concentrations. (We normalized this quantity by its maximum over all times and TF densities considered.) The curves in the right panel of Figure 3.2 show this measure of overlap as a function of time for different TF densities (increasing from bottom to top) and we see that for all above-threshold cases (curves 3 and higher) there is a period in which the overlap measure increases sharply. This sharp increase is followed quickly by successive sharp increases in tenase, prothrombinase and thrombin (not shown).

As the TF density increases from 15 to 30 fmol/cm$^2$, there is little change ($\approx 2.5\%$) in

the maximum concentration of thrombin achieved. Since this level is substantially below the plasma concentration (1.4 $\mu$M) of the thrombin precursor, prothrombin, substrate availability is not the limiting factor that prevents greater thrombin production. Figure 3.4 shows how the maximum tenase and prothrombinase concentrations change with TF density. We see that the tenase concentration continues to increase significantly even at high TF densities, but the prothrombinase concentration plateaus. The increase in tenase implies an increased *potential* to generate platelet-bound factor Xa, the enzyme part of prothrombinase and yet there is little change in prothrombinase levels. The explanation for this is that tenase is unable to produce platelet-bound factor Xa at its potential.

Figure 3.5 shows, for a TF density of 15 fmol/cm$^2$, the spatial distribution (at 10 min) of the tenase and prothrombinase complexes and the unoccupied platelet binding sites for X and Xa. Where the tenase concentration is high, there are few unoccupied binding sites to which X can bind. Since tenase activates only platelet-bound X to Xa, tenase activity is therefore severely limited. The bulk of the occupied X/Xa binding sites are bound to Xa molecules that have been incorporated in prothrombinase complexes. Many X/Xa binding sites are available on newly-activated platelets at the upstream end of the thrombus, but there is essentially no tenase in that region. The spatial distribution of tenase, empty X/Xa binding sites, and prothrombinase for a TF density of 30 fmol/cm$^2$ (not shown) are similar but the tenase levels are about six-fold higher.

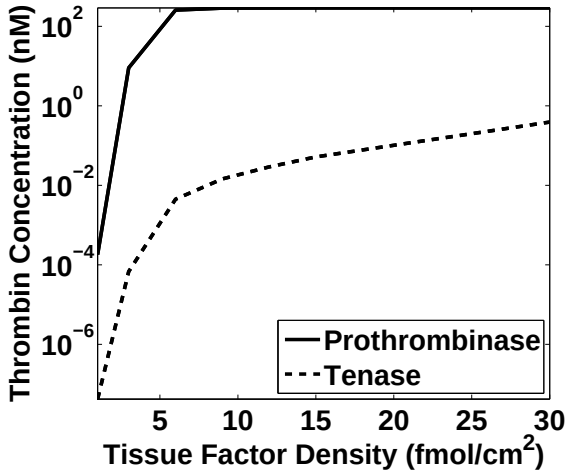


**Figure 3.4**. Maximum prothrombinase and tenase concentrations at any point within the entire domain 10 minutes after TF exposure to plasma as a function of the density of TF exposed. Wall shear rate of the flow is 500 $s^{-1}$ and the platelet profile is $P_1$.

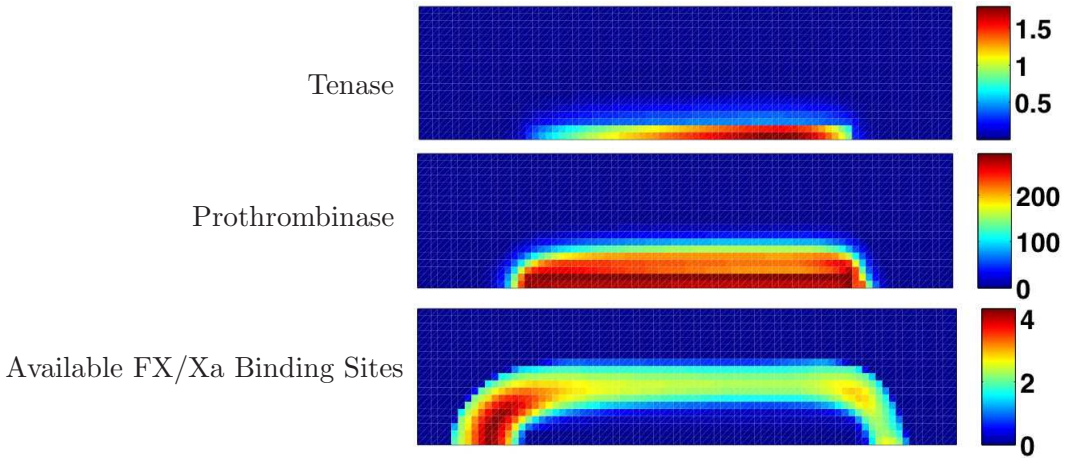


**Figure 3.5**. Spatial concentration (nM) of tenase (top panel), prothrombinase (middle panel) and available binding sites for factor X/Xa (bottom panel). In this simulation, the initial TF density is set to 15 fmol/cm$^2$, the wall shear rate is 500 $s^{-1}$, and the platelet profile is $P_1$.

The level of exposure of tissue factor (TF) is a critical determinant of the response of the coagulation system. About 1% of circulating factor VII is the active form factor VIIa. On its own, factor VIIa is a weak enzyme, but when bound to a subendothelial TF molecule, it becomes a powerful activator of factors IX and X. Presumably small amounts of TF are routinely exposed to the blood by small injury or other means. Because of the threshold nature of the system's response to the level of TF exposure, these small amounts of TF do not trigger a substantial production of thrombin. Yet if a more sizeable trauma causes a sufficiently high exposure of TF, the response of the system is rapid and strong.

Based on our simulations, we believe that the essential condition that has to achieved in order to trigger a substantial response is the *simultaneous* availability of platelet-bound factor VIIIa and fluid-phase or platelet-bound factor IXa. These are the cofactor and enzyme components of the tenase complex that can form on the surface of activated platelets. Factor IXa is produced only by subendothelial TF:VIIa (in the model) and thus its production depends on the density of TF:VIIa on the subenothelium, and thus on the density of TF exposed. Because the progressing deposition of platelets on the subendothelium reduces and eventually eliminates the accessibility of TF:VIIa to its substrates, production of factor IXa is limited largely to the first two minutes following injury, and much of the IXa produced is carried away by flow or inhibited by the fluid-phase inhibitor ATIII. Removal by flow or inhibition by ATIII are also the fate of most of the factor Xa activated

by TF:VIIa. Since this is the dominant activator of platelet-bound VIIIa during the first 60 s following injury, the density of TF:VIIa exposed also, indirectly, strongly influences the availability of factor VIIIa during the early stages of coagulation. Although we have yet to study hemophilia with our new model, we note that hemophilias A and B are deficiencies in the plasma levels of factors VIII and IX, respectively. Without the activated forms of these factors (activated directly or indirectly by TF:VIIa as just described), the initial stimulus for coagulation is not successfully transferred to the surfaces of the depositing platelets.

Our model currently does not include factor XI and its activated form factor XIa. There is increasing experimental support for a possible role of XI in the coagulation process; it has been shown that thrombin can activate XI to XIa and that XIa can activate factor IX to IXa. This second pathway to factor IXa production is believed by some to be important in determining the ultimate levels of thrombin produced late in the coagulation process. Recent simulations based on an extension of the KF model (unpublished data) suggest that for each shear rate considered (10, 50, 100, 500 $\text{sec}^{-1}$), there is a narrow range of TF densities for which the inclusion of factor XI increases the thrombin concentration significantly. Yet it will be interesting to extend the spatial-temporal model we present here to look at this as well.

The availability of surface-bound cofactor molecules (such as TF) and binding sites for cofactors, enzymes, and substrates on the surfaces of activated platelets strongly influences coagulation events. Without these sites the powerful enzyme complexes critical in coagulation would not form. The enzyme molecules generally compete for these sites with their zymogen precursors, and because the zymogen concentrations are typically larger than the corresponding enzyme concentrations, most binding sites are occupied by zymogen. For example, over 90% of the platelet binding sites shared by factors IX and IXa is occupied by the zymogen. This is not the case however for the shared binding sites for factors X and Xa under conditions of high TF exposure. For a TF exposure of 15 $\text{fmol/cm}^2$ or higher, formation of prothrombinase is limited because the great majority of these sites become occupied by Xa molecules that are part of the existing prothrombinase complexes. This implies that there are few or no empty binding sites for the precursor zymogen factor X, the substrate for tenase, and consequently the six-fold higher tenase concentration that forms for [TF]=30 $\text{fmol/cm}^2$ than at 15 $\text{fmol/cm}^2$ does not lead to increased prothrombinase formation or thrombin production.

## 3.2 Thrombus Growth Dependence on Wall Shear Rate and Near-Wall Excess of Platelets

Turitto *et al.* [74] report an increase in thrombus growth with wall shear rate. They attributed this increase to an enhancement of the local arrival rate of platelets and hypothesized that a possible mechanism for such an enhancement would be a near-wall excess of platelets of the type illustrated in Figure 2.2. Motivated by these experiments, we carried out simulations at three shear rates 500, 1000, and 1500 $s^{-1}$ and with the four platelet concentration profiles $P_0$, $P_1$, $P_2$, and $P_3$ illustrated in Figure 2.2. Results of these simulations are shown in Figs. 3.6-3.7. One set of experiments, the 'uniform profile' set, looked at the effect of varying shear rate with the fixed and uniform inflow platelet concentration profile $P_0$. For the 'fixed nonuniform profile' set, the inflow platelet profile was kept fixed at the nonuniform profile $P_1$ with a peak-to-center ratio of 5 as the shear rate was varied. In the 'varying nonuniform profile' experiments, the different spatially nonuniform inflow profiles $P_1$, $P_2$, and $P_3$, with peak-to-center ratios of 5, 7.5, and 10, were used for shear rates 500, 1000, and 1500 $s^{-1}$, respectively.

From the spatial plots (at 600 seconds) in Figure 3.6, we see i) no apparent difference in the bound platelet concentration as shear rate is varied with the spatially-uniform platelet profile, ii) an increased extent of high density regions (dark red) but no apparent difference in overall thrombus size as shear rate is increased in the fixed nonuniform simulations, and iii) an increase in both overall thrombus size and in high density regions as shear rate

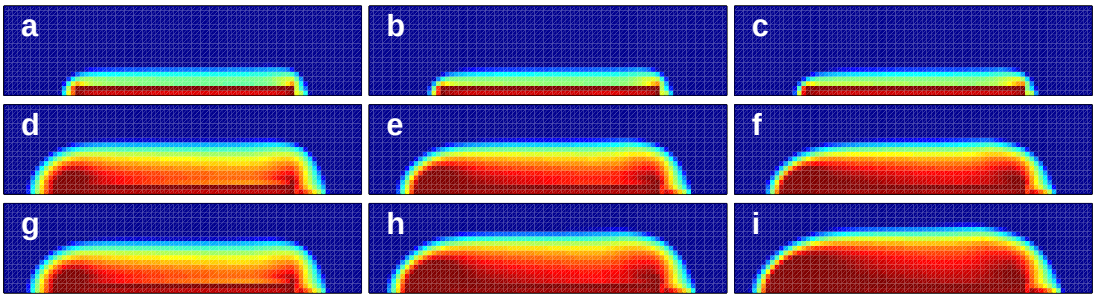


**Figure 3.6**. Bound platelet concentrations after 10 minutes for three different wall shear rates and four different platelet profiles. Close-up of approximately 188 $\mu$m long by 38 $\mu$m high region around thrombus. Bound platelet concentrations vary from 0 (dark blue) to $P_{max}$ (dark red). Columns 1, 2 and 3 represent wall shear rates of 500, 1000, 1500 $s^{-1}$ respectively. The experiments in rows 1 (a-c) and 2 (d-f) use platelet profiles $P_0$ and $P_1$ respectively. The experiments across the bottom row (g-i) use the platelet profiles $P_1, P_2$ and $P_3$, respectively.

increased in the varying nonuniform simulations. Comparing plots within each column, we see that for a fixed shear rate, thrombus size increased with increasing peak-to-center ratios in platelet concentration.

To quantify these observations further, we computed for each clot, the 'area' in which the bound platelet concentration exceeded 10 and 90% of $P_{max}$, respectively. We regard the first as giving a measure of overall thrombus size, and the latter as providing information about the bound platelet density distribution with the thrombus. (These areas were computed by counting the computational grid cells in which the various platelet density levels were exceeded.) The results are shown in Figure 3.7.

A noteworthy feature of all of the plots is the appearance of a temporary plateau at an area of 100 grid cells. This is the area of the region in which the adhesion rate function $k_{adh}(\mathbf{x})$ is nonzero. Recall that to adhere directly to the subendothelium does not require prior activation, so the time to reach this plateau is affected little by chemistry but can be affected by the rate of delivery of platelets to this region. This is clearly seen in Figure 3.7b and 3.7d, which shows how the time it takes for subendothelial platelets to reach 90% of their maximum concentration is affected by shear rate (Figure 3.7d) or shear rate and platelet concentration profile together (Figure 3.7f). The end of the plateaus in the left panels indicates the beginning of thrombus growth beyond direct subendothelial adhesion.

Each panel in the top two rows of Figure 3.7 shows the effect of varying shear rate for a fixed inflow platelet concentration profile. The plots for 10% density show that the effect of shear rate alone on thrombus area is minimal. The 90% density plots demonstrate that shear rate affects thrombus density; platelet density in the thrombus increases with shear rate. Referring to Figure 3.6, we see that the density increase occurs in a spatially heterogeneous manner. When the platelet peak-to-center ratio and the shear rate are both increased (Figure 3.7e-3.7f), there is a moderate increase in thrombus area and a large increase in thrombus density compared both to the change in area in this set of experiments and to the density changes when shear rate only is varied (Figure 3.7d). At the highest shear rate, large density regions developed in the upstream third and near the downstream end of the thrombus.

In our simulations, if the platelet concentration is uniformly 250,000 platelets/$\mu$L, a typical plasma value, we see little thrombus growth beyond direct adhesion to the subendothelium. A three-fold increase in shear rate (from 500 to 1500 $s^{-1}$) and therefore in the rate at which platelets are brought to the vicinity of the injury does not lead to appreciable

increases in platelet deposition at least for the value of the cohesion parameter $k_{coh}$ used in these simulations (see below). By contrast, for nonuniform platelet concentration profiles similar to those measured experimentally, substantial thrombus growth occurs under the same conditions, which lead to little thrombus growth for the uniform profile.

Experimental data about the near-wall platelet excess is not clear about whether or to what extent the peak-to-center concentration ratio increases with shear rate in the range

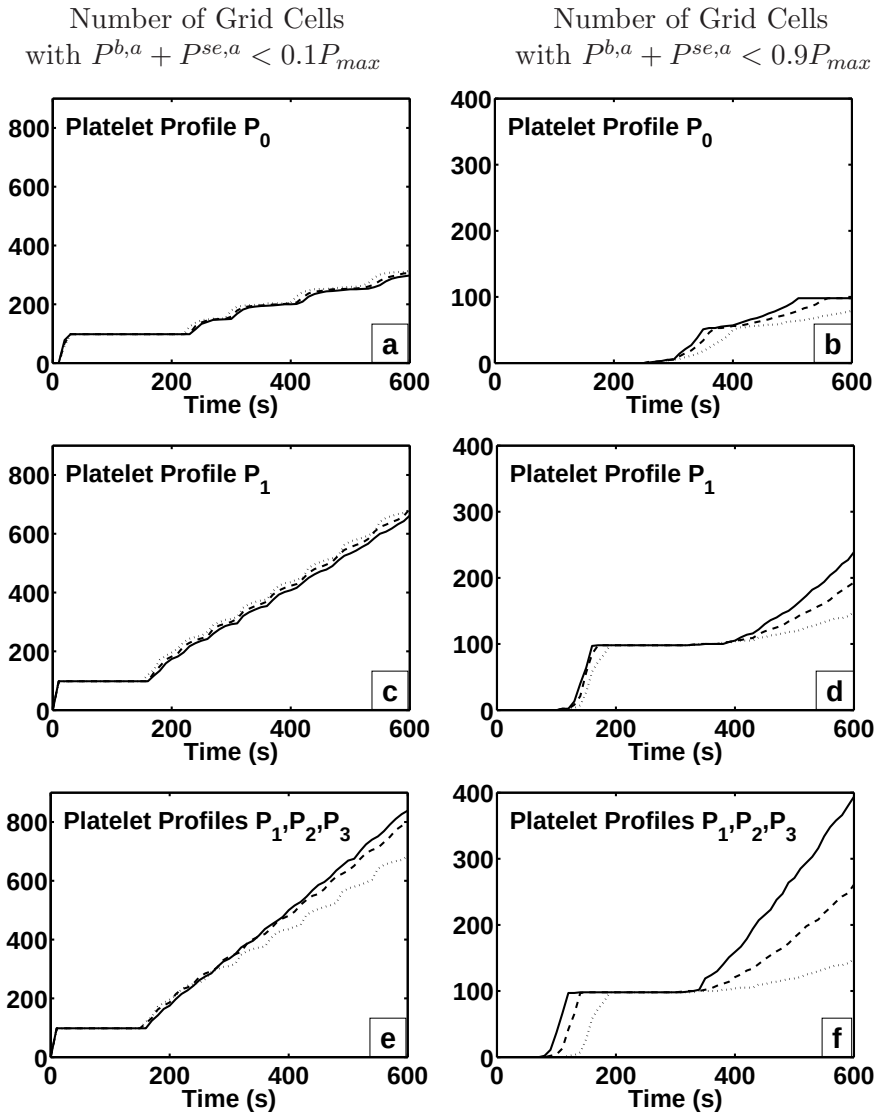


**Figure 3.7**. Clot 'area' for each set of experiments: uniform platelet profiles (top row, a-b), fixed nonuniform platelet profiles (middle row, c-d) and varying nonuniform profiles (bottom row, e-f). In all cases the dotted line, dash-dot line and solid line represent wall shear rates 500, 1000 and 1500 $\text{sec}^{-1}$ respectively.

500-1500 $s^{-1}$. Hence we looked at the effect of shear rate on thrombus growth both for a nonuniform profile that was the same for all shear rates, and for a sequence of nonuniform profiles in which the peak-to-center concentration itself increased with shear rate. The results for a fixed profile and increasing shear rate (Figure 3.6 and 3.7) show that changing the shear rate alone is not a factor in determining the overall size of the thrombus, but that it does impact the size and distribution of high density regions within the thrombus. Figure 3.7d shows an increase in area of high density (>90%) and the images in the second row of Figure 3.6 show that new high density regions develop in the more central portions of the thrombus as the shear rate increases. A possible explanation for this relies on the fact that, with increases in shear rate, both the delivery of platelets to the upstream end of the thrombus and their advection within the thrombus are higher. Thus more platelets may enter the upstream end of the thrombus and be carried to its central portions before the density of bound platelets at the upstream end increases sufficiently to block further platelet transport through this portion of the thrombus.

As the near-wall platelet excess concentration becomes more pronounced, either because of changes of shear rate (Figure 3.6 bottom row) or not (Figure 3.6 right column), both the density of bound platelets within the thrombus and the overall size (area) of the thrombus increase. In both of these sets of experiments, the advective flux of platelets to the injury increases. There is not, however, a simple relationship between the advective flux of platelets to the injury and the growth of the thrombus. This flux is the product of the local concentration of platelets and the local velocity of the fluid, so that the same flux results from different combinations of concentration and velocity that vary in inverse proportion to one another. Equal platelet fluxes do not necessarily imply equal thrombus growth. This is illustrated in Figure 3.6f and h. The ratio of the (initial) platelet flux in the simulation depicted in Figure 3.6f to that depicted in Figure 3.6h is about 6/5 (velocity ratio 3/2, concentration ratio about 4/5), yet the overall size of the thrombus and the size of the high-density region are greater in Figure 3.6h.

To investigate this flux relationship further, we simulated two cases in which the advective flux of platelets arriving at the injury site, concentration times velocity, was equal. We tried one case with higher velocity and lower platelet concentration (wall shear rate of 1500 with platelet profile $P_1$) and another case with lower velocity and higher platelet concentration (wall shear rate of 1056 with platelet profile $P_3$). Figure 3.8 shows the concentration of bound platelets after 10 minutes of clotting activity.

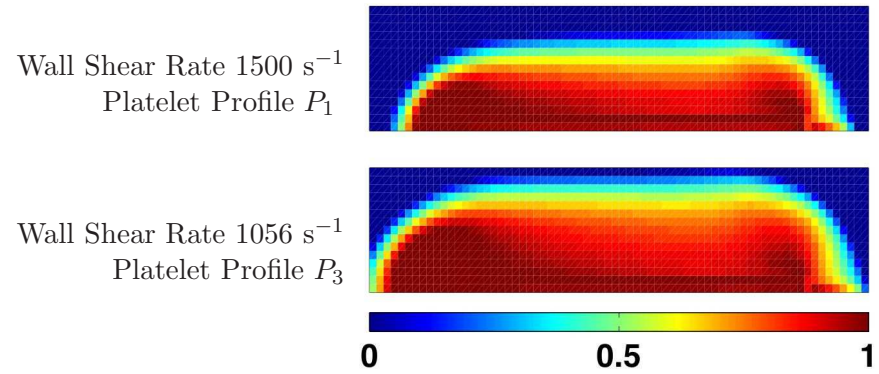


**Figure 3.8**. Bound platelet concentrations after 10 minutes of clotting activity for two cases with equal advective flux of platelets to the injury site. Close-up of approximately 131 $\mu$m long by 30 $\mu$m high region around thrombus. Bound platelet concentrations vary from 0 (dark blue) to $P_{max}$ (dark red). Wall shear rates are 1500 s$^{-1}$ (top) and 1056 s$^{-1}$ (bottom) and the platelet profiles are $P_1$ (top) and $P_3$ (bottom).

The platelet mass is larger in the bottom panel of Figure 3.8 where the platelet profile (platelet concentration near the wall) is higher. This is further confirmed by using the quantitative counting method for the clot 'area' as we did earlier. Indeed, Figure 3.9a shows that there are more grid cells in which the bound platelet concentration exceeds 10% of $P_{max}$ for the case of higher platelet concentration, indicating that the overall size of the thrombus was larger. In fact, Figure 3.9b shows that the density of the clot in the case of higher platelet concentration near the walls was also higher.

The development and maintainance of an enhanced near-wall platelet concentration is

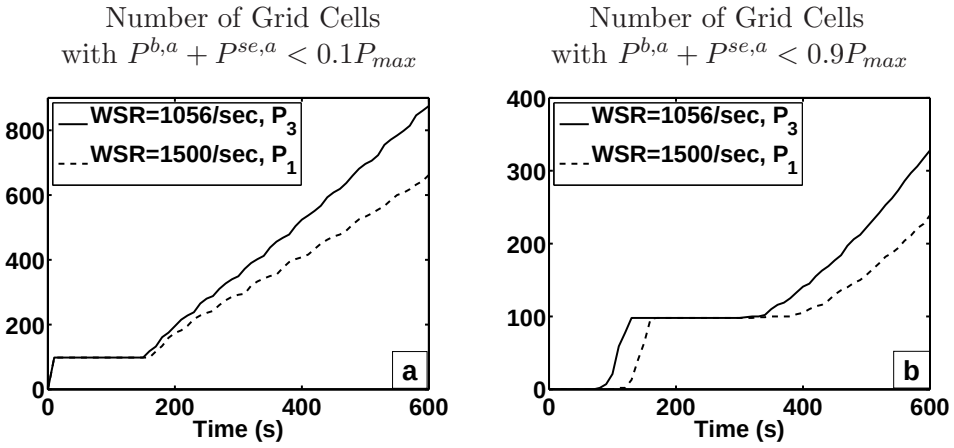


**Figure 3.9**. Clot 'area' for the advective flux comparison. Panels a and b show plots of the number of grid cells where the sum $P^{b,a}+ P^{se,a}$exceeds 10% and 90% of $P_{max}$, respectively.

the result of motion of red blood cells. Since, we do not explicitly include red blood cells in our model, we instead prescribe the concentration profile for incoming platelets. For simulations in very long segments of a vessel, platelet diffusion would eventually cause the platelet profile to become close to uniform. This is not a serious issue in our simulations because the diffusion distance for the time it takes near-wall fluid to traverse the 240 $\mu$m long domain is only about 1 $\mu$m and so the profiles remain sharp throughout the domain.

## 3.3 Platelet Activation by Chemical Agonists

In the model, platelets can be activated by two fluid-phase chemical agonists, ADP and thrombin. To explore the importance of each activating mechanism at different times and locations we tracked the following two quantities:

$$P_{act}^{e_2}(\mathbf{x},t) = \int_{t-10}^{t} A_1(e_2(\mathbf{x},t'))P^{m,u}(\mathbf{x},t')dt', \tag{3.1}$$

and

$$P_{act}^{ADP}(\mathbf{x},t) = \int_{t-10}^{t} A_2([ADP](\mathbf{x},t'))P^{m,u}(\mathbf{x},t')dt'. \tag{3.2}$$

Here, $P_{act}^{e_2}(\mathbf{x},t)$ and $P_{act}^{ADP}(\mathbf{x},t)$ (shown in Figure 3.10 for t = 10, 120, 360, 480, and 600 seconds) are the number per unit volume of platelets activated at location $\mathbf{x}$ during the time interval $t-10$ to $t$ by thrombin and ADP, respectively. Activation by ADP dominates during early thrombus formation (up to about 150 seconds) before substantial thrombin is produced. Its effectiveness peaks during this period at about 20 seconds and then decreases. As the effect of ADP declines, that of thrombin grows because of increases in the thrombin concentration. Thrombin remains the dominant activator during the remainder of thrombus development, but the increased rate of platelet activation increases the rate of ADP release, which, in turn, causes a resurgence in ADP-induced activation, particularly at the upstream end of the thrombus.

Mobile unactivated platelets become activated by ADP or thrombin at rates that depend on the concentrations of these agonists. Once activated, mobile platelets can bind to platelets already part of the thrombus. It is upon binding to the thrombus (or subendothelium) that a platelet becomes procoagulant (*i.e.*, supports coagulation reactions on its surface) and its ADP secretion begins. While this may be a limitation in the model, it is not a serious one because activated platelets which remain unbound are rapidly carried downstream by the flow.

Prothrombinase, the enzyme complex that activates prothrombin to thrombin is a platelet-bound complex. Therefore, thrombin production depends on the concentration

of bound activated platelets. Since prothrombin is abundant in the plasma, thrombin production continues provided there are prothrombinase and binding sites available for prothrombin to bind.

ADP, by contrast, is nonrenewable in the sense that each platelet carries a finite amount of ADP which it can secrete into the plasma. Since fluid-phase ADP is rapidly removed by the flow, the concentration of ADP at a specific location depends largely on the *rate* that platelets bind to the thrombus, not on the accumulated number of platelets already in the thrombus. Platelets rapidly adhere to the subendothelium during early thrombus development, so large amounts of ADP are secreted there and ADP-induced platelet activation is important during this period. The rate at which ADP-activated platelets bind to the thrombus peaks between 50-70 seconds at $\approx 5(10)^4$ platelets/(mm$^3$·sec), and this binding contributes to the early growth of the thrombus into the lumen. The initial burst of platelet activation by ADP is short-lived because of ADP's removal by flow and the slowing of platelet adhesion as coverage of the subendothelium progresses. The next burst of platelet activation, this time due to thrombin, between 150 and 240 seconds (see Figure 3.10) leads to another round of ADP secretion and ADP-induced activation. Together these

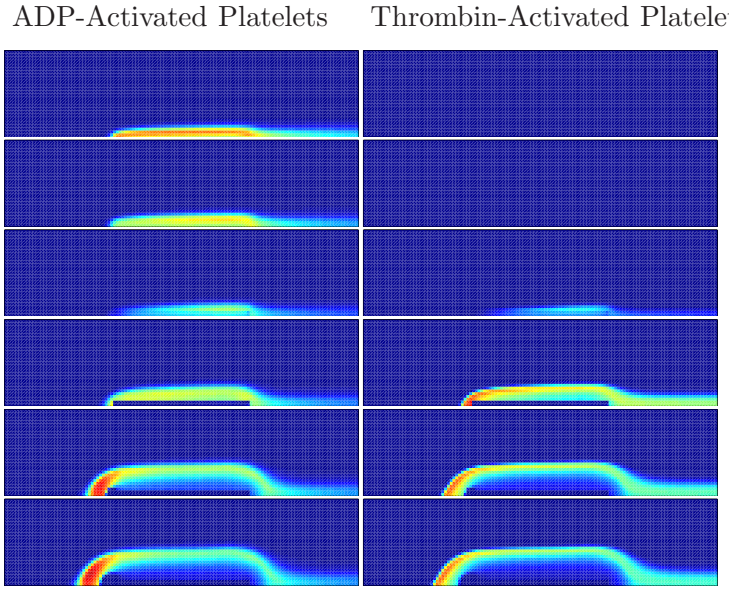


**Figure 3.10**. Activation of platelets by ADP (left) and thrombin (right) in the previous 10 second interval. The rows from top to bottom are for times 10, 60, 150, 240, 480, and 600 seconds. Shear rate 500 s$^{-1}$, platelet profile $P_1$, TF density 15 fmol/cm$^2$. Platelet activation is shown in densities from 0 (dark blue) to 4 (dark red) times $10^4$ platelets per mm$^3$ for ADP and 0 (dark blue) to 4 (dark red) times $10^5$ platelets per mm$^3$ for thrombin.

lead to substantial growth of the thrombus. However, platelet activation by ADP and the binding of ADP-activated platelets to the thrombus have a relatively small affect on the overall thrombus size. This may be due in part to the relatively large activation threshold response (2 $\mu m$) of platelets to ADP used in the model simulations.

The spatial distribution of the agonist-induced platelet activation is also interesting. Initial deposition of platelets and hence ADP secretion and platelet activation, are relatively uniform along the injury. Platelets activated near the downstream end of the injury have less opportunity to bind to the thrombus than those activated upstream because a substantial fraction of them is carried downstream (see Figure 3.10). Later in the simulation, most of the chemical activation (by ADP and thrombin) occurs at the upstream end of the thrombus. A platelet activated there may bind there contributing to upstream growth or it may be carried into or over the thrombus binding downstream and contributing to upward growth of the thrombus or increased thrombus density.

## 3.4 Porosity and Intrathrombus Transport

As a thrombus grows, it offers more resistance to the flow and the bulk of the flow is diverted around the thrombus. But, because a thrombus is porous, fluid motion within the thrombus persists albeit at a velocity much less than that outside of the thrombus. To investigate the effect that porosity and flow resistance has on the growth of the thrombus, we carried out simulations of 10 minutes of clotting activity for three different values of the porosity coefficient, $\alpha_{max} = 40$, 400, and 4000, each with a wall shear rate of 500 $s^{-1}$. In each case, as the first platelets adhere to the subendothelium the velocity within the early thrombus becomes very small. As seen in Figure 3.11, the velocity of the fluid within the thrombus increases, because the thrombus grows and occludes more of the vessel and pressure builds up at the front edge of the thrombus, reaching a magnitude on the order of 0.1-10 $\mu$m/s (depending on $\alpha_{max}$). This is the velocity at which fluid-phase chemicals inside the thrombus advect. However, recalling the platelet-density-dependent limitation on platelet advection, platelets move at reduced velocities (see Figure 3.12), in particular, where the density of bound platelets is high.

Although fluid velocities inside a partially-developed thrombus are small relative to those in the bulk flow around the thrombus, they are large enough to carry fluid-phase chemicals the entire length of the injury within 30-90 seconds (see Figure 3.13).

However, fluid-phase species may also be transported by diffusion. To explore the

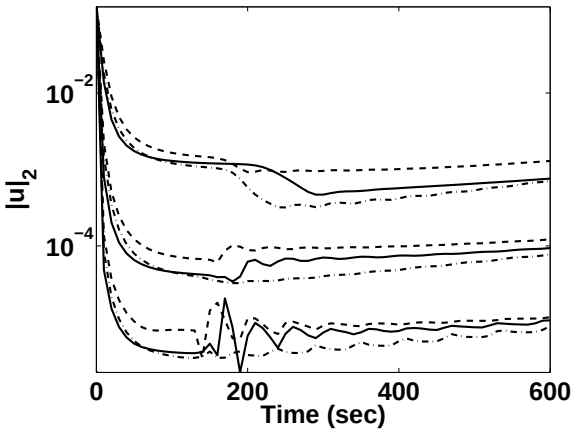


**Figure 3.11**. Flow speed (cm/s) inside the thrombus approximately 1 $\mu$m from the vessel wall. The curves correspond to locations about 8 $\mu$m from the upstream end (solid), at the middle (dash-dot), and about 8 $\mu$m from the downstream end of the injury (dashed), respectively. The three groups of curves, from top to bottom, represent simulations performed using $\alpha_{max}$ = 40, 400, and 4000, respectively. Wall shear rate is 500 $s^{-1}$, the platelet profile is $P_1$ and the initial TF density is 15 fmol/$cm^2$.

relative influence of advective and diffusive transport, we use the nondimensional Peclet number, $Pe = uL/D$. We define a Peclet number at each point $\mathbf{x}$ in the thrombus using the magnitude of the velocity at that point, the species' diffusion coefficient $D$, and the length $L = 90$ $\mu$m of the injury.

Figure 3.14 shows spatial plots of $1/Pe(\mathbf{x}, t)$ for $\alpha_{max}$=40, 400, and 4000, and demonstrates that diffusion is more effective than flow at moving chemical species at certain times during the simulation. These plots do not give information about the *direction* of movement, but, as we explain shortly, some of this movement is indeed upstream against the direction of the flow. The velocities within the thrombus increase starting at about time 150-250 seconds (depending on $\alpha_{max}$, see Figure 3.11), and the value of $1/Pe$ and, with it, the relative influence of diffusion to advection decreases after that time.

The time at which $1/Pe$ is highest (*i.e.,* when the intra-thrombus velocity is lowest) is crucial for the formation and spread upstream of the important platelet-bound enzyme complexes. Figure 3.15 shows spatial concentrations (nM) of eight different platelet-bound chemical species that are vital to thrombin formation and, thus, thrombus growth, for the case where $\alpha_{max} = 400$. The columns in Figures 3.15 and 3.16 represent the times 140, 180, and 250 seconds, respectively. At 140 seconds, there are substantial amounts of the platelet-bound zymogens, $Z_5^m$, $Z_8^m$, and $Z_{10}^m$, present everywhere within the thrombus. A

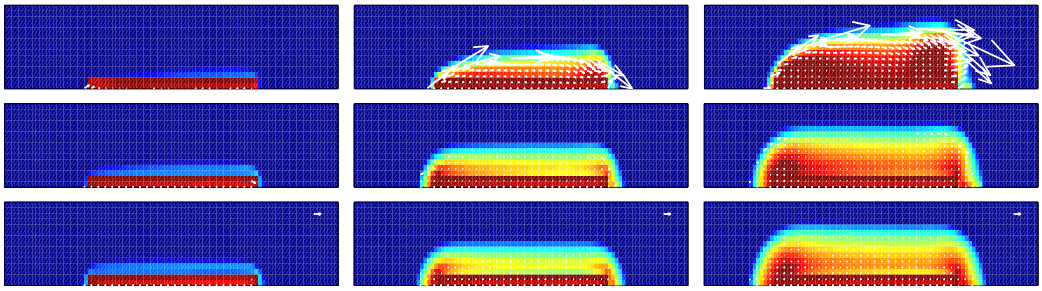

**Figure 3.12**. Bound platelet concentrations with an overlay of the mobile platelet velocity vectors for three different values of $\alpha_{max}$ at three distinct time points. Close-up of near thrombus region at times 200, 400, and 600 seconds (left to right) for $\alpha_{max} = 40$, 400, and 4000 (top to bottom). Velocity vectors represent platelet velocities scaled relative to the 10 $\mu$m/s vector shown in the upper-right corner of the bottom plots. The velocity vectors only appear in regions where the bound platelet concentration exceeds $1{\times}10^7$ platelets/mm$^3$ and the nondimensional concentration of the virtual substance, $\eta$, exceeds 0.27. Bound platelet concentrations vary from 0 (dark blue) to $P_{max}$ (dark red).

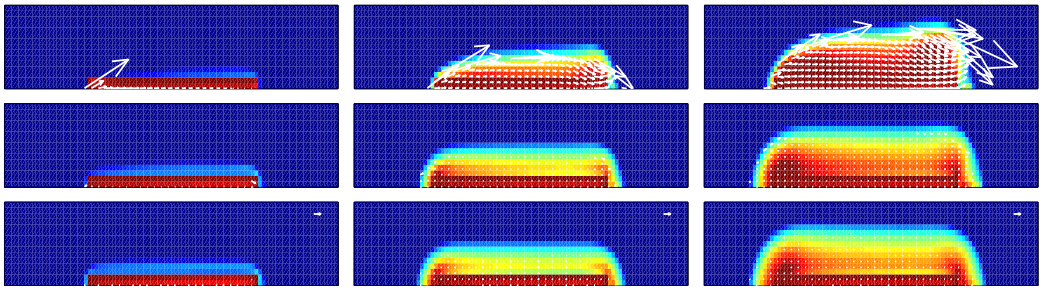

**Figure 3.13**. Bound platelet concentrations with an overlay of the fluid velocity vectors for three different values of $\alpha_{max}$ at three distinct time points. Close-up of near thrombus region at times 200, 400, and 600 seconds (left to right) for $\alpha_{max} = 40$, 400, and 4000 (top to bottom). Velocity vectors represent fluid velocities scaled relative to the 10 $\mu$m/s vector shown in the upper-right corner of the bottom plots. The velocity vectors only appear in regions where the bound platelet concentration exceeds $1{\times}10^7$ platelets/mm$^3$ and the nondimensional concentration of the virtual substance, $\eta$, exceeds 0.27. Bound platelet concentrations vary from 0 (dark blue) to $P_{max}$ (dark red).

small quantity of platelet-bound thrombin ($E_2^m$) can be seen in the downstream portion of the thrombus in the region where prothrombinase (PRO) is present. The enzyme $E_9^m$, which only appears when the activated fluid-phase enzyme $E_9$ (IXa) binds weakly to platelets, is also found in the downstream region. The small amount of thrombin is apparently sufficient to activate $Z_8^m$ to $E_8^m$, which rapidly binds to $E_9^m$ to form the tenase (TEN) complex.

This happens only at the downstream end of the thrombus because that is where

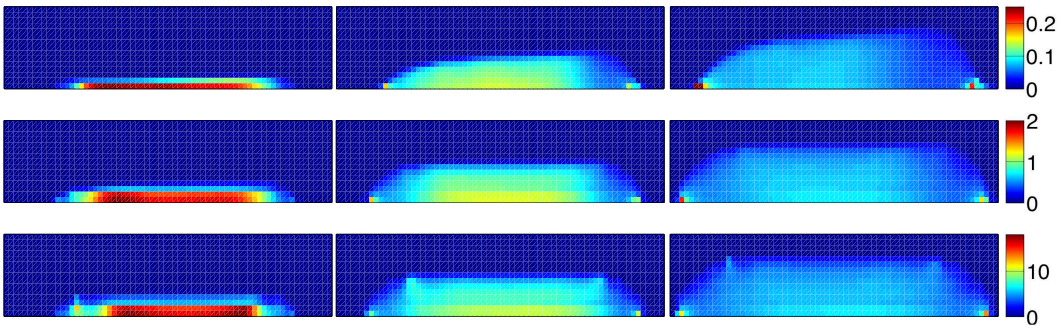


**Figure 3.14**. Spatial plots of $1/Pe$ using three different values of $\alpha_{max}$ at three different time points. The color bar scales across each row. The plots show times 200, 400, 600 seconds (left to right) and $\alpha_{max}$=40, 400, and 4000 (top to bottom).

thrombin and $E_9^m$ are found. Since the platelet-bound zymogen $Z_{10}^m$ is also abundant there, the tenase complexes produce substantial platelet-bound Xa ($E_{10}^m$) in the downstream portion of the thrombus. In addition to activating $Z_8^m$ to $E_8^m$, the thrombin in this portion of the thrombus activates $Z_5^m$ to $E_5^m$, which together with the $E_{10}^m$ produced by the tenase complexes, forms new prothrombinase complexes, which, in turn, produce more thrombin. Up to this time, factor Xa made at the subendothelial surface by TF:VIIa has been largely responsible for thrombin production; it has been the dominant activator of platelet-bound $E_5^m$, and it has combined with the $E_5^m$ molecules to form prothrombinase. With the formation of substantial numbers of tenase complexes in the downstream portions of the thrombus, another powerful source of $E_{10}^m$ comes into play, while thrombin takes over as the dominant activator of $E_5^m$.

By 180 seconds, both Xa and thrombin have diffused a small distance upstream, binding and unbinding from the bound platelet surfaces as they move. The thrombin activates almost all of the platelet-bound zymogens $Z_5^m$ and $Z_8^m$ on the platelets it reaches, and the Xa binds to the platelets and forms prothrombinase complexes with the newly activated $E_5^m$. Thus, the availability of prothrombinase moves upstream through the thrombus as a consequence of upstream diffusion of thrombin and Xa from their downstream sources against the weak flow then present in the thrombus. By time 250 seconds, the effect of diffusion is even more apparent. Tenase is still found predominantly at the downstream end of the thrombus, but both platelet-bound Xa and prothrombinase are found in the upstream portions of the thrombus.

Although we only show these eight important species for the case where $\alpha_{max} = 400$,

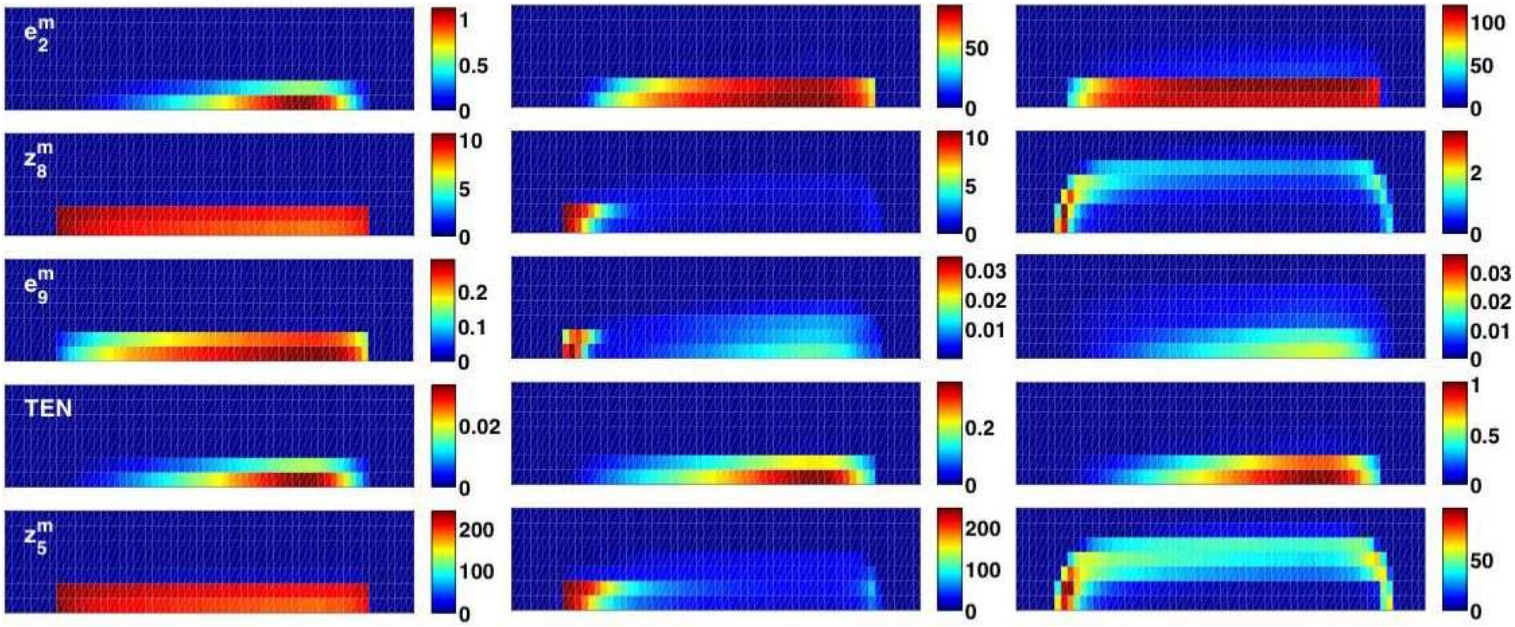


**Figure 3.15**. Spatial concentrations of five platelet-bound chemicals vital to thrombin formation at three different time points. Close-up of 120 $\mu$m long by 15 $\mu$m high region around thrombus at times 140, 180, and 250 seconds in left, middle, and right columns respectively. In each column are shown (top to bottom) spatial concentrations (nM) of platelet-bound chemical species thrombin $e_2^m$, $z_8^m$, $e_9^m$, TEN (tenase), and $z_5^m$. Wall shear rate is 500 $s^{-1}$, the platelet profile is $P_1$, and the initial TF density is 15 fmol/cm$^2$.

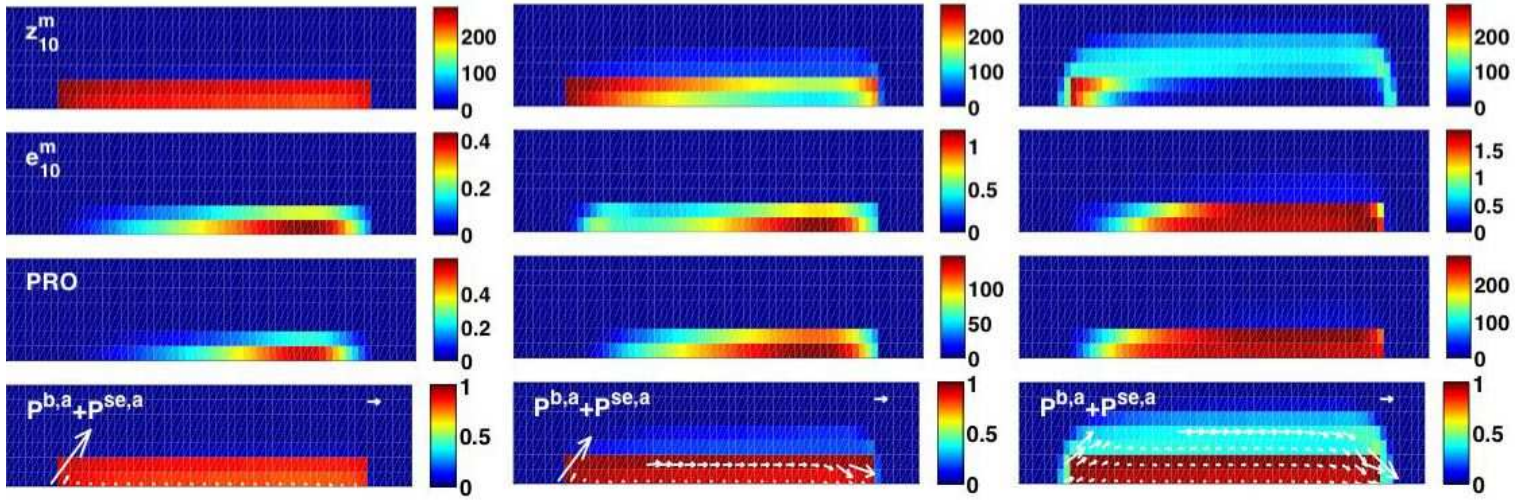


**Figure 3.16**. Spatial concentrations of three platelet-bound chemicals vital to thrombin formation and bound platelet concentrations at three different time points. Close-up of 120 $\mu$m long by 15 $\mu$m high region around thrombus at times 140, 180, and 250 seconds in left, middle, and right columns respectively. In each column are shown (top to bottom) spatial concentrations (nM) of platelet-bound chemical species $z^m_{10}$, $e^m_{10}$, and PRO (prothrombinase), as well as the bound platelet concentration (fraction of $P_{max}$) and intra-thrombus velocity (velocity scale vector 2 $\mu$m/s). Wall shear rate is 500 $s^{-1}$, the platelet profile is $P_1$, and the initial TF density is 15 fmol/$cm^2$.

the same behavior is indeed seen for all of the $\alpha$ cases, although they occur at different times. The Peclet number is higher ($1/Pe$ is lower) for the smallest value of $\alpha_{max}$, since the flow within the thrombus is less inhibited, and since the diffusion coefficient is not changed in these experiments, it is clear that the upstream diffusion, if any, will take longer as the value of $\alpha_{max}$ is decreased. This is seen in Figure 3.17 where we plot the platelet-bound species tenase, prothrombinase, and $e_{10}^m$ for the three values of $\alpha_{max}$. Each column represents a different $\alpha_{max}$ and a different point in time (350 seconds for $\alpha_{max}$=40, 300 seconds for $\alpha_{max}$=400, and 250 seconds for $\alpha_{max}$=400), while each row represents the spatial concentration (nM) or tenase (a-c), prothrombinase (d-f) and $e_{10}^m$ (h-i). In each column, tenase is mostly downstream while platelet-bound Xa and prothrombinase are found in the upstream portions of the thrombus.

The different distributions of platelet-bound species for different values of $\alpha_{max}$ seem to have a profound effect on the overall shape of the formed thrombus. Recalling the bound platelet distributions after 10 minutes of clotting activity for each of the $\alpha_{max}$ cases (Figures 3.12 and 3.13), the smaller $\alpha_{max}$ shows significantly more downstream thrombus growth and less upstream growth. This is partly due to larger Peclet number but also to the fact that the higher intra-thrombus velocities (both platelet and fluid) introduce more platelets and chemicals to the injury site and also farther into the interior of the growing thrombus.

The porosity of the thrombus is a model outcome; it evolves in space and time as a result of processes whose dynamics, themselves, depend on the porosity. Platelets transported into the thrombus may not be activated until they reach a chemical agonist far within the interior, and, depending on $\alpha_{max}$, reach different distances within the thrombus. In all cases, however, as activated platelets are incorporated into parts of the thrombus, those parts become more dense and their permeability and the flow within them decrease, therefore restricting more flow or platelets from entering. This is apparent in the first 60 seconds when, because of platelet adhesion to the subendothelium, the near-wall velocity above the injury decreases by orders of magnitude. The time that the flow speed at the center of the injury is at its minimum is, interestingly, the precise time when thrombin begins to make a major appearance. The reduction in velocity, although it occurs at different times depending of thrombus porosity, aids in the sharp increase in thrombin production by allowing the enzymes, $E_9$ in particular, to remain within the thrombus for extended periods after their production. Moreover, our Peclet number studies revealed

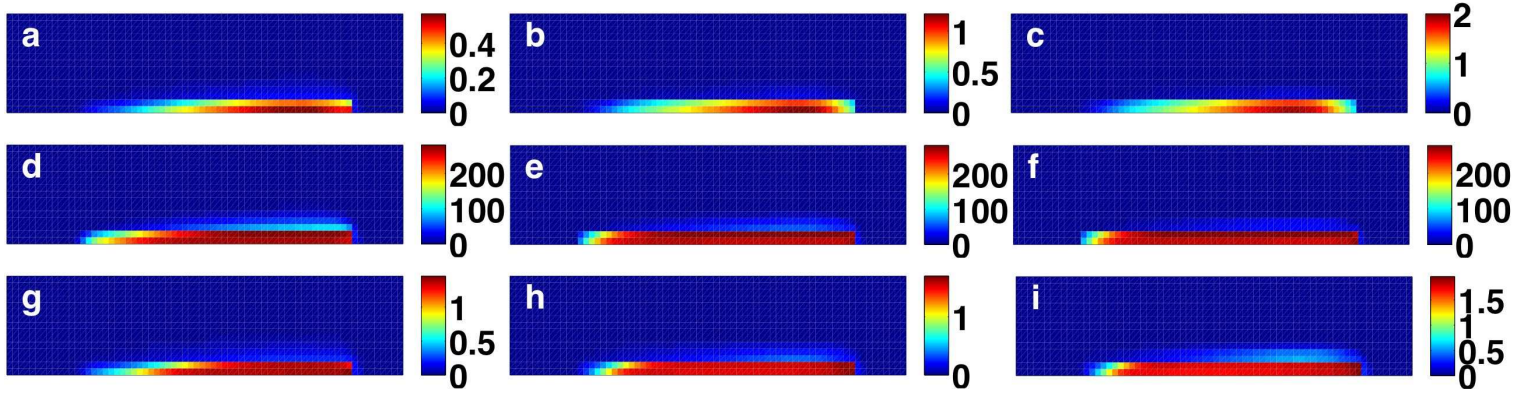


**Figure 3.17**. Spatial concentrations of tenase, prothrombinase, and platelet-bound factor Xa for three different values of $\alpha_{max}$ at three different time points. Close-up of region around thrombus at times 350 (left column), 300 (middle column), and 250 (right column) seconds. The column from left to right also represent the three different values $\alpha_{max}$= 40 (left), 400 (middle) and 4000 (right). The rows show the spatial concentrations (nM) of platelet-bound chemical species tenase (a-c), prothrombinase (d-f), and $e_{10}^m$ (g-i). Wall shear rate is 500 $s^{-1}$, the platelet profile is $P_1$, and the initial TF density is 15 fmol/$cm^2$.

that diffusional transport was extremely important in upstream prothrombinase formation and thus thrombin production and further thrombus growth. The combined effects of increased contact times due to the reduction in velocity and diffusional transport of species upstream cause substantial enhancement in the development of the thrombus.

## 3.5 Flow Boundary Conditions

In the simulations reported in this chapter, we specify the velocity profile (hence the volumetric flow rate) at the inlet to the computational domain. In many laboratory experiments, a pump is used to impose a constant volumetric flux, so our simulations can be compared directly with such experiments. However, it is unclear whether these are the most appropriate flow boundary conditions for simulations of *in vivo* thrombus formation. It is inappropriate to drive the flow through the short vessel segment we simulate by imposing a constant pressure drop over that length that remains constant for the duration of the simulation. The reason is that as the thrombus grows, flow in the longer vessel, of which the computational domain is regarded to be a piece, slows and the pressure drop over the shorter segment actually increases. An alternative procedure is as follows: let the computational domain represent a small portion of a longer vessel over which the pressure drop is constant. In this case, we would indeed drive the flow with a pressure drop, but use a relationship (derived and used in [20]) between the flux and pressure drop across just the computational domain, while holding the pressure drop across the longer vessel fixed. We tried this method by running our simulation with a wall shear rate of 500/s, a TF density of 15 fmol/cm$^2$, and the platelet profile $P_1$. We used boundary conditions derived from this pressure-flow relationship and found that the results differed by less than one percent with the case of fixed inflow and Neumann outflow.

## 3.6 Limitations and Extensions

Most of the model parameters have been previously estimated from the experimental literature [38]. Two new parameters about whose values we are less certain are the cohesion rate, $k_{coh}$, and the maximum resistance to flow within the thrombus, $\alpha_{max}$. The parameter $k_{coh}$ represents the rate of binding between two platelets already in relative positions that allow them to bind. We know of no comparable measurements in the literature. A fixed value of this parameter was used for all of the simulations reported in this chapter. In the following chapter, a limited set of simulations are carried out in which we use a 10-fold

lower and 100-fold higher value for both $k_{coh}$ and $\alpha_{max}$. It is also of interest to explore the model's behavior if $k_{coh}$ is made to depend on the local shear rate. In particular, this may change the linear rate of thrombus growth seen in Fig. 3.7(d-i). We discuss this further in Chapter 8.

In reference to $\alpha_{max}$, which is the reciprocal of permeability, there are few measurements of thrombus permeability in the literature and none of these pertains to the permeability of a thrombus during its early stages of development. At times beyond those of interest in our simulations, the active process of 'clot retraction' pulls platelets into close proximity and squeezes out much of the fluid between the platelets. Hence we expect 'old' thrombi to be much less porous than newly forming ones. One value for thrombus permeability we found in the literature is for thrombi extracted from abdominal aortic aneurysms. These develop overs months and are therefore representative of old thrombi. The permeability reported for these thrombi is 0.91 $\pm$ 0.54 mm$^4$/N·s [1]; our middle permeability ($\alpha_{max} = 400$) is about six-fold larger than this, reflecting our belief that the early thrombus is much more porous than an old thrombus. It would be of immense help to have experimental measurements of the permeability of representative thrombi fixed at different relatively short times (e.g., 3, 5, 7 min) during their development.

We also note that the current simulations do not include the effect of the inhibitor APC. APC is produced on the surfaces of endothelial cells by a complex of thrombin and endothelial-bound thrombomodulin. In Chapter 5, we describe how we incorporate endothelial reactions into the model (on surfaces upstream and downstream of the injury), APC production and its action of factors Va and VIIIa.

# CHAPTER 4

# ACCOUNTING FOR THE FINITE SIZE OF PLATELETS

Additional challenges emerge due to the fact that we model platelets as a continuum and not as discrete objects. A fraction of a platelet should be able to survey its immediate environment so that it 'knows' where and when to attach and how to be transported. Otherwise, platelet fractions would cohere and build-up at only one spatial location. To our knowledge, there is no model or mathematical theory to describe platelet-platelet cohesion. We have developed four phenomenological models to represent such behavior within our continuum model.

The first model describes the adhesion of platelets to the subendothelium. The second model describes platelet transport and includes a modification we make to the diffusive and advective flux of the two mobile platelet species, $P^{m,u}$ and $P^{m,a}$. Below, we compare and contrast three different forms of the function, $W(\phi^T)$. Finally, we model platelet-platelet cohesion with the two parameters: $k_{coh}$ and $g(\eta)$. We compare and contrast three separate values of $k_{coh}$ and three separate forms of $g(\eta)$. In all simulations described below, the initial TF density is 15 fmol/cm$^2$, the platelet profile is $P_1$ and the wall shear rate is 500 inverse seconds.

## 4.1 The Spatial Parameter $k_{adh}(\mathbf{x})$

The first phenomenological model describes platelet adhesion and utilizes the spatial function and parameter, $k_{adh}(\mathbf{x})$, that 'tells' platelets when they are close enough to the subendothelium to adhere. We assume that if a platelet fraction is within a platelet diameter from the subendothelium, then it will bind at some rate. The rate we use was estimated from experimental studies conducted by Turitto and Baumgartner (1979) [71] and Turitto *et al.* (1980) [73]. The estimation of this second-order reaction between platelets and binding sites on the subendothelium was developed for the KF model and is

described in [38]. The only difference here is that we assume that this rate is distributed spatially as seen in Figure 4.1.

## 4.2 Three Forms of $W(\phi^T)$

The function, $W(\phi^T)$, is used to modify mobile platelet advection and diffusion. As mentioned in Chapter 2, we multiply the mobile platelet flux vector $\mathbf{J}^{m,u} = \mathbf{u}P^{m,u} - D\nabla P^{m,u}$ by this function $W(\phi^T)$ which depends on the *total* platelet fraction, $\phi^T$. A platelet, but not necessarily fluid, must be hindered from passing through a region of space that is partially filled with an obstacle such as platelets. The platelet masses build up gradually and so the 'obstacle' that hinders the motion of mobile platelets, and thus the function, $W(\phi^T)$, must evolve as the thrombus grows. Where there is no obstacle, the mobile platelets should diffuse freely and advect solely with the fluid. However, at some point, depending on the size and volume fraction of the obstacle, a mobile platelet should be completely restricted from moving through that obstacle. This describes a form for $W(\phi^T)$: a monotonically decreasing function of the total platelet fraction with $W(0) = 1$ and $W(1) = 0$. There are numerous functions that satisfy these conditions so we choose three different forms to see how they alter the behavior and results of the model.

The three shapes we chose for the function $W(\phi^T)$ are shown in Figure 4.2. The dashed line (the function we use to produce all of the results in Chapters 3 and 5), which we denote $W_1$, has a shape for which we have assumed the ability of mobile platelets to move into a region is gradually impaired until $\phi^T$ reaches approximately 0.5, and then drops quickly.

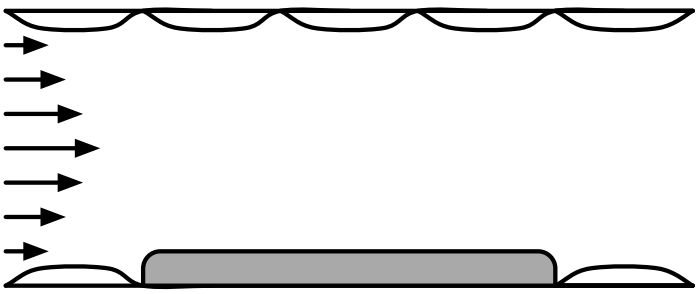

**Figure 4.1**. Depiction of the parameter, $k_{adh}(\mathbf{x})$. This parameter is assumed to be a positive constant for spatial points $\mathbf{x}$ within one platelet diameter's distance of the subendothelium (shaded in gray) and zero elsewhere.

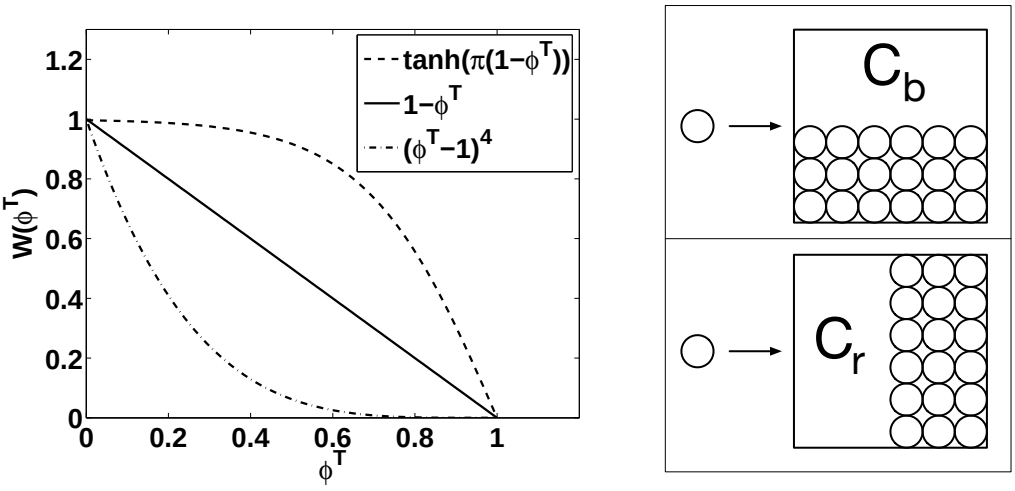


**Figure 4.2**. Left: three different shapes for the function $W(\phi^T)$, $W_1$ (dashed), $W_2$ (solid) and $W_3$ (dash-dot). Right: two extreme cases of spatial configurations of 'platelets' where the volume fraction is 0.5. $C_b$ depicts the case where all 'platelets' are at the bottom half of the cell and $C_r$ depicts the case where all 'platelets' are located in the right half of the cell.

The other choices are a linear decay ($W_2$) and one in which we assume the ability of mobile platelets to move into a region is quickly impaired initially, and then gradually decays to zero ($W_3$).

In Figure 4.3, we show the bound platelet concentrations that develop when using each of the three $W(\phi^T)$ functions, after 10 (left panel) and 20 (right panel) minutes of clotting activity. It is clear that using $W_1$ allows for more platelets to enter a region initially, become activated and cohere inside the growing thrombus, which produces a denser thrombus. On the other hand, using $W_3$ produces a thrombus that is about half of $P_{max}$ everywhere in its interior, as mobile platelets are hindered from entering.

The platelet motion must be hindered in some way by the nearby bound platelets, but modeling the relationship that is 'most realistic' is both novel and challenging. To illustrate this, we imagine the possible platelet configurations that could form in a square region, or cell, half-filled with platelets, with the idea in mind that platelets arrive from the left with the flow and deposit on the bottom. Two platelet configurations are initially considered (see the right hand side of Figure 4.3): the bottom of the square is half-filled ($C_b$), through which a platelet could move fairly easily, and the right side of the square is half-filled ($C_r$), through which a platelet could not move. The choice to use $W_3$ in the model amounts to making the assumption that most configurations of bound platelets, when the volume

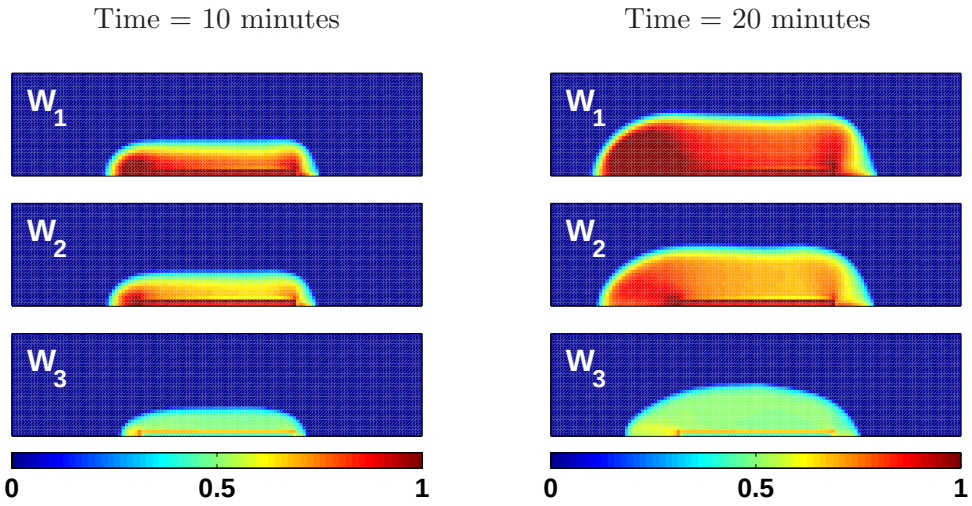


**Figure 4.3**. Bound platelet concentrations after 10 (left panel) and 20 (right panel) minutes of clotting activity vary from 0 (dark blue) to $P_{max}$ (dark red). From top to bottom, the choice for $W(\phi^T)$ is $W_1$, $W_2$, and $W_3$, respectively. Wall shear rate is 500 $s^{-1}$, the platelet profile is $P_1$ and the initial TF density is 15 fmol/$cm^2$.

fraction is near one half, is similar to that of $C_r$. On the other hand, the configuration $C_b$ might not hinder a mobile platelet at all. The platelets nearest the wall arrive at the injury and essentially hit a 'wall' (as in $C_r$), become activated if chemical activator is present and cohere. Many mobile platelets do not hit the wall, but instead flow over the clot and may encounter a situation more like that of $C_b$. Furthermore, a mobile platelet may also move through the interior of the porous thrombus, encountering an obstacle that is a combination of the two in $C_b$ and $C_r$. This logic ruled out the choice of $W_3$ in our model, and left us with either $W_1$ (hyberbolic tangent) or $W_2$ (linear). We chose $W_1$ because we can think of more configurations that would hinder the motion of a platelet volume fraction of 0.5 for $W_1$ over $W_2$. We show the results from all three choices for completeness.

## 4.3 Platelet-Platelet Cohesion: $k_{coh}$ and $g(\eta)$

Although there has been numerous experiments that have studied the adherence of platelets to collagen-covered surfaces and platelet aggregation, to our knowledge, there is no definitive platelet-platelet cohesion 'rate' that has been (or can ever be) quantified. Platelet-platelet binding is complicated and involves two important plasma glycoproteins von Willebrand factor (vWF) and fibrinogen. An excellent review on the interactions of platelets with these glycoproteins can be found in [64]. Our model does not include detailed

treatment of the complex interactions between platelets and these proteins. Instead we assume a second-order binding reaction between a given mobile platelet and bound platelets that depend on the number of bound activated platelets near the mobile one.

The evolution equations for the mobile activated and bound activated platelets ($P^{m,a}$ and $P^{b,a}$) both include the term: $k_{coh}g(\eta)P_{max}P^{m,a}$. We assume that the cohesion is a second-order binding reaction and the parameter $k_{coh}$ is the binding rate. The 'binding affinity' function, $g(\eta)$, allows the cohesion to occur at a rate that depends on the number of nearby bound activated platelets, where the function $\eta(\mathbf{x}, t)$ is used to indicate both proximity to bound platelets and the density of nearby bound platelets. We have investigated how the rates and behavior of $g(\eta)$ affect the thrombus growth process by using different values of $k_{coh}$ and shapes of the function $g(\eta)$. Figure 4.4 shows the bound platelet concentrations after ten minutes of clotting activity where we vary the rate $k_{coh}P_{max}$ from $10^5$ to $10^3$ per second (top to bottom). We note that the middle figure ($k_{coh}P_{max} = 10^3$ per second) is the value used when acquiring the results in Chapters 3 and 5. The smaller value of $k_{coh}P_{max}$ allows fewer platelets to cohere per second which results in a smaller, but denser, thrombus while the larger value of $k_{coh}P_{max}$ causes more platelets to cohere per second, which results in a larger, but less dense, thrombus.

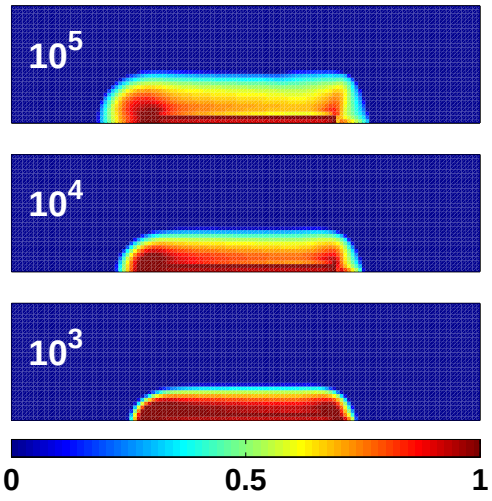


**Figure 4.4**. Bound platelet concentrations after 10 minutes of clotting activity vary from 0 (dark blue) to $P_{max}$ (dark red). From top to bottom, the value of $k_{coh}P_{max}$ is $10^5$, $10^4$, and $10^3$, respectively.

Altering the value of $k_{coh}P_{max}$ and changing the form of $g(\eta)$ will affect the magnitude of the term $k_{coh}g(\eta)P_{max}P^{m,a}$ and thus, the number of platelets that will transition from a mobile activated state into a bound activated state. Furthermore, $g(\eta)$ gives the cohesion dependence on clot density, where the parameter, $k_{coh}P_{max}$, is a constant rate. Changing the form of $g(\eta)$ does not change how the the virtual substance, $\eta$, is secreted but may, however, affect the location at which $\eta$ is secreted by increasing or decreasing the bound platelet concentration by a substantial amount. Figure 4.5 shows the three different forms of $g(\eta)$ that we test in the model. All three forms are zero below the value 0.1 indicating that platelets should not cohere if there are relatively few bound platelets nearby. The top dashed curve ($g_1$) sharply rises around the value $\eta = 0.25$ and then slowly climbs to one. This form of $g_1$ allows mobile activated platelets to bind to the thrombus from a further distance away than the other two forms $g_2$ and $g_3$, basically increasing the binding rate. For example, when $\eta$ is 0.5, which indicates to a mobile platelet that the nearby bound platelet concentration is half $P_{max}$, $g_1$ makes the mobile platelet cohere approximately twice as fast as $g_2$ and four times as fast as $g_3$. This ultimately increases the local value of $\eta$ and thus, $g(\eta)$ itself.

In Figure 4.6, we show the bound platelet concentrations that have developed using each of the three $g(\eta)$ functions, after 10 (left panel) and 20 (right panel) minutes of clotting activity. After 10 minutes, the results are similar to those in Figure 4.4, with the increased

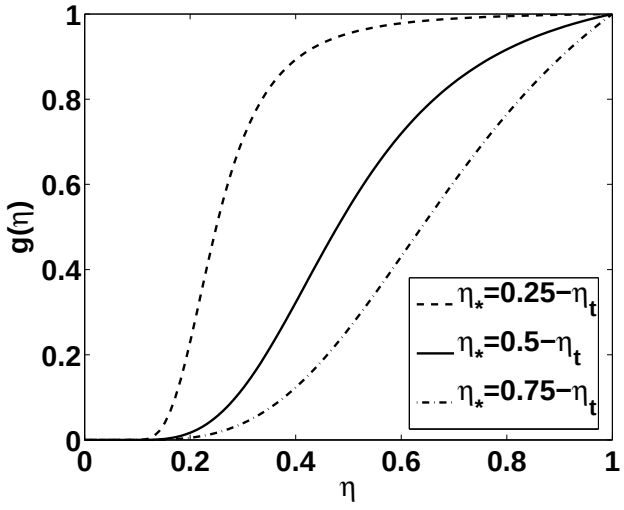


**Figure 4.5**. Three different shapes for the function $g(\eta)$: $g_1$ (dashed), $g_2$ (solid) and $g_3$ (dash-dot).

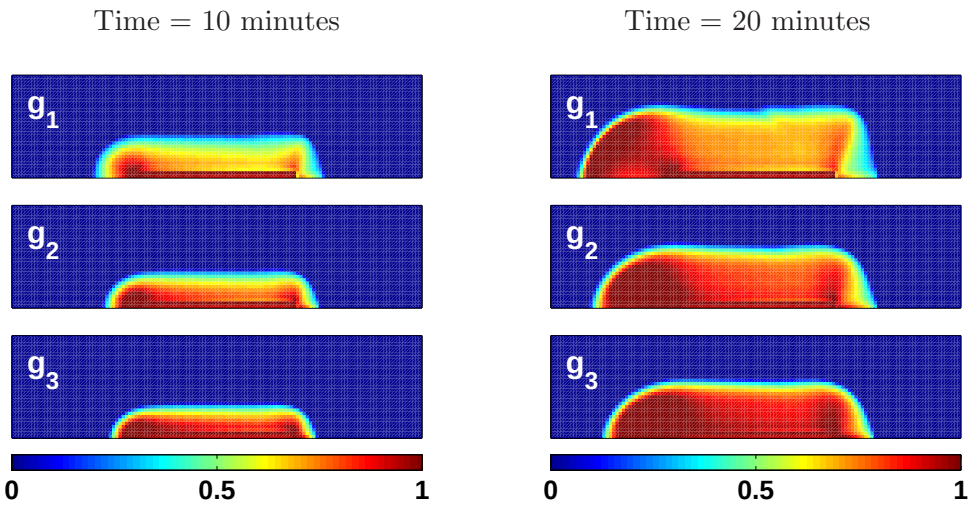


**Figure 4.6**. Bound platelet concentrations after 10 (left panel) and 20 (right panel) minutes of clotting activity vary from 0 (dark blue) to $P_{max}$ (dark red). From top to bottom, the choice for $g(\eta)$ is $g_1$, $g_2$, and $g_3$, respectively.

rate of cohesion ($g_1$ and $k_{coh}P_{max} = 10^5$) developing a larger and less dense thrombus than the other two choices.

The decision to use $g_2$ was a somewhat arbitrary one, but the resulting thrombi in each case are not completely dissimilar either. We chose the 'middle of the road' but made sure that the model was not extremely sensitive to this choice. Again, we have shown the results for all cases for completeness.

# CHAPTER 5

# LONGER VESSEL EXPERIMENTS

With a working spatial-temporal model that gives insight into thrombus formation under flow and intrathrombus transport, we want to learn how a thrombus forming at a particular location might affect the growth of a second thrombus directly downstream. To investigate this, we place two subendothelial regions in a vessel that is twice as long as in the simulations described in previous chapters. In setting up this numerical experiment, we realized that interesting dynamics may emerge between the two growing thrombi, and became curious as to what role an endothelial surface might play in this situation. In this chapter, we first describe how two growing thrombi behave in a long vessel segment and then discuss how the addition of an endothelial surface and the activated protein C pathway affect thrombus growth.

## 5.1 Two Thrombi

Figure 5.1 shows four snapshots from a simulation of 20 minutes of clotting activity. The channel has height 60 $\mu$m, length 480 $\mu$m and there are two injuries, each of length 90 $\mu$m with 90 $\mu$m between them. The Brinkman coefficient, $\alpha_{max}$, is set to 400 and the initial TF density in both injuries is set to 15 fmol/cm$^2$. After 300 seconds, it is already apparent that the second thrombus, or 'downstream' thrombus, is growing differently than the first thrombus, or 'upstream' thrombus and the flow between the two looks relatively undisturbed. By 600 and 900 seconds, the downstream clot has dense protrusions that radiate diagonally at both its front and back edge while the flow in between the two thrombi becomes increasingly sheltered by their growth. Finally, at 1200 seconds, the different growth of the downstream thrombus has persisted, the flow in between seems almost stagnant, and the upstream thrombus has a 'tail' that has formed on its back edge that was not there in the previous one-thrombus simulations (see Figure 4.3).

The growth behavior of the downstream thrombus is somewhat curious at first glance. Since it has some resemblance to the thrombi that formed when we increased the parameter

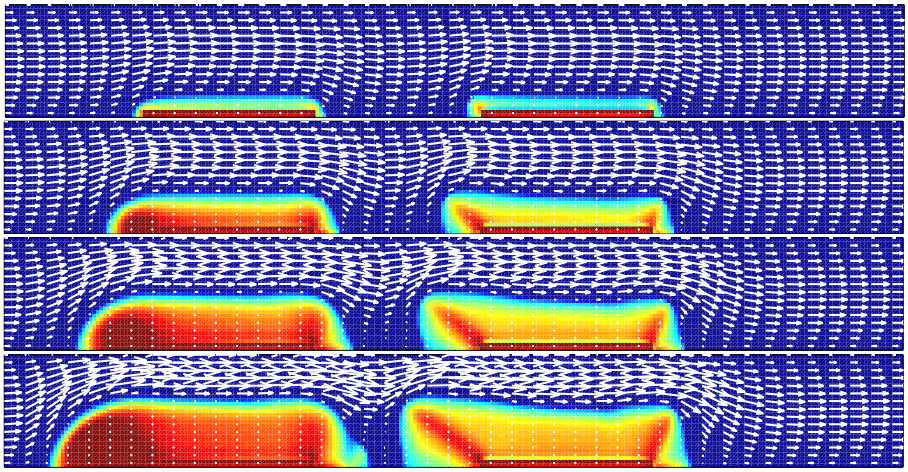

**Figure 5.1**. Time sequence of two growing thrombi, at times 300, 600, 900 and 1200 seconds (from top to bottom). The initial TF density is 15 fmol/cm$^2$, the wall shear rate is 500 s$^{-1}$, and the platelet profile is $P_1$. The arrows show the fluid velocity and have a uniform scaling throughout the sequence. Bound platelet concentrations vary from 0 (dark blue) to $P_{max}$ (dark red).

$k_{coh}P^{max}$ as in Figure 4.4, we hypothesize that this is a similar phenomenon. Rather that increasing $k_{coh}P^{max}$ in the cohesion term $k_{coh}g(\eta)P_{max}P^{m,a}$, we consider that platelets are being activated as they move over or through the upstream thrombus. This increases $P^{m,a}$ downstream, and increases the magnitude of the cohesion term. This idea seems plausible, and we can see in Figure 5.2, that there are indeed high-density 'pockets' of activated platelets directly in front of the downstream thrombus. However, if our theory is correct, this should make the entire front edge of the downstream thrombus highly dense, not just the diagonally-radiating dense regions. *Why aren't the activated platelets in front of the downstream thrombus attaching?*

To answer this question, we take a closer look at the flow between the two thrombi. Although the flow appears to be almost stagnant between the thrombi in Figure 5.1, the streamlines of the flow show exactly how that slow flow is moving. Figure 5.3 shows the streamlines of the flow plotted over the spatial concentration of mobile activated platelets, $P^{m,a}$, (left) and the spatial plot of the function $g(\eta)$ (right) positioned at the front edge of the upstream thrombus (top) and the downstream thrombus (bottom) after 10 minutes of clotting activity. The spatial region where $P^{m,a}$and $g(\eta)$ overlap indicates where the platelets should attach. There are small regions at both the front edge of both thrombi where there is little overlap of $P^{m,a}$and $g(\eta)$, but the streamlines reveal that the flow is

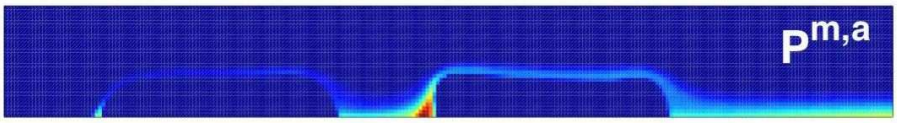


**Figure 5.2**. Spatial concentration of mobile activated platelets, $P^{m,a}$, after 600 seconds of clotting activity. The initial TF density is 15 fmol/cm$^2$, the wall shear rate is 500 s$^{-1}$, and the platelet profile is $P_1$.

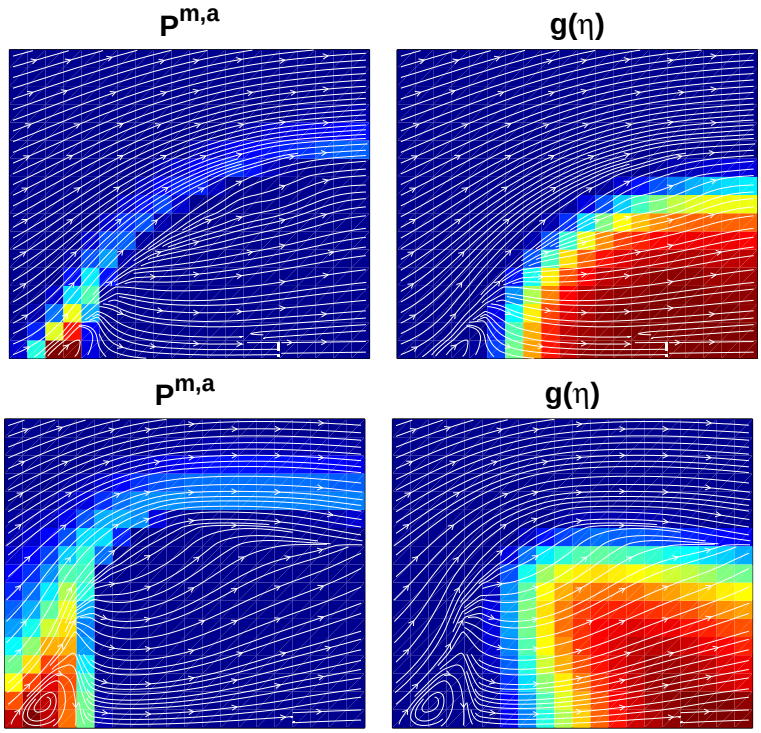


**Figure 5.3**. Streamlines of the flow plotted over the spatial concentration of mobile activated platelets, $P^{m,a}$, (left) and the function $g(\eta)$ (right) positioned at the front edge of the upstream thrombus (top) and the downstream thrombus (bottom) after 10 minutes of clotting activity.

different in the two cases.

Just upstream of both thrombi, there is a recirculation zone, but the one in front of the downstream thrombus is much larger. This difference in the size of the recirculation zone is what differentiates between the growth behaviors of the two thrombi. The larger recirculation zone causes mobile platelet to enter into or attach onto the thrombus at a greater height, which creates an uneven distribution of bound platelets in the $y$ direction. The distribution of bound platelets in the upstream clot is more uniform and this difference

is even more pronounced after 20 minutes as seen in Figure 5.4. The downstream part of a recirculation zone at the downtream edge of the upstream clot is also apparent in Figure 5.4. It is this recirculation zone that is responsible for the 'tail' that forms at the back edge of the upstream clot. However, without the downstream clot growth to create a lid driven cavity-type flow between the two thrombi, this recirculation zone does not grow large enough to create this thrombus extension.

There are other ways in which the downstream clot is affected by the upstream clot. For instance, the fluid-phase species that are carried by flow and diffusion from the upstream injury and introduced to the downstream injury are most likely in an activated state, rather that in their unactivated zymogen form. Although the upstream clot creates a barrier to platelet transport to the downstream thrombus, it also becomes a large source of activated procoagulant proteins to that same thrombus. This is the reason that the downstream thrombus grows to a size comparable to that of the upstream one. However, after reviewing the spatial-temporal concentrations of all chemical and platelet species, we conclude that the advective transport of mobile platelets has the largest impact on the

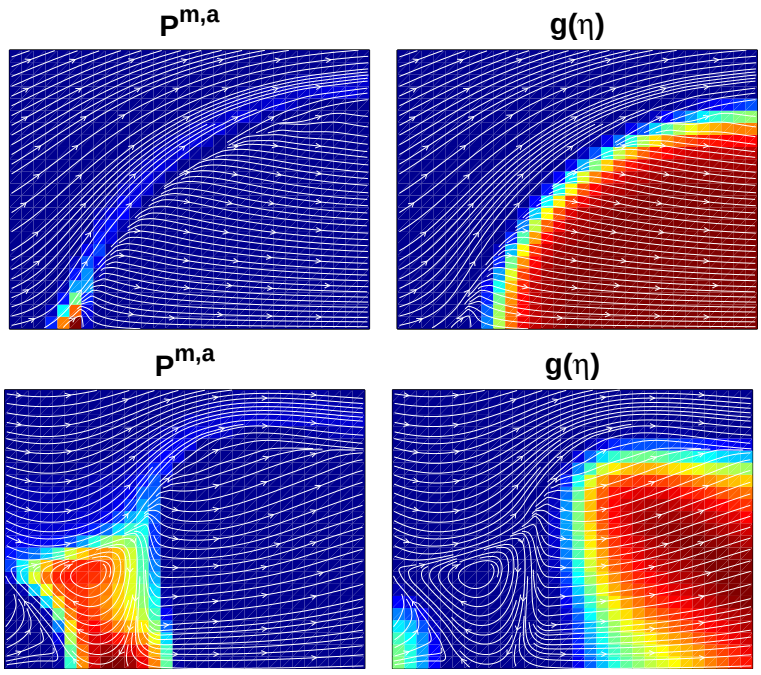


**Figure 5.4**. Streamlines of the flow plotted over the spatial concentration of mobile activated platelets, $P^{m,a}$, (left) and the function $g(\eta)$ (right) positioned at the front edge of the upstream thrombus (top) and the downstream thrombus (bottom) after 20 minutes of clotting activity.

formation of the internal structure of the downstream clot.

## 5.2 Activated Protein C and the Endothelium

Normal healthy endothelial cells that line the blood vessels provide an anticoagulant surface to the flowing blood and thus play an important role in hemostasis. One antithrombotic mechanism that they provide is the promotion of activity of the protein C pathway [66]. Endothelial cells express the membrane-bound protein thrombomodulin which functions as a co-factor (for thrombin) to activate the plasma protein C. Thrombomodulin acts as a scavenger for thrombin that may have been released from an active thrombus. In addition, the activated form of protein C (APC), if formed within close proximity to the injury, inhibits coagulation by inactivating clotting factors Va and VIIIa (FVa and FVIIIa).

The model described in Chapter 2, the 'LF' model, is set up to include inactivation of platelet-bound FVa and FVIIIa by APC. The inactivation occurs due to the formation of a complex with APC on the platelet surface. The concentration of APC is set to zero in all of the simulations that are described in the results in Chapter 3 because APC was not generated in that version of the model. Here we describe the addition of an endothelial cell covered surface to the model and the addition of the protein C pathway reactions on that surface. Following the approach of Fogelson and Tania (2005), we model an endothelial surface and the protein C pathway and add this into the LF model in order to better understand how APC inhibition in a spatial model affects thrombus growth.

### 5.2.1 Model Extension

The new species we introduce are protein C, thrombomodulin, the thrombomodulin-thrombin complex, and the thrombomodulin-thrombin-protein C complex together with their concentrations $[PC]$, $[TM]$, $[TM : E_2]$, and $[TM : E_2 : PC]$, respectively. We assume that the protein C concentration, $[PC]$, stays at a constant 65 nM throughout time and that the thrombomodulin density, $[TM] = 70$ fmol/cm$^2$, is distributed uniformly along the part of the boundary that is designated as endothelium but not along the subendothelium (see Figure 5.5). Since we regard $[PC]$ and $[TM]$ as fixed, we do not have evolution equations for them. To track the concentrations of the two endothelium-bound complexes, $[TM : E_2]$, and $[TM : E_2 : PC]$, we use the following ordinary differential equations:

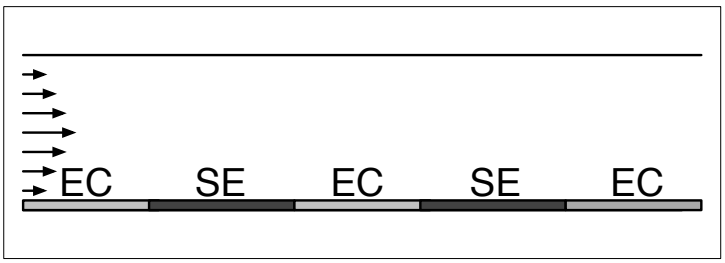


**Figure 5.5**. Spatial distribution of endothelium (EC) and subendothelium (SE). Total length of the vessel segment is 240 microns and the two SE segments are approximately 90 microns in length with 90 microns of EC in between.

$$\begin{aligned}\frac{\partial[TM:E_2]}{\partial t} &= k_{tm}^{on}e_2([TM]-[TM:E_2]-[TM:E_2:PC])-k_{tm}^{off}[TM:E_2] \\ &\quad -k_{pc}^{+}[TM:E_2][PC]+(k_{pc}^{-}+k_{pc}^{cat})[TM:E_2:PC], \qquad (5.1)\end{aligned}$$

$$\frac{\partial[TM:E_2:PC]}{\partial t} = k_{pc}^{+}[TM:E_2][PC]-(k_{pc}^{-}+k_{pc}^{cat})[TM:E_2:PC]. \qquad (5.2)$$

The first two terms in Equation 5.1 describe the binding and dissociation of thrombin with thrombomodulin. The last two terms describe the the transient binding of the thrombomodulin-thrombin complex to protein C on the way to activating protein C. The same (with opposite sign) as the terms found in Equation 5.2. These equations hold at each point of the endothelium.

These new endothelium-bound complexes lead to production of APC at the endothelium and this enters the model through an endothelium-boundary condition for APC:

$$-D\frac{\partial[APC]}{\partial y} = k_{pc}^{cat}[TM:E_2:PC]. \qquad (5.3)$$

Thrombin also has an altered boundary condition to represent binding and unbinding from thrombomodulin:

$$\begin{aligned}-D\frac{\partial e_2}{\partial y} &= -k_{z_7^{se}:e_2}^{+}z_7^{se}e_2+(k_{z_7^{se}:e_2}^{-}+k_{z_7^{se}:e_2}^{\mathrm{cat}})[Z_7^{se}:E_2] \\ &\quad -k_{tm}^{on}e_2([TM]-[TM:E_2]-[TM:E_2:PC])+k_{tm}^{off}[TM:E_2]. \qquad (5.4)\end{aligned}$$

Figure 5.5 depicts the spatial distribution of endothelium and subendothelium that we use to produce the results in the rest of this chapter.

### 5.2.2 Results

Figure 5.6 shows the spatial concentration of thrombin (top) and bound activated platelets (bottom) after 10 minutes of clotting activity. These are results from simulations which include an endothelium that enables the production of activated protein C. The distribution of bound platelets in this figure is practically indistinguishable from that in Figure 5.1, in which case there was no effect of APC.

To understand why the thrombi are so similar even with the APC inhibition, we need to investigate the APC production throughout the simulation and the species that it inhibits. Figure 5.7 shows the spatial concentration of activated protein C (APC) after 200 seconds, 10 minutes and 20 minutes of clotting activity. There is a small amount of APC that has built up at the front edge of the downstream thrombus after 200 seconds, and by five minutes a more substantial amount at the front and back edge of both the upstream and downstream thrombus has developed. This means that by 200 seconds, APC activity is limited to the downstream thrombus and is weak even there.

Figure 5.8 shows the spatial concentrations of platelet-bound FVa after 20 minutes in the absence (top) and presence (bottom) of APC. There is a substantial difference in the concentrations of platelet-bound FVa around the edges of the thrombus but in both cases there is almost no platelet-bound FVa in the interior portion of the thrombus. This is because the FVa there has boundd with platelet-bound FXa to form prothrombinase complexes. The distribution of prothrombinase concentrations were almost identical after 20 minutes (not shown).

Figure 5.9 shows the spatial concentrations of platelet-bound FVIIIa after 20 minutes in the absence (top) and presence (bottom) of APC. There is a substantial difference in the concentrations of platelet-bound FVIIIa throughout much of the thrombus. However,

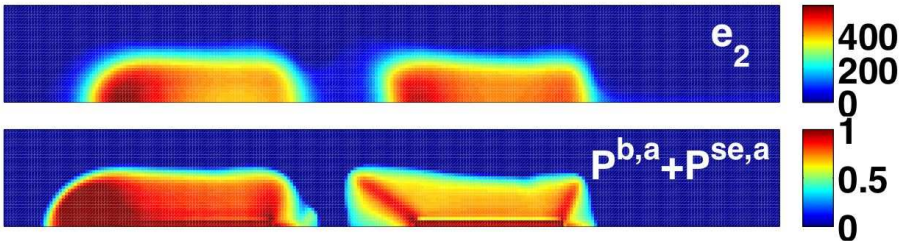


**Figure 5.6**. Spatial concentration of thrombin (top row) and bound activated platelets (bottom row) after 10 minutes of clotting activity. The initial TF density is 15 fmol/cm$^2$, the wall shear rate is 500 s$^{-1}$, and the platelet profile is $P_1$.

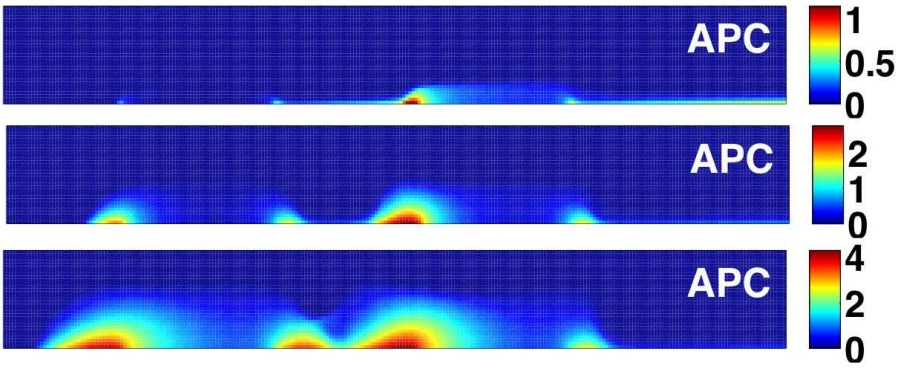


**Figure 5.7**. Spatial concentration of activated protein C after (top to bottom) 200 seconds, 10 minutes and 20 minutes of clotting activity. The initial TF density is 15 fmol/cm$^2$, the wall shear rate is 500 s$^{-1}$, and the platelet profile is $P_1$.

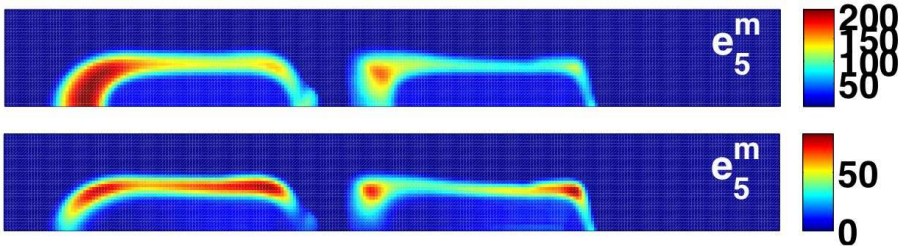


**Figure 5.8**. Spatial concentrations of platelet-bound FVa after 20 minutes of clotting activity. The top and bottom represent concentrations without and with activated protein C present, respectively. The initial TF density is 15 fmol/cm$^2$, the wall shear rate is 500 s$^{-1}$, and the platelet profile is $P_1$.

the tenase complexes, whose spatial distributions are almost identical in the presence and absence of APC (not shown), are in highest density and predominantly located on subendothelium-bound platelets since FIX is only produced at the subendothelium and is carried away by flow at the beginning of the simulations, as described in Chapter 3.

We conclude that while APC is able to inhibit platelet-bound factors Va and VIIIa, this inhibition begins and persists at times later than that during which the bulk of the tenase and prothrombinase complexes are formed. Because thrombin is required for APC production, and this thrombin must be produced and transported to regions where there is thrombomodulin attached to the endothelium, APC does not arrive on scene until it is too late. If APC was able to affect the earlier thrombin production in some way, it may play a larger role in the inhibition of thrombin production and thrombus propagation.

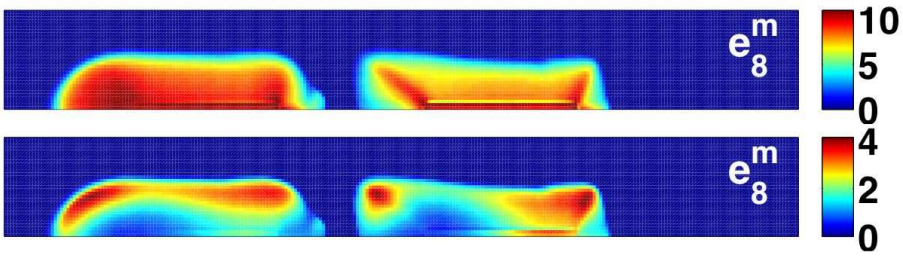


**Figure 5.9**. Spatial concentrations of platelet-bound FVIIIa after 20 minutes of clotting activity. The top and bottom represent concentrations without and with activated protein C present, respectively. The initial TF density is 15 fmol/cm$^2$, the wall shear rate is 500 s$^{-1}$, and the platelet profile is $P_1$.

### 5.2.3 Discussion

Earlier studies by Fogelson and Tania (2005) with an extended version of the KF model suggest that under flow situations, APC has little effect on events within the thrombus. There are a few assumptions that we have made here in this model extension that have simplified the realistic production and behavior of APC. For instance, protein C in this model is readily available at 65 nM, when it should be lost due to forming complexes and less available to the endothelium due to physical blockage by the thrombus itself. However, even with this abundant source of protein C, the maximum APC concentration reached about 4 nM (see Figure 5.7), which leads us to believe that our approximation for constant plasma protein C may in fact be quite reasonable. Also, as seen in many of our results within this thesis, there is growth of thrombi upstream and downstream of the subendothelium and we have not taken into consideration the physical inhibition of the endothelium that is covered by platelets that bind to the thrombus directly above those regions. Finally, we have used a thrombomodulin density that we believe to be five times that of a real endothelial cell. Further modification of the model to account for each of these details would *decrease* the amount of APC available to inhibit the platelet-bound species FVa and FVIIIa, inevitably leading to more thrombus growth. In conclusion, under the assumptions of our model, the results agree with the the previous results from Fogelson and Tania (2005) and suggest that APC has little effect on thrombus growth.

However, it has recently been suggested that the physiological role of APC is to act on the endothelial surface to limit *prothrombinase* activity, which would then prevent initiation of the amplification phase of thrombosis and thus limit propagation and thrombus growth [50]. It is thought that small amounts of thrombin produced on the endothelium act to

amplify the response by both activating platelets and the platelet-bound cofactors FV and FVIII. Our model does not currently support the formation of prothrombinase complexes on the endothelium, but it also does not rely on thrombin to be the only activator of platelet-bound FV and FVIII. Our model allows FXa (made by the TF:VIIa complex at the subendothelium) to slowly activate platelet-bound FV and FVIII and also does not include the activation of plasma FV, which would be necessary for the formation of prothrombinase complexes to form on the endothelial cells. It would be interesting to see how the results might change if we were to incorporate endothelial-cell-bound prothrombinase complexes and activation of plasma FV by plasma FXa into this new version of the model.

# CHAPTER 6

# STIRRING MODEL

In their 2004 paper [4], Allen *et al.* describe the effects of varying single procoagulant proteins on thrombin production using a cell-based model of coagulation. In an attempt to use our theoretical model to make further predictions of the behavior of this type of *in vitro* experiment, we have adapted our spatial model (the LF model) to replicate the results from this paper. The ultimate goal is to use our model to predict how thrombin production is affected when varying *multiple* procoagulant proteins with the hopes of unveiling novel, non-heparin-based anticoagulation therapies. This chapter contains a brief summary of the experiments from [4] followed by a description of our revised model and a comparison of the results.

## 6.1 Physical Experiments and Results

The cell-based model of coagulation employed in [4] was developed by Monroe *et al.* [51, 62]. In this model, human monocytes are deposited into microtiter wells and activated to induce tissue factor expression. The monocytes, used as tissue factor-bearing cells, initiate coagulation in the presence of activated factor VII. Physiological numbers of platelets and physiological concentrations of procoagulant and inhibitory proteins are added to the wells which contain the adherent monocytes. Different sets of experiments are carried out in which the number of monocytes and platelets is kept constant but the concentrations of prothrombin and factors V, VIII, IX, X, and XI are varied one at a time from 0% to 200% of normal plasma concentration (see Table 6.1). After initiating coagulation in each of these experiments, thrombin generation is measured at timed intervals. At each sample time, 10 $\mu L$ of the reaction mixture is removed from the well. Just before the reaction is sampled, the mixture is 'stirred' with a pipette, in order to obtain uniformity in results across sets of experiments (A. Wolberg, personal communication).

The cell-based model aided Allen *et al.* in the systematic examination of the effect of individual procoagulant proteins on thrombin production. They were able to highlight

**Table 6.1**. Amount or concentration of components used in the cell-based model.

| Component | Amount or Concentration |
|---|---|
| Platelets | 75,000 $\mu$L |
| Monocytes | TF $<$ 1 pM |
| Prothrombin | 1.4 $\mu$M |
| FV | 20 nM |
| FVIII | 0.3 nM |
| FIX | 70 nM |
| FX | 135 nM |
| FXI | 25 nM |
| AT | 3 $\mu$M |
| TFPI | 3 nM |

features unique to some proteins but also found some could be grouped in terms of their effects. Experimental results using the cell-based model showed that the clotting factors which contribute to the formation of the tenase complex, FVIII, FIX, and FXI (not shown), primarily affected the rate and peak of thrombin production but had little effect on the total thrombin production (see Figure 6.1).

The effect of FXI was, however, less pronounced than that of FVIII and FIX. The results also showed that clotting factors which contribute to the formation of the prothrombinase complex, prothrombin and FV (results from experiments with FV-deficient platelets), affected the rate, peak, *and* total thrombin production (Figure 6.2). However, the left

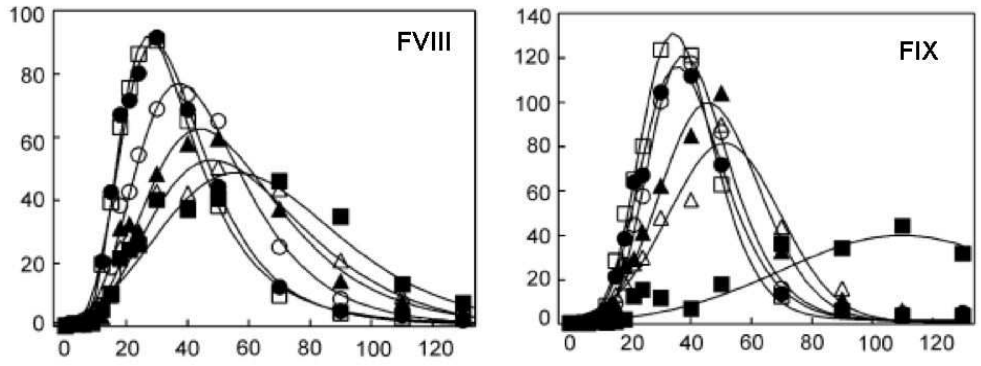


**Figure 6.1**. Figures reproduced from [4] with permission. Thrombin production (nM) versus time (minutes) as the concentrations of FVIII (top left), FIX (top right), and FXI (bottom) were varied from 0% to 200% of normal plasma concentration. Percentages are 0% (solid square), 1% (open triangle), 3% (solid triangle), 10% (open circle), 100% (solid circle), 200% (open square).

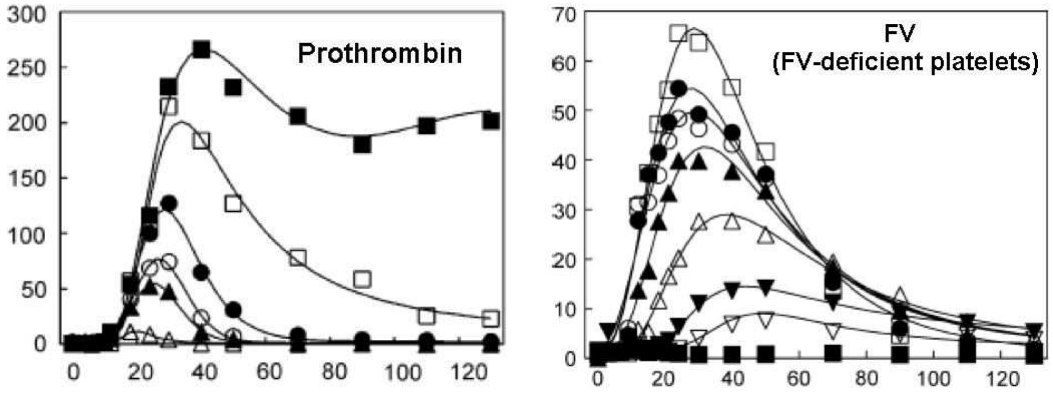


**Figure 6.2**. Figures reproduced from [4] with permission. Thrombin production (nM) versus time (minutes) as the concentrations of prothrombin (left) and FV using FV-deficient platelets (right) were varied from 0% to 200% of normal plasma concentration. Percentages for prothrombin are represented as 10% (open triangle), 50% (solid triangle), 75% (open circle), 100% (solid circle), 150% (open square) and 200% (solid square). Percentages for FV-deficient platelets are shown as 0% (solid square), 1% (open upside-down triangle), 3% (solid upside-down triangle), 10% (open triangle), 30% (solid triangle), 50% (open circle), 100% (solid circle), 200% (open square).

panel in Figure 6.3 shows that in the experiments performed with normal platelets and variations in the plasma FV concentration had minimal affect on thrombin production.

No thrombin production was observed without FX, since FX is required in formation of prothrombinase complexes. With the addition of small amounts of FX, between 1% and 10%, the thrombin production is normalized (see Figure 6.3). These data, combined with the FV data, suggest that FV proteins stored within platelets, rather than plasma FV, are the major contributor to the prothrombinase complexes formed on platelet surfaces.

Although the details of the experimental protocols of [4] are not represented in their entirety in this thesis, we believe that the results from our mathematical model should at least match the qualitative behaviors that we have highlighted so far.

## 6.2 Mathematical Model

Our first idea for modeling this system was to use an extension of the ODE model of Kuharsky and Fogelson [38]. In such a model, we would use a specified concentration of platelets, and thus platelet binding sites, to represent that of the entire well described above. The platelet concentration, although relatively low in these experiments (see Table 6.1), does not affect the density of binding sites on each platelet surface. Platelets are discrete objects and so their binding sites, which are exposed in high densities, are only

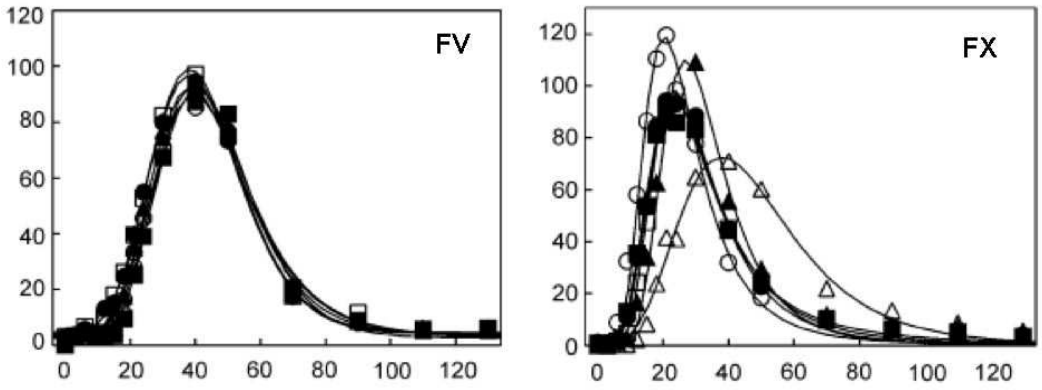


**Figure 6.3**. Figures reproduced from [4] with permission. Thrombin production (nM) versus time (minutes) as the concentrations of FV and FX are varied from 0% to 200% of normal plasma concentration. Percentages for FV are indistinguishable, but the percentages for FX are 1% (open triangle), 3% (solid diamond), 10% (solid triangle), 50% (solid circle), 100% (solid circle), 150% (open square), and 200% (solid square).

positioned at discrete locations. To correctly represent this, we must model platelet binding sites in high densities at discrete locations and therefore need a *partial* differential equation to include the spatial component. To be sure that these discrete locations of high-density binding sites are necessary, we first simulated clotting activity in a small square domain including diffusive transport together with no-flux boundary conditions so that no species could leave the domain. We did not include flow and therefore the model had a finite amount of each procoagulant protein. We used a constant platelet concentration and represented a tissue factor-bearing subendothelium along the bottom boundary. After 20, 40 and even 60 minutes of clotting activity there was less than 1 nM of thrombin produced. We were not able to see significant thrombin production unless the platelet concentration was increased to well above a physiological level. We therefore proceeded to adapt the LF model for this set up, with the addition of high-density regions of binding sites.

The microtiter wells used in the experiments comfortably hold 300 $\mu L$ of liquid (A. Wolberg, personal communication). For simplicity, and because platelets are neutrally buoyant, we assume platelets are uniformly distributed within a well. Theoretically, this means we can split a well into smaller, equal-sized compartments, each of which contains one *fixed* platelet (we assume these are of the type $P^{b,a}$). Tracking the concentrations and activity in one of these smaller compartments with no-flux boundary conditions is our approximation to tracking the dynamics within the entire well. Assuming platelets are approximately 3 $\mu m$ in diameter and using a concentration of 75,000/$\mu$L in a 300 $\mu L$

well, as in the experiments, we calculate the smaller compartments to have a volume of approximately 24 $\mu m^3$ which corresponds to a distance of 24 $\mu m$ between platelet centers. The next consideration is how to represent this 'volume' in two dimensions, which is necessary since that is how our model is set up. The simplest approach would be to compute on a 24 $\mu m$ x 24 $\mu m$ square domain with a 'thickness' of 24 $\mu m$ (see the left schematic in Figure 6.4). However, if we were to use a two-dimensional domain to approximate this cubic domain, we would actually be modeling a cylinder of platelets throughout the 24 $\mu m$ thickness, which overestimates the number of platelets that should reside in one compartment.Therefore, we use the compartment as shown on the right side of Figure 6.4.

Another modification to the LF model is the addition of a layer of monocytes at the bottom of a well. The monocytes used in the experiments were cultured to induce tissue factor expression, so our assumption about tissue factor activity on the boundary still holds. A new and interesting feature of monocytes, however, is their ability to produce thrombin on their surfaces by binding both factors Va and Xa which together form the prothrombinase complex [69, 5]. To include this in the current model, we add new 'subendothelium-bound' species. We assign a specific number of binding sites for factor Va at the monocyte surface and allow fluid-phase factor Va to bind to them. Fluid-phase factor Xa is assumed to bind directly to these monocyte-bound factor Va molecules, immediately forming active prothrombinase complexes on the cell surfaces. These active complexes bind fluid-phase prothrombin molecules, activate them into thrombin which is then released back into the fluid.

This specific prothrombinase activity occurs only at the bottom of the well where there are monocytes. Therefore we cannot simply represent the events of the entire well within one compartment; we must use multiple, separate compartments. One should represent the space nearest the monocytes, include a platelet and a small portion of monocyte surface while any other(s), representing the space away from the bottom of the well, should contain platelets but no monocytes.

The sampling in the experiments starts off at two minute intervals. During these two minutes, the fluid-phase reactants are also undergoing diffusion. The compartment nearest the monocytes must therefore be large enough to allow an enzyme made at the bottom of the well, like thrombin, to diffuse upward without being hindered in those two minutes. Using the diffusion coefficient of $5 \times 10^{-7}$ cm$^2$/s, we calculate the diffusion length, $L_D$, in two minutes using the following:

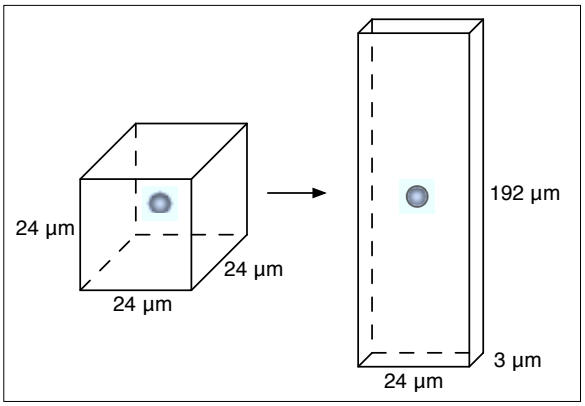


**Figure 6.4**. A schematic of one single compartment that holds one platelet. Approximating the cubic domain (left) in two dimensions would lead to a cylinder of eight platelets, thus, we use the rectangular domain (right) to avoid including more than one platelet in one compartment.

$$L_D = \sqrt{4Dt} = \sqrt{20 \times 10^{-7} cm^2/s \times 120s} \approx 155 \mu m. \tag{6.1}$$

Instead of using the square with dimensions 24 x 24 $\mu m$ and 'thickness' of 24 $\mu m$, we use a rectangular domain that is 24 x 192 $\mu m$ with a 'thickness' of 3 $\mu m$ to represent the volume of a single compartment (see Figure 6.4). We use a height of 192 $\mu m$, which is a slight increase from $L_D$, but it makes the domain's height an even eight times the width.

We will compute within the compartments just described, but it is actually the sum of these compartments, which we denote as 'regions', that will represent the entire well. We use three separate regions, $R_1, R_2$, and $R_3$ in which there will be separate and different activity, see Fig. 6.5. All of the monocyte activity will occur in $R_1$, the region nearest the bottom of the well. Contained within $R_1$ there are on the order of 390,000 compartments, as described above and seen in Figure 6.4, which sum to a volume of $V_1 = \pi(3 \times 10^3 \mu m)^2 \times 192 \mu m$. Each compartment includes a single platelet and therefore, each region contains as many platelets as it has compartments.

The initial volume of the well is 300 $\mu L$ and we let the total volume of the three regions $V_1 + V_2 + V_3 = 300 \mu L$ to start. We assume that the volume $V_2$ of region $R_2$ is initially zero but represents a region that 'exchanges' platelets and thus platelet bound proteins, with $R_1$. The region $R_3$ includes the pool of platelets that have not made it to $R_1$ or $R_2$ in order to exchange, but has mixed its fluid-phase proteins with the entire well. After each stir-and-sample, $R_2$ will grow in volume by the volume of $R_1$ and whatever was in $R_2$ previously will mix evenly with what is in the newly added volume.

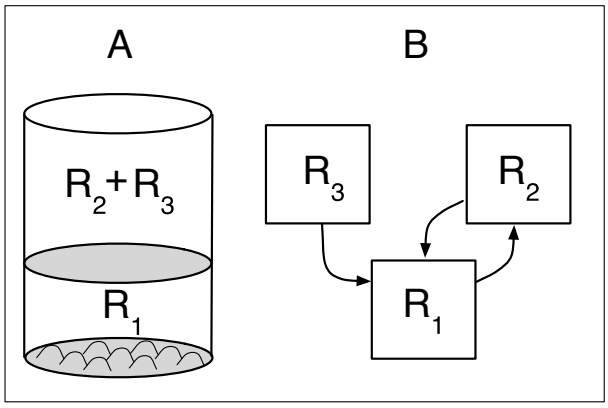


**Figure 6.5**. A schematic of the splitting of the wells (A) and a diagram of the platelet "exchanges" that take place between the separate regions (B).

### 6.2.1 Algorithm

We begin the simulation with specified amounts of platelets, clotting factors and inhibitors (see Table 6.1) spread evenly throughout the mixture in $R_1$ and $R_3$. After set amounts of time that match with the experiments, we 'stir' the current mixture and remove 10 $\mu L$ from the total volume. The following is the algorithm we use to 'stir' the mixture:

1. Take the following steps for the fluid-phase species:

   (a) Average the concentration of each fluid-phase species, in $R_1$, $R_2$, and $R_3$.

   (b) Weight these averages appropriately using the current volumes of each region to compute an entire-well average.

   (c) Update all fluid-phase species to this average concentration everywhere.

2. Take the following steps for the platelet-bound species:

   (a) The small platelet population in $R_1$ mixes with that in $R_2$.

   (b) Platelet-bound species in $R_1$ and $R_2$ are averaged.

   (c) The volume of $R_2$ is increased by the volume of $R_1$. (The volume of $R_1$ remains the same.)

   (d) The concentrations in $R_2$ are updated to be the average calculated in step 2.

   (e) Concentrations of platelet-bound species in $R_1$ are set to those of the platelet-bound species in $R_3$.

(f) Platelet-bound species in $R_3$ remain unchanged in this 'stirring' step, but are affected later by the new fluid-phase species' concentrations.

(g) 10 $\mu L$ of the mixture is removed (from $R_2$ and $R_3$ only), weighted by the appropriate volumes in $R_2$ and $R_3$.

### 6.2.2 Equations and Parameters

To account for the formation and activity of prothrombinase complexes at the monocyte surface, we add four new species to the current model: monocyte-bound factor Va, $E_5^{se}$, the complex of monocyte-bound factor Va and fluid-phase Xa, $E_5^{se}$:$E_{10}$, fluid-phase prothrombin bound to this complex, $Z_2$:$E_5^{se}$:$E_{10}$ and finally, we allow clotting factor V to become activated in plasma by factor Xa, and so have the new fluid-phase complex, $Z_5$:$E_{10}$. This is to have fluid-phase FVa available to bind the monocyte surface.

The differential equation that describes changes to $Z_5 : E_{10}$ is as follows:

$$\begin{aligned} \frac{\partial [Z_5 : E_{10}]}{\partial t} &= \nabla \cdot (D \nabla [Z_5 : E_{10}]) \\ &\quad + k^+_{z_5:e_{10}} z_5 e_{10} - (k^-_{z_5:e_{10}} + k^{cat}_{z_5:e_{10}})[Z_5 : E_{10}], \end{aligned} \tag{6.2}$$

where the term on the first line is the diffusive transport term, and the terms on the second line are the activation terms, accounting for the binding, dissociation and catalyzation. Another change in the model due to this new species is the addition of $-k^+_{z_5:e_{10}} z_5 e_{10} + k^-_{z_5:e_{10}}[Z_5 : E_{10}]$ to the right hand side of the differential equation for fluid-phase factor V. The terms $(k^-_{z_5:e_{10}} + k^{cat}_{z_5:e_{10}})[Z_5 : E_{10}] - k^+_{z_5:e_{10}} z_5 e_{10}$ and $k^{cat}_{z_5:e10}[Z_5 : E_{10}]$ are also added to the right hand sides of the differential equations for fluid-phase Xa and Va, respectively.

We assume there are 16,000 binding sites available for factor Va per monocyte [69], which translates into an initial surface density of 0.16 fmol/cm$^2$, which we denote $M_5$. Mathematically, we represent factor Va binding to monocytes in a way similar to the way that VIIa binds to tissue factor in the subendothelium. The equation that tracks the concentration of monocyte-bound factor Va, $e_5^{se}$, is

$$\begin{aligned} \frac{\partial e_5^{se}}{\partial t} &= k_5^{on,se} e_5 (M_5 - e_5^{se} - [E_5^{se} : E_{10}] - [Z_2 : E_5^{se} : E_{10}]) - k_5^{off,se} e_5^{se} \\ &\quad - k_{10}^{on,se} e_5^{se} e_{10} + k_{10}^{off,se} [E_5^{se} : E_{10}], \end{aligned} \tag{6.3}$$

where the first two terms represent the binding and unbinding from the monocyte surface, and the last two terms are the rates of formation and dissociation of the monocyte-bound prothrombinase complex. We track this complex with the following equation:

$$\begin{aligned}\frac{\partial[E_5^{se}:E_{10}]}{\partial t} &= k_{10}^{on,se}e_5^{se}e_{10} - k_{10}^{off,se}[E_5^{se}:E_{10}] \\ &+ (k^-_{z_2:e_5^{se}:e_{10}} + k^{cat}_{z_2:e_5^{se}:e_{10}})[Z_2:E_5^{se}:E_{10}], \\ &- k^+_{z_2:e_5^{se}:e_{10}}z_2[E_5^{se}:E_{10}]\end{aligned} \tag{6.4}$$

where the first two terms are the same as in the last equation and the next three terms represent the activation of fluid-phase prothrombin into thrombin. And finally, we have the equation

$$\begin{aligned}\frac{\partial[Z_2:E_5^{se}:E_{10}]}{\partial t} &= k^+_{z_2:e_5^{se}:e_{10}}z_2[E_5^{se}:E_{10}], \\ &- (k^-_{z_2:e_5^{se}:e_{10}} + k^{cat}_{z_2:e_5^{se}:e_{10}})[Z_2:E_5^{se}:E_{10}],\end{aligned}$$

on the surface of the monocytes. This reaction also leads to a new boundary condition for fluid-phase $z_2$:

$$-D\frac{\partial z_2}{\partial y} = -k^+_{z_2:e_5^{se}:e_{10}}z_2[E_5^{se}:E_{10}] + k^-_{z_2:e_5^{se}:e_{10}}[Z_2:E_5^{se}:E_{10}]. \tag{6.5}$$

and modification of the boundary condition for fluid-phase $e_2$:

$$\begin{aligned}-D\frac{\partial e_2}{\partial y} &= -k^+_{z_7^{se}:e_2}z_7^{se}e_2 + (k^-_{z_7^{se}:e_2} + k^{\rm cat}_{z_7^{se}:e_2})[Z_7^{se}:E_2] \\ &+ k^{cat}_{z_2:e_5^{se}:e_{10}}[Z_2:E_5^{se}:E_{10}].\end{aligned}$$

Finally, the boundary conditions for fluid-phase Xa is changed to reflect the reactions in Equation 6.3:

$$\begin{aligned}-D\frac{\partial e_{10}}{\partial y} &= -k^+_{z_7^{se}:e_{10}}e_{10}z_7^{se} + k^{\rm cat}_{z_{10}:e_7^{se}}[Z_{10}:E_7^{se}] \\ &+(k^-_{z_7^{se}:e_{10}} + k^{\rm cat}_{z_7^{se}:e_{10}})[Z_7^{se}:E_{10}] \\ &- k_{10}^{on,se}e_5^{se}e_{10} + k_{10}^{off,se}[E_5^{se}:E_{10}].\end{aligned} \tag{6.6}$$

In the LF model, we accounted for the antithrombin (AT) inhibition of plasma factors IXa, Xa and thrombin with a simple, first-order rate constant. This was done because of the assumption that the AT was found in relatively high concentrations in the blood and since

there was flow, there was a constant supply. In this current version of the model, however, there are finite amounts of procoagulant proteins and inhibitors in the wells. Therefore, we include AT as a variable, whose concentration, and thus the rate at which it inhibits, decreases as it quickly forms complexes with IXa, Xa and thrombin. We also assume that any complex of AT with thrombin, factor IXa, or Factor Xa, is formed irreversibly and we use the second-order rate constants $4.9 \times 10^2$, $3.13 \times 10^3$, and $7.08 \times 10^3 M^{-1}s^{-1}$ for factors IXa, Xa and thrombin, respectively. These rates were acquired from experiments done on AT binding in the absence of heparin [35].

Finally, the last model consideration is the inclusion of factor V-deficient platelets versus platelets that release stores of factor V. In the LF model, we include the term, $N_5 \frac{\partial(P^{b,a}+P^{se,a})}{\partial t}$ in the evolution equation for fluid-phase factor V; it gives the rate of appearance of FV due to its release by platelets when they become bound and activated. In the current version of the model, we initialize the simulation with bound platelets that are *already* activated, and thus this term will not affect plasma levels of factor V. To include platelets with and without stores, we assume that either the initial platelet-bound factor V concentration is at 80% of its maximum or is zero.

## 6.3 Comparing Model to Experiment

Although there are a few obvious quantitative differences in our model's results compared to those from the experiments, such as peak thrombin level, our model does quite well qualitatively at replicating the behaviors unique to individual proteins. Allen *et al.* characterize the pattern of thrombin generation by the rate of the thrombin burst, the peak thrombin level and by the area under the thrombin level curve (AUC), which they use to reflect both the amount and persistence of free thrombin. They cannot measure the total thrombin produced, but we can with our model. To approximate the total number of thrombin molecules produced throughout the simulation, we integrate the $k^{\text{cat}}_{z_2^m:pro}[Z_2^m{:}PRO]$ term over time.

In Figure 6.6, we show the plasma-phase thrombin concentration during 90 minutes of clotting activity, for 100%, 1%, and 0.1% of normal plasma concentrations of factors VIII and IX. We note here that 0.1% is lower than any nonzero percent used in the experiments. Decreasing the concentrations of proteins successively, in our model, qualitatively affects the thrombin level curve in the same way as in the experiments, but we are able to see these effects more distinctly when we decrease to 0.1%. In all figures, the thrombin concentration

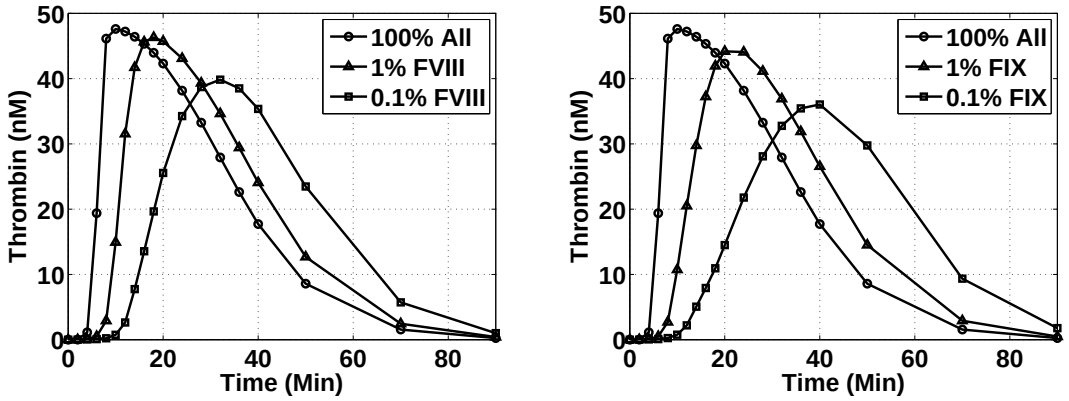


**Figure 6.6**. Plasma-phase thrombin concentration (nM) versus time (minutes) with varied concentrations of plasma factors VIII (left) and IX (right).

plotted is the entire-well volume-weighted average of fluid-phase thrombin that is calculated in algorithm step 1(b) described in Section 6.2.1.

In each of the plots in Figure 6.6, the line through open circles is the same and represents the 'baseline' case where all of the added procoagulant protein concentrations are 100% of normal. The curves show that the rate of thrombin production is slowed and the peak of thrombin production is decreased when the amount of added factors VIII and IX are decreased from 100% to 1% to 0.1%. The curves for 1% and 0.1% in the left and right panels show that the rate is slower and the peak is slightly decreased in the right panel (FIX) compared with those in the left panel (FVIII). Table 6.2 lists both the area under all of the curves seen in Figure 6.6 and the total thrombin production. In the cases where

**Table 6.2**. Area under the thrombin concentration curve and total thrombin produced for variations in concentration of plasma factors VIII and IX.

| **Variation** | **Area Under the Curve (nM$\times 10^3$·min)** | **Total Thrombin Produced (Molecules) $\times 10^{13}$** |
|---|---|---|
| 100% All | 4.49 | 1.76 |
| 1% FVIII | 4.50 | 1.76 |
| 0.1% FVIII | 4.48 | 1.42 |
| No FVIII | 0.079 | 0.017 |
| 1% FIX | 4.50 | 1.57 |
| 0.1% FIX | 4.49 | 1.34 |
| No FIX | 0.082 | 0.018 |

factors VIII and IX are at 0.1 and 1 % of normal, we can see that the area under the curve and the total thrombin production are relatively unaffected. These data are in good agreement (qualitatively) from [4] and those shown in Figure 6.1, and show that the procoagulant proteins contributing to the formation of tenase primarily affect the rate and peak of thrombin generation and do not seem to affect the total amount of thrombin produced. However, when we completely remove factors VIII and IX from the well, we see a significant decrease is thrombin production. This does not agree with the conclusions from [4], but there is one set of experiments (not shown here) in which the area under the curve appears to be significantly lower when no FVIII or FIX are present. Currently, we do not include factor XI in our model and thus cannot compare results of varying amounts of this protein.

In Figure 6.7, we show the results for varying the amounts of prothrombin and factor V, a protein that contributes to the formation of the prothrombinase complex. Again, the line through open circles represent the 'baseline' case where all of the added procoagulant protein concentrations are 100% of normal.

Our model shows that the total amount of thrombin produced is significantly different when varying levels of prothrombin and factor V, which was not the case when varying factors VIII and IX as described above. It is clear from Table 6.3 that increasing the concentration of plasma prothrombin increases the total production of thrombin and decreasing the concentration of plasma prothrombin decreases the total thrombin production. Furthermore, varying prothrombin levels affects the other two measures of thrombin pro-

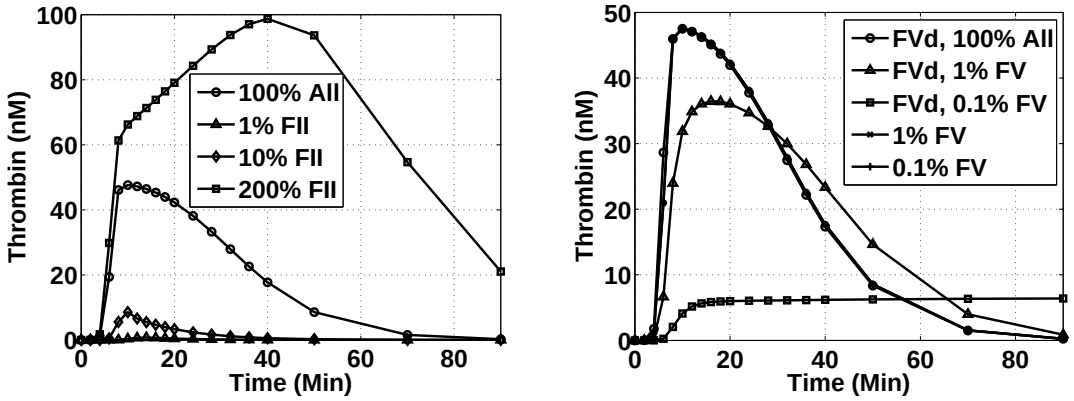


**Figure 6.7**. Plasma-phase thrombin concentration (nM) versus time (minutes) with varied concentrations of plasma prothrombin (left) and plasma factor V (right).

**Table 6.3**. Area under the thrombin concentration curve and total thrombin produced for variations in concentration of prothrombin and plasma factor V.

| **Variation** | **Area Under the Curve (nM$\times 10^3$·min)** | **Total Thrombin Produced (Molecules) $\times 10^{13}$** |
|---|---|---|
| 100% All | 4.49 | 1.76 |
| 200% FII | 18.00 | 3.26 |
| 10% FII | 0.34 | 0.18 |
| 1% FII | 0.03 | 0.02 |
| 100% All FV-deficient | 4.49 | 1.76 |
| 1% FV, FV-deficient | 4.46 | 1.63 |
| 0.1% FV, FV-deficient | 1.50 | 0.54 |
| 1% FV | 4.49 | 1.76 |
| 0.1% FV | 4.49 | 1.76 |

duction as well: rate and peak as seen in Figure 6.7. This is in good agreement with the experimental results in Figure 6.2. Similarly, the curves in the right panel show that varying the concentration of plasma factor V in a reaction mixture that includes factor V-deficient platelets also affects the rate of thrombin production and thepeak thrombin level. Interestingly, the top curve in the right panel of Figure 6.7 is actually three curves, all of which match the 'baseline' curve. One curve represents thrombin production when we use normal concentrations of all procoagulant proteins and the factor-V deficient platelets. The other two curves represent thrombin production where the added amount of factor V is 1% and 0.1% but the platelets have their normal platelet stores of factor V. The thrombin levels are similar because the prothombinase concentration curves (in time) are almost identical after eight minutes and, at this same time, the $P_5$ binding sites become nearly saturated in each of the three cases. These three indistinguishable curves demonstrate that platelet stores of factor V, rather than added plasma factor V, act as the main source of V in the formation of prothrombinase complexes. Again, our model results agree very well (qualitatively) with those from experiments shown in Figures 6.2 and 6.3.

Finally, we compare the differences in varying the concentration of plasma factor X in Figure 6.8. The main comments about the variation in factor X levels from [4] were i) no thrombin was produced with no added plasma factor X, ii) with a small amount of plasma factor X, thrombin levels were normalized, and iii) above 10% of normal concentration of plasma factor X, all rates of thrombin production were the same. In our model, we cannot produce thrombin without prothrombinase and thus factor X. Figure 6.8 shows that with

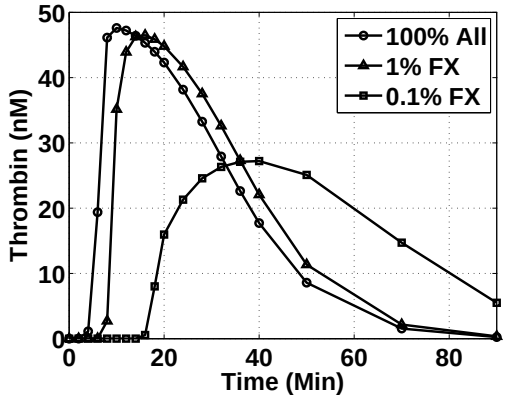


**Figure 6.8**. Plasma-phase thrombin concentration (nM) versus time (minutes) with varied concentrations of plasma factor X.

a concentration of 0.1% of factor X, the thrombin level is

significant, although delayed. Furthermore, the rate of thrombin production with a 1% plasma factor X concentration is almost identical to the rate with a concentration of 100%. In these three cases, 0.1%, 1%, and 100%, the $P_5$ binding sites (receptors for plasma factors V and Va) saturate early on, which indicates that there are platelet-bound factor V molecules readily available to bind with factor Xa. Comparing the 0.1% and 1% cases, in the simulation using 0.1% of the normal plasma factor X concentration, more IXa is produced at the monocyte surface due to the lower level of factor X. This leads to a higher concentration of tenase complexes, albeit at a later time. The small number of factor X molecules become activated at a relatively fast rate due to the larger concentration of tenase. The platelet-bound Xa may then bind to and activate platelet-bound factor V which results in the formation of prothrombinase complexes and leads to the thrombin production. The data seen in Figure 6.8 and Table 6.4 are in good agreement with those from the experiments.

## 6.4 Discussion

We have adapted the LF model to model clotting activity within a microtiter well that includes diffusion but no flow, and thus finite amounts of procoagulant proteins. The major adaptations to the LF model include the 'stirring' algorithm and the monocyte-surface prothrombinase activity. Our model produced results that are in excellent qualitative agreement with experimental results described in [4]. We show that proteins that contribute to tenase, factors VIII and IX, affect the rate and maximum thrombin production but do

**Table 6.4**. Area under the thrombin concentration curve and total thrombin produced for variations in concentration of plasma factor X.

| **Variation** | **Area Under the Curve (nM$\times 10^3 \cdot$min)** | **Total Thrombin Produced (Molecules) $\times 10^{13}$** |
|---|---|---|
| 100% All | 4.49 | 1.76 |
| 1% FX | 4.51 | 1.64 |
| 0.1% FX | 4.13 | 1.24 |

not seem to affect the total amount of thrombin produced. We also show that prothrombin and factor V (when in combination with factor-V deficient platelets) levels affect all three measures of rate, peak and total amount of thrombin productions. And finally we showed that a small amount of added factor X produced a large amount of thrombin and that the rate of thrombin production was the same once the added amount of X was increased above a specific level.

There are a few obvious quantitative differences in our model's results compared to the experimental results. Our model produced a maximum value for the thrombin peak that was much lower than those in the experiments and we also had to lower the percentage of added procoagulant protein concentrations to 0.1% in order to achieve similar qualitative behavior to the experimental results.

There are ways in which we can modify the model to increase or decrease the thrombin peak value. For instance, thrombin and prothrombin share binding sites in this model and if we increase the off-rate for thrombin from its platelet binding site, we make more room for prothrombin and thus more thrombin production. In fact, in the current version of the model, we have increased this off-rate eight-fold from the LF model due to recent findings in the literature stating that thrombin unbinds from its binding site on platelets upon activation [36]. This increased the thrombin peak from approximately 30 nM (using the off-rate from the LF model) to around 48 nM. Another way in which we can modify the thrombin production is by altering the number of binding sites for specific proteins. For instance, we have recently discovered that there may be as many as 16,000 shared binding sites for prothrombin (not thrombin) and factor X on platelet surfaces [65]. Compared to the 2700 we have now for factors X/Xa and 2000 for prothrombin/thrombin, this might allow more binding of prothrombin and factor X to the platelet surfaces. However, the prothrombinase complex formation may still be limited by the number of factor V binding

sites. We have not tried this modification yet, but it will be interesting to see how the results are affected by these types of changes.

We also see that the rate of thrombin production is slower and the peak is decreased more when varying levels of factor IX compared to varying levels of factor VIII. This is opposite of what is seen in the experimental results. However, upon activation by thrombin, factor XI is a known activator of factor IX. It is possible that our results reflect the lack of factor XI in the model. The kinetics of factor XI activity on platelet surfaces is not clear from the literature, but we are currently working on different possible ways in which to add factor XI into the system.

# CHAPTER 7

# NUMERICAL METHODS

We solve the model equations in a rectangular spatial region $R = [0, x_{max}] \times [0, y_{max}]$. For all of the variables, including the fluid, we use a uniform mesh placed over $R$ with equal mesh spacing in both the $x$ and $y$ directions. For each differential equation, we use a finite-difference approximation defined at points on this mesh. We use a variable time step set to three-fourths of the Courant number, which is necessary for numerical stability of the advection scheme. However, this poses quite serious timestep-size restrictions when solving the diffusion and reaction equations, which do not physically or numerically require such a restriction. To reduce the computation time, we use two different sized timesteps. The smaller one, $\Delta t$ is dependent upon the Courant number and a larger one, $\Delta t_{rxn}$ is set to be approximately one millisecond which is sufficiently small to capture accurately the behavior of the reaction system. They are related in the following way:

$$\Delta t = \frac{\Delta t_{rxn}}{M}, \tag{7.1}$$

$$M = \text{ceil}\left(\frac{u_{max}\Delta t_{rxn}}{\frac{3}{4}\Delta x}\right) \tag{7.2}$$

During each timestep of size $\Delta t_{rxn}$ in the computation, we perform the following series of updates for the unknowns:

1. Perform the following $M$ times using $\Delta t$

   (a) The discretized Navier-Stokes equations with Brinkman term are solved using a second-order projection method, to give fluid velocities $u, v$, and pressure, $p$.

   (b) Platelets activated within the previous timestep are counted and the ADP release function, $\sigma_{release}$, is updated.

   (c) Mobile platelets are updated to account for advection using LeVeque's high-resolution advection algorithm [39].

2. Mobile platelets and $\eta$ are updated to account for diffusion using a Crank-Nicolson time discretization and the usual spatial-difference approximation to the Laplacian.

3. Perform the following $M$ times using $\Delta t$

   (a) Fluid-phase chemicals are updated to account for advection using LeVeque's high-resolution advection algorithm [39].

   (b) All platelet species are updated to account for reactions using a second-order Runge-Kutta solver. (Reactions for platelet species are updated separately using the smaller timestep in order to test different values for $k_{coh}$ which may differ by multiple orders of magnitude.)

4. Fluid-phase chemicals are updated to account for diffusion using a Crank-Nicolson time discretization and the usual spatial-difference approximation to the Laplacian.

5. All nonplatelet species are updated to account for reactions using a second-order Runge-Kutta solver.

6. The platelet fractions of bound platelets, $\phi^B$ and $\phi^T$, are calculated and $\alpha(\phi^B)$ and $W(\phi^T)$ are updated.

7. Repeated until desired time.

In this chapter, we describe the numerical methods used to perform these updates. First, we describe the projection method used to solve for the unknowns in the fluid equations. Then we discuss the fractional step method used to advance the advection-diffusion-reaction equations for both the mobile chemical and mobile platelet species. We describe two different diffusion and advection solvers due to the special treatment needed for the platelet-density-dependent diffusion and advection of the mobile platelet species. For immobile species that only react, the same numerical method as used for the reaction step of the mobile species is employed.

## 7.1 Projection Method for Fluid Equations

Approximate solutions to equations (2.1) and (2.2) were obtained using finite-difference methods. The spatial discretization including the definitions of discrete gradient $\nabla^h$, divergence $\nabla^h\cdot$, and Laplacian operator $\Delta^h$ is described below. First we discuss the temporal discretization which is based on the role the pressure plays of enforcing the

incompressibility condition (2.2). Our method is a fractional-step 'projection method', an approach introduced by Chorin [14, 15] and extended and used extensively by others [58, 7, 12]. In each timestep, the discrete momentum equations are used to obtain an intermediate velocity field $\mathbf{u}^*$ that accounts for all of the forces that act on the fluid except the pressure gradient

$$\frac{\mathbf{u}^* - \mathbf{u}^n}{\Delta t} + \mathbf{a}^{n+\frac{1}{2}} = \mu \Delta^h \left( \frac{\mathbf{u}^* + \mathbf{u}^n}{2} \right) - \mu \alpha \mathbf{u}^*. \tag{7.3}$$

Here, $\Delta t$ is the size of the timestep, $\mathbf{u}^n$ is the velocity field at the beginning of the timestep, $\mathbf{a}^{n+\frac{1}{2}}$ is an approximation to the nonlinear advection terms at the middle of the timestep, and $\Delta^h$ is a finite-difference approximation to the Laplacian operator. For reasons of numerical stability, the viscous and Brinkman terms involve the unknown intermediate velocity field $\mathbf{u}^*$. The nonlinear advection term is calculated using only known quantities,

$$\mathbf{a}^{n+\frac{1}{2}} = \frac{3}{2}\mathbf{a}^n - \frac{1}{2}\mathbf{a}^{n-1} \tag{7.4}$$

so equation (7.3) constitutes a system of linear equations for $\mathbf{u}^*$. The field $\mathbf{u}^*$ generally does not satisfy the (discrete) incompressibility condition.

$$\nabla^h \cdot \mathbf{u} = 0. \tag{7.5}$$

A final new (discretely) incompressible velocity field $\mathbf{u}^{n+1}$ is obtained from equations which incorporate the unknown pressure gradient and the incompressibility constraint:

$$\frac{\mathbf{u}^{n+1} - \mathbf{u}^*}{\Delta t} = -\nabla^h p \tag{7.6}$$

$$\nabla^h \cdot \mathbf{u}^{n+1} = 0. \tag{7.7}$$

One way to think about (7.6) is in the form $\mathbf{u}^* = \mathbf{u}^{n+1} + \Delta t \nabla^h p$ which shows that $\mathbf{u}^{n+1}$ is the projection of the intermediate velocity field $\mathbf{u}^*$ onto the space of discretely divergence-free velocity fields. In practice, equation (7.6) is converted to a Poisson equation for $p$ by applying the operator $\nabla^h \cdot$ to all terms in (7.6) and using (7.7):

$$\Delta^h p = \frac{1}{\Delta t} \nabla^h \cdot \mathbf{u}^*. \tag{7.8}$$

Once $p$ is determined from this equation, $\mathbf{u}^{n+1}$ is set to

$$\mathbf{u}^{n+1} = \mathbf{u}^* - \Delta t \nabla^h p. \tag{7.9}$$

Hence, the calculations in a single timestep are to (1) solve the linear system equation (7.3) for $\mathbf{u}^*$ (using SOR iteration, described below), (2) solve equation (7.8) for $p$ (using multigrid, described below), and (3) set $\mathbf{u}^{n+1}$ using equation (7.9).

For the spatial discretization we use a rectangular MAC grid [59], with spacing $h$ in both coordinate directions, as shown in Figure 7.1. Scalar variable such as pressure $p$, or $\nabla^h \cdot \mathbf{u}^*$ are represented at cell centers, x-components of vector variables such as velocity are represented at the midpoints of left and right (LR) cell edges and y-components of vector variables are defined at the midpoints of top and bottom (TB) cell edges. For example, the variables in cell $(ij)$ are the pressure $p_{ij}$, the LR edge x-component velocity $u_{i\pm\frac{1}{2},j}$, and the TB edge component velocity $v_{i,j\pm\frac{1}{2}}$.

The discrete pressure gradient $\nabla^h p$, being a vector quantity, is defined at cell edges. Its x-component at the right edge of cell $(ij)$ is

$$\frac{p_{i+1,j} - p_{i,j}}{h},$$

and its y-component at the top edge of cell $(ij)$ is

$$\frac{p_{i,j+1} - p_{i,j}}{h}.$$

The discrete divergence operator applied to a vector variable gives a scalar output defined at cell centers. For example, the value of $\nabla^h \cdot \mathbf{u}^*$ in cell $(ij)$ is

$$\frac{u^*_{i+\frac{1}{2},j} - u^*_{i-\frac{1}{2},j}}{h} + \frac{v^*_{i,j+\frac{1}{2}} - v^*_{i,j-\frac{1}{2}}}{h}.$$

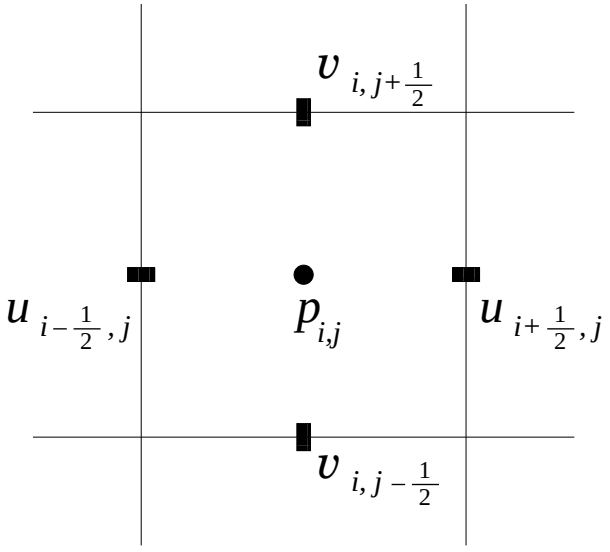


**Figure 7.1**. MAC grid

The discrete Laplacian operator applied to any variable is the usual five-point discrete Laplacian operator relevant to the variable in question. For x-components of velocity, it defines values at LR edges; for example,

$$\begin{aligned}(\Delta^h u^*)_{i+\frac{1}{2},j} &= \Big(u^*_{i+\frac{1}{2},j-1} + u^*_{i-\frac{1}{2},j} \\ &- 4u^*_{i+\frac{1}{2},j} + u^*_{i+\frac{3}{2},j+1} + u^*_{i+\frac{1}{2},j}\Big)/h^2\end{aligned}$$

defines a value at the right edge of cell $(ij)$. Similarly,

$$\begin{aligned}(\Delta^h p)_{ij} &= (p_{i,j-1} + p_{i-1,j} \\ &- 4p_{ij} + p_{i+1,j} + p_{i,j+1})/h^2\end{aligned}$$

defines the value of the discrete Laplacian of the pressure at the center of cell $(ij)$. The three spatial difference operators all use centered-differencing and so are second order accurate. Note that it follows from the definitions of $\nabla^h$, $\nabla^h\cdot$, and $\Delta^h$, that

$$\Delta^h p = \nabla^h \cdot (\nabla^h p),$$

so the formulas (7.8) and (7.9) give an exact projection, i.e. $\nabla^h \cdot \mathbf{u}^{n+1} = 0$. This is an advantage of using the MAC grid.

Finally, we come to the spatial discretization of the nonlinear advection terms. For the continuum equations, $\nabla \cdot \mathbf{u} = 0$ implies that

$$\mathbf{u} \cdot \nabla \mathbf{u} = \nabla \cdot (\mathbf{u}\mathbf{u}^T) = \begin{pmatrix} (uu)_x + (uv)_y \\ (uv)_x + (vv)_y \end{pmatrix}$$

where $\mathbf{u}\mathbf{u}^T$ denotes the outer-product of $\mathbf{u}$ with itself, and the divergence operator is applied to each row of this matrix. For the MAC grid, discretizations based on the alternative 'conservative form' require approximations to $(uu)_x$ and $(uv)_y$ at LR cell edges, and approximations to $(uv)_x$ and $(vv)_y$ on TB cell edges. The approximations for $(uu)_x$ and $(vv)_y$ are straightforward:

$$\begin{aligned}[(uu)_x]_{i+\frac{1}{2},j} &\approx \frac{u^2_{i+\frac{3}{2},j} - u^2_{i-\frac{1}{2},j}}{2h}, \\ [(vv)_y]_{i,j+\frac{1}{2}} &\approx \frac{v^2_{i,j+\frac{3}{2}} - v^2_{i,j-\frac{1}{2}}}{2h}.\end{aligned}$$

The approximation for $(uv)_y$ at a LR edge is more complicated because $v$ is not defined on the LR cell edges. To overcome this difficulty, we define a value of v at each LR edge

by averaging the values of $v$ from the four TB edges closest to the LR edge in question. Letting $\bar{v}$ denote the average, we have

$$\bar{v}_{i+\frac{1}{2},j} = \frac{1}{4}\left(v_{i,j+\frac{1}{2}} + v_{i,j-\frac{1}{2}} + v_{i+1,j+\frac{1}{2}} + v_{i,j-\frac{1}{2}}\right).$$

Then, we use the approximation

$$[(uv)_y]_{i+\frac{1}{2},j} \approx \frac{\bar{v}_{i+\frac{1}{2},j+1}u_{i+\frac{1}{2},j+1} - \bar{v}_{i+\frac{1}{2},j-1}u_{i+\frac{1}{2},j-1}}{2h}.$$

A similar procedure is used to approximate $(uv)_x$ at TB cell edges.

### 7.1.1 SOR

Within the projection method, we solve the linear system given by equation (7.3), for $\mathbf{u}^*$. We use the Crank-Nicholson scheme for the time discretization of the viscous term and the backward Euler scheme for the Brinkman term. This choice of discretization gives:

$$\frac{\mathbf{u}^* - \mathbf{u}^n}{\Delta t} + \mathbf{a}^{n+\frac{1}{2}} = \mu\Delta^h\left(\frac{\mathbf{u}^* + \mathbf{u}^n}{2}\right) - \mu\alpha\mathbf{u}^*, \tag{7.10}$$

where $\Delta^h$ is the same five-point discrete Laplacian as described above. Rearranging, we get the following:

$$\left((1+\mu\alpha)I - \frac{\Delta t}{2}\Delta^h\right)\mathbf{u}^* = \left(I + \frac{\Delta t}{2}\Delta^h\right)\mathbf{u}^n + \mathbf{a}^{n+1/2} \tag{7.11}$$

With $\mathbf{a}^{n+1/2}$ as known data, we can solve this system of equations using an iterative method. We chose the method of successive overrelaxation (SOR) and will now briefly describe it.

Given a linear system $A\mathbf{x} = \mathbf{b}$ of $n$ equations, we can split $A$ by the decomposition into two matrices $A = M - K$ such that $M$ is nonsingular. This splitting gives

$$A\mathbf{x} = M\mathbf{x} - K\mathbf{x} = \mathbf{b},$$

which leads to the fixed point problem

$$\mathbf{x} = M^{-1}K\mathbf{x} + M^{-1}\mathbf{b},$$

and thus implies an iterative solution method

$$\mathbf{x}_{k+1} = M^{-1}K\mathbf{x}_k + M^{-1}\mathbf{b}.$$

A particular decomposition of $A$ into a diagonal, upper and lower triangular part ($A = D + U + L$), where $M = D - L$ is nonsingular and $K = U$, leads to the following scheme:

$$\mathbf{x}_k{+}1 = (D - L)^{-1}(U\mathbf{x}_k + \mathbf{b}).$$

This is called the Gauss-Seidel iterative method by which we begin with an initial guess $\mathbf{x}_0$ and iterate until we converge to the desired solution. To accelerate the rate of convergence

of the Gauss-Seidel method, we use SOR, where in each iteration, we use the weighted average between the previous iterate and the computed Gauss-Seidel iterate successively:

$$\mathbf{x}_{k+1} = (D - \omega L)^{-1}(\omega U + (1 - \omega)D)\mathbf{x}_k + \omega(D - \omega L)^{-1}\mathbf{b},$$

where $\omega$ is called the relaxation parameter. In solving equations (7.10) using this SOR method, we sweep through and update the components in lexicographic order. We found that for these particular equations a value of $\omega = 1.8$ for the relaxation parameter resulted in the lowest number of iterations per timestep.

### 7.1.2 Multigrid

The other system of equations that is solved within the projection method arises from discretizing the Poisson equation for pressure, $p$, as seen in (7.8). It is known that when computing the solution to a discretized Poisson equation, basic iterative methods alone (such as the SOR method previously described) take many iterations to reduce the amplitude of the error, but only a few iterations to smooth it [11, 70, 16]. This means that the high frequency components of the error become small after a few iterations, but the low frequency components change only slightly. This characteristic of basic iterative methods is called the *smoothing principle* [70]. Another useful principle is the *coarse grid principle* which says that any quantity that is smooth on a certain grid can be appoximated on a coarser grid without essential loss of information [70]. The method of multigrid exploits these principles in the following way.

We will again take the linear system $A\mathbf{x} = \mathbf{b}$ with $n$ equations as our example. Let $\hat{\mathbf{x}}$ be the computed solution. Then the error, $\mathbf{e}$, which measures $\hat{\mathbf{x}}$ as an approximation to $\mathbf{x}$, is given by $\mathbf{e} = \mathbf{x} - \hat{\mathbf{x}}$. We do not have access to the exact solution, thus we do not have access to the error itself. However, another measure that *is* accessible is the residual, $\mathbf{r} = \mathbf{b} - A\hat{\mathbf{x}}$ which is the amount that $\hat{\mathbf{x}}$ fails to satisfy the original equation. Using this definition for the residual, we can solve for the error with $A\mathbf{e} = \mathbf{r}$, which gives a different way to update the solution: $\mathbf{x} = \hat{\mathbf{x}} + \mathbf{e}$.

We begin the solution process by using an iterative method such as SOR, but just until the error is smooth, so we have to iterate only a few times. Since the smooth error can be approximated on a coarser grid without the loss of essential information, we *move* the current residual along with the matrix $A$ to a coarser grid on which the error equation, $A\mathbf{e} = \mathbf{r}$ is then solved. The error is then *moved* back to the finer grid where it is added the current value of the computed solution, $\hat{\mathbf{x}}$. This process is then repeated until the

desired solution is obtained. There can also be more that one coarse grid; a sequence of grids in which the mesh size doubles successively can, in fact, be used. There are also many different ways in which information is moved, or transferred, between grids. This is just an overview of the solution process by which we solve our Poisson equation for the pressure. Details of how we use this process on a cell-centered grid and the information transfer operations that we use are fully described in [25].

## 7.2 Mobile Chemical Species

Each of the mobile chemical species has equations of the form:

$$\frac{\partial C}{\partial t} = -\nabla \cdot (\mathbf{u}C - D\nabla C) + R(C) \tag{7.12}$$

where $\mathbf{u}$ is the two-dimensional fluid velocity and $D$ and $R(C)$ are the diffusion coefficient and reaction terms associated with a particular chemical species, respectively. To advance these equations in time, we use a fractional step method. Within each time step of size $\Delta t$, we solve separate equations for advection, diffusion and reaction. Let $c$ represent the numerical solution to equation 7.12. Then to advance one time step from $c^n$ to $c^{n+1}$, we perform the following set of updates. First, update the discrete version of

$$\frac{\partial C}{\partial t} = -\nabla \cdot (\mathbf{u}C) \tag{7.13}$$

for $\Delta t$ time, to go from $c^n$ to $c^*$. Then update the discrete version of

$$\frac{\partial C}{\partial t} = \nabla \cdot (D\nabla C) \tag{7.14}$$

for $\Delta t$ time, to go from $c^*$ to $c^{**}$. Finally, we update the discrete version of

$$\frac{\partial C}{\partial t} = R(C), \tag{7.15}$$

for $\Delta t$ time, to get from $c^{**}$ to $c^{n+1}$. We now describe the methods used to approximate the intermediate and end solutions.

### 7.2.1 Advection Equation

Equation 7.13 is written in the *conservative* form, but can be also be written in the *advective* form:

$$\frac{\partial C}{\partial t} = -\mathbf{u} \cdot \nabla C. \tag{7.16}$$

since the fluid is incompressible. Equation 7.16 is mathematically equivalent to equation (7.13), but has some advantages and disadvantages when it comes to discretizing. In areas

where $C$ is constant but the velocity is not, the conservative differencing will preserve the total amount of $C$, but may produce a nonconstant $C$. Advective differencing will produce a constant $C$ but may not preserve total mass. We use a high-resolution conservative algorithm developed by LeVeque [39] that mixes these two forms of differencing.

For this algorithm, which requires that $C$ be discretized on a cell-centered grid, $C^n_{ij}$ represents the cell-average of $C$ over the grid cell $\Gamma_{ij}$. This method uses fluid velocities as well as the numerical fluxes, both of which are located at the cell-edges. The functions $F_{i\pm\frac{1}{2},j}$ and $G_{i,j\pm\frac{1}{2}}$, represent the numerical fluxes of $C$ across the left, right, bottom, and top edges, respectively. To advance one time step from time $m$ to time $m+1$, we use the final update formula

$$c^{m+1}_{ij} = c^m_{ij} - \frac{\Delta t}{h}(F_{i+\frac{1}{2},j} - F_{i-\frac{1}{2},j} + G_{i,j+\frac{1}{2}} - G_{i,j-\frac{1}{2}}), \tag{7.17}$$

where $h$ is distance between two cell centers, or the length of one grid cell. As mentioned above, we are updating the discrete version of equation (7.13) for $\Delta t$ time to go from $c^n$ to $c^*$, but for simplicity in this section, we will use the notation $c^m$ and $c^{m+1}$ instead of $c^n$ and $c^*$. We will also assume for the rest of this section that both $u$ and $v$ are positive.

Imagine constructing a function, $\tilde{c}(\mathbf{x}, t^m)$, from the given cell averages $c^m_{ij}$. First assume that $\tilde{c}$ is piecewise constant such that its value at $c^m_{ij}$ is the average of $c$ over the grid cell $\Gamma_{ij}$. We can view the discontinuities in $\tilde{c}$ at the cell interfaces between $\Gamma_{i-\frac{1}{2}j}$ and $\Gamma_{ij}$ and between $\Gamma_{ij-\frac{1}{2}}$ and $\Gamma_{ij}$ as giving rise to waves that propagate into cell $\Gamma_{ij}$, modifying the value of $c$ as they pass through. Waves carrying the jumps $(c^m_{ij} - c^m_{i-1j})$ and $(c^m_{ij} - c^m_{ij-1})$ propagate independently into the cell at speeds given by $u$ and $v$, respectively, in the directions normal to the cell edges. To implement this, we use the "donor-cell" upwind method, and use *conservative* differencing such that:

$$F_{i-\frac{1}{2},j} = F_{i-\frac{1}{2},j} + u_{i-\frac{1}{2},j}c^m_{i-1j} \tag{7.18}$$

$$G_{i,j-\frac{1}{2}} = G_{i,j-\frac{1}{2}} + v_{i,j-\frac{1}{2}}c^m_{ij-1}. \tag{7.19}$$

If we then add similar fluxes for this cell's two other edges, it is clear that

$$c^{m+1}_{ij} = c^m_{ij} - \frac{\Delta t}{h}(u_{i+\frac{1}{2},j}c^m_{ij} - u_{i-\frac{1}{2},j}c^m_{i-1j} + v_{i,j+\frac{1}{2}}c^m_{ij} - v_{i,j-\frac{1}{2}}c^m_{ij-1}) \tag{7.20}$$

approximates the *conservative* form of equation (7.13). This is seen by

$$\begin{aligned} -\nabla\cdot(\mathbf{u}C) &= uC_x + vC_y + C(u_x + v_y) \\ &= uC_x + vC_y \end{aligned}$$

because the velocity field is incompressible. We note here that this is the only step in which we use conservative differencing. We improve the stability of this method by accounting for the transverse propagation of the wave and add in its effects to the cells above and to the right of $\Gamma_{ij}$. To do this, we increment the fluxes at the top and right by

$$G_{i,j+\frac{1}{2}} = G_{i,j+\frac{1}{2}} - \frac{\Delta t}{2h} u_{i-\frac{1}{2},j} v_{i,j+\frac{1}{2}} (c^m_{ij} - c^m_{i-1j}) \tag{7.21}$$

$$F_{i+\frac{1}{2},j} = F_{i+\frac{1}{2},j} - \frac{\Delta t}{2h} v_{i,j-\frac{1}{2}} u_{i+\frac{1}{2},j} (c^m_{ij} - c^m_{ij-1}). \tag{7.22}$$

This is a two-step procedure in which $c_{ij}$ is modified by propagating a piecewise constant wave (LeVeque calls this the *increment wave*) and together, these steps give a method that is still first order accurate, but with better stability properties and smaller error constant than the upwind method alone.

To make this method second order accurate, we will add two more steps. Imagine now that $\tilde{c}$ is a piecewise linear function. Since we already accounted for the propagation of the cell averages, we must use piecewise linear approximations that have mean 0 between the cells. We will modify $c_{ij}$ with two steps where we propagate a piecewise linear wave (LeVeque calls this the *correction wave*) in the normal and transverse directions.

For propagation in the normal $x$ direction, the approximation in $\Gamma_{ij}$ is linear in $x$, constant in $y$, and has slope $\sigma_{i-\frac{1}{2}j} = \frac{1}{h}(c^m_{ij} - c^m_{i-1j})\Phi_{i-\frac{1}{2}j}$, where $\Phi_{i-\frac{1}{2}j}$ is a limiter used to prevent the introduction of oscillations when there are steep gradients in $c$. Let $S$ represent the first set of corrections to the flux due to the normal propagation of the wave. At the left and bottom edge of the cell, the corrections are

$$S_{i-\frac{1}{2},j} = \frac{h}{2}|u_{i-\frac{1}{2},j}| \left(1 - \frac{\Delta t}{h}|u_{i-\frac{1}{2},j}|\right) \sigma_{i-\frac{1}{2}j} \tag{7.23}$$

$$S_{i,j-\frac{1}{2}} = \frac{h}{2}|v_{i,j-\frac{1}{2}}| \left(1 - \frac{\Delta t}{h}|v_{i,j-\frac{1}{2}}|\right) \sigma_{ij-\frac{1}{2}}. \tag{7.24}$$

The modification to the fluxes is then given by:

$$F_{i-\frac{1}{2},j} = F_{i-\frac{1}{2},j} + S_{i-\frac{1}{2},j} \tag{7.25}$$

$$G_{i,j-\frac{1}{2}} = G_{i,j-\frac{1}{2}} + S_{i,j-\frac{1}{2}}. \tag{7.26}$$

So far, the method is second order-accurate; however, better results can be obtained by adding in the transverse propagation. We will use one last step, which is the additional correction due to the transverse propagation of the linear profiles. We update the fluxes

at the top and right of cell $\Gamma_{ij}$ but now, because of the linear profile, we must also update the flux at the top of the adjacent cell $\Gamma_{i-1j}$ and the right of the adjacent cell $\Gamma_{ij-1}$:

$$G_{i,j+\frac{1}{2}} = G_{i,j+\frac{1}{2}} + \frac{\Delta t}{h} v_{i,j+\frac{1}{2}} S_{i,j+\frac{1}{2}} \tag{7.27}$$

$$G_{i-1,j+\frac{1}{2}} = G_{i-1,j+\frac{1}{2}} - \frac{\Delta t}{h} v_{i-1,j+\frac{1}{2}} S_{i-\frac{1}{2},j+\frac{1}{2}} \tag{7.28}$$

$$F_{i+\frac{1}{2},j} = F_{i+\frac{1}{2},j} + \frac{\Delta t}{h} v_{i+\frac{1}{2},j} S_{i+\frac{1}{2},j} \tag{7.29}$$

$$F_{i+\frac{1}{2},j-1} = F_{i+\frac{1}{2},j-1} - \frac{\Delta t}{h} v_{i+\frac{1}{2},j-1} S_{i+\frac{1}{2},j-\frac{1}{2}}. \tag{7.30}$$

### 7.2.2 Diffusion Equation

We begin by describing the discretization of Equation 7.14. Although, the diffusion coefficient here appears to be constant in space, we treat is as a spatially-varying coefficient for future applications. Therefore, after expanding out the terms in Equation 7.14, we obtain:

$$\frac{\partial C}{\partial t} = (DC_x)_x + (DC_y)_y. \tag{7.31}$$

We then use the standard Crank-Nicholson time discretization together with central differences in each spatial direction. Since the diffusion coefficient is inside of a spatial derivative, computing the central differences requires the evaluation of the diffusion coefficient on the cell edges, half-way between the cell-centered grid points. For simplicity, we will show the discretization of the one-dimensional equation:

$$\frac{\partial C}{\partial t} = (DC_x)_x. \tag{7.32}$$

This discretization looks like:

$$\begin{aligned} \frac{c_i^{n+1} - c_i^n}{\Delta t} &= \frac{1}{2(\Delta x)^2} \Big[ D_{i-\frac{1}{2}} c_{i-1}^{n+1} - (D_{i-\frac{1}{2}} + D_{i+\frac{1}{2}}) c_i^{n+1} + D_{i+\frac{1}{2}} c_{i+1}^{n+1} \\ &+ D_{i-\frac{1}{2}} c_{i-1}^{n} - (D_{i-\frac{1}{2}} + D_{i+\frac{1}{2}}) c_i^{n} + D_{i+\frac{1}{2}} c_{i+1}^{n} \Big] \end{aligned} \tag{7.33}$$

and rearranging, becomes the following system of equations:

$$\begin{aligned} c_i^{n+1} &- \frac{\Delta t}{2(\Delta x)^2} (D_{i-\frac{1}{2}} c_{i-1}^{n+1} - (D_{i-\frac{1}{2}} + D_{i+\frac{1}{2}}) c_i^{n+1} + D_{i+\frac{1}{2}} c_{i+1}^{n+1}) \\ &= c_i^n + \frac{\Delta t}{2(\Delta x)^2} (D_{i-\frac{1}{2}} c_{i-1}^{n} - (D_{i-\frac{1}{2}} + D_{i+\frac{1}{2}}) c_i^{n} + D_{i+\frac{1}{2}} c_{i+1}^{n}). \end{aligned} \tag{7.34}$$

The variables for the chemical species are represented at the centers of the computational grid cells, in the same location as the pressure, seen in Figure 7.1. However, the

physical boundary of the computational domain is located on cell edges, as depicted in Figure 7.2, and must be handled in the following slightly unusual way.

All of the mobile species have specified upstream concentrations that are represented as Dirichlet conditions on the left boundary and move freely downstream represented by a homogeneous Neumann boundary condition at the right boundary. The injury site or endothelium is located on the bottom boundary and the chemicals are not allowed to interact with other parts of the vessel walls (top and bottom not including the injury site or endothelium) and therefore have no flux conditions on the top boundary and part of the bottom boundary. At the injury site or endothelium, some of the chemicals interact with subendothelium-bound or endothelium-bound chemicals and this is represented through a Robin or Neumann boundary condition, depending on the species. We will describe how we handle the Robin condition since it incorporates the same terms as if there were just a Neumann condition. The general form of this bottom boundary condition is:

$$D\frac{\partial C}{\partial y} = \kappa C - \beta, \tag{7.35}$$

where $C$ represents the concentration of the chemical in the fluid immediately adjacent to the physical boundary (see Figure 7.2). We again use a centered difference for the $y$ derivatives and to keep the same order of accuracy as at the interior points, we use a Crank-Nicholson time discretization and the equation becomes:

$$\frac{D}{2}\frac{\left(C_{i,1}^{n+1} + C_{i,1}^{n}\right) - \left(C_{i,0}^{n+1} + C_{i,0}^{n}\right)}{\Delta y} = \kappa\frac{C_{i,1/2}^{n+1} + C_{i,1/2}^{n}}{2} - \frac{\beta^{n+1} + \beta^{n}}{2}, \tag{7.36}$$

For computational ease, we use ghost cells around all edges of the domain so that the operator stencil used in the interior of the domain (equation 7.34 plus the $y$ direction

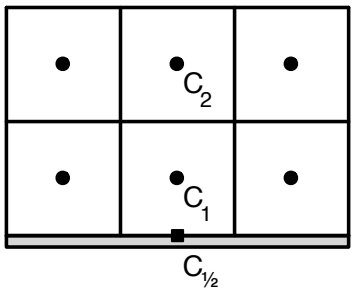


**Figure 7.2**. Shaded region represents location of physical boundary. All chemical and platelet species are represented at cell-centers, as depicted as black circles. The chemical concentration at the physical boundary, $C_{1/2}$, represented by a black square is computed by extrapolating values from $C_1$ and $C_2$.

analogs) may be used at the boundaries as well. The values for the ghost cells at the bottom boundary at time $n$ are:

$$C_{i,0}^{n} = C_{i,1}^{n} - \frac{\Delta y}{D}\left(\kappa C_{i,1/2}^{n} - \beta^{n}\right). \tag{7.37}$$

Similarly, the ghost cell values at time $n+1$ are:

$$C_{i,0}^{n+1} = C_{i,1}^{n+1} - \frac{\Delta y}{D}\left(\kappa C_{i,1/2}^{n+1} - \beta^{n+1}\right). \tag{7.38}$$

The last term to describe here is the value of the chemical species concentration at the physical boundary, $C_{i,1/2}$. To compute this value, we use linear extrapolation such that:

$$C_{i,1/2} = \frac{3}{2}C_{i,1} - \frac{1}{2}C_{i,2}. \tag{7.39}$$

To solve the discretized version of equation 7.31 together with the discretized boundary conditions as just described, we use SOR iteration. For this system, we found that a value of 1.01 for the relaxation parameter (making this almost a Gauss-Seidel method) results in the smallest number of iterations per time step for each chemical species.

### 7.2.3 Reaction Equation

All of the reaction terms are indeed spatial but there is no coupling between the grid cells, that is, we only need to solve ordinary differential equations at each grid point. To accomplish this we use a second-order Runge-Kutta method, also called Heun's method, for all of the reaction terms in all of the equations. To advance the discrete version of the reactions as in equation (7.15) from $c^{**}$ to $c^{n+1}$, we use the following steps:

$$k_1 = R(c^{**}) \tag{7.40}$$

$$k_2 = R(c^{**} + \Delta t k_1) \tag{7.41}$$

$$c^{n+1} = c^{**} + \frac{\Delta t}{2}(k_1 + k_2). \tag{7.42}$$

## 7.3 Mobile Platelets

The transport of mobile platelets depends on the density of bound platelets, quantities that are represented at cell-centers, and therefore must be treated differently than the transport of chemicals as described above. The equation for the transport of mobile platelets is of the form:

$$\frac{\partial P}{\partial t} = -\nabla \cdot \left\{ w \left( \mathbf{u}P - D\nabla P \right) \right\}, \tag{7.43}$$

where, for simplicity, we take $w = W(\phi^T)$ and let $w_{i,j} = W(\phi_{i,j}^T)$. We again use a fractional step method to solve the equations for the mobile platelets, consisting of an advection,

diffusion and reaction step. We first describe the changes made from numerical methods used to solve the chemical equations for the advection step and then for the diffusion step. The reaction step is identical to that for the chemical equations.

### 7.3.1 Mobile Platelet Advection

The advection step for mobile platelets consists of updating the discrete version of

$$\frac{\partial P}{\partial t} = -\nabla \cdot (w\mathbf{u}P). \tag{7.44}$$

We use a method similar to that described in section 7.2.1. The main difference here is that the new velocity field, $w\mathbf{u}$ is *not* incompressible, and thus we cannot simply approximate the advective form of this equation. However, we make use of the the conservative form of the equation in the first step of our algorithm (see section 7.2.1) which is first-order accurate, and proceed by adding on second-order corrections. Letting $U = wu$ and $V = wv$, we can see that in fact,

$$\begin{aligned} -\nabla \cdot (w\mathbf{u}P) &= UP_x + VP_y + P(wu_x + wv_y) \\ &= UP_x + VP_y + wP(u_x + v_y) \\ &= UP_x + VP_y. \end{aligned}$$

The analogous version of equation (7.20) will be

$$P_{ij}^{m+1} = P_{ij}^m - \frac{\Delta t}{h}(U_{i+\frac{1}{2},j}P_{ij}^m - U_{i-\frac{1}{2},j}P_{i-1j}^m + V_{i,j+\frac{1}{2}}P_{ij}^m - V_{i,j-\frac{1}{2}}P_{ij-1}^m). \tag{7.45}$$

One other difference is that our function $w$ is represented at cell-centers whereas the velocities $u$ and $v$ are at cell-edges. To choose the appropriate values for $U$ and $V$ at the edges, we imagine the following situation: two adjacent cells, left with no bound platelets and the right with bound platelets, and a positive velocity $u$, that is, moving from left to right. If there were no bound platelets, the velocity would freely carry mobile platelets from the left cell into the right cell. Therefore, the velocity on the left edge should have some information about the bound platelets in the right cell. Using this logic, we use the following rules to set $U$ at the left edge (for example):

$$U_{i-\frac{1}{2}j} = \begin{cases} w_{ij}u_{i-\frac{1}{2}j}, & u_{i-\frac{1}{2}j} > 0 \\ w_{i-1j}u_{i-\frac{1}{2}j}, & u_{i-\frac{1}{2}j} \leq 0. \end{cases}$$

We then use the same algorithm as described in section 7.2.1, with our new $U$ and $V$ instead of $u$ and $v$.

### 7.3.2 Mobile Platelet Diffusion

The diffusion step consists of updating the discrete version of

$$\frac{\partial P}{\partial t} = \nabla \cdot \left( \hat{D} \nabla P \right). \tag{7.46}$$

The discretization of this equation will be the same as that for the chemical diffusion equation, with the exception that $D$ from the chemical equation is now the product $\hat{D} = wD$. The major difference between solving the two equations is the evaluation of $\hat{D}$ at cell edges. We have to find the value of this product when the values of $\phi^T$, and thus $w$, are only defined at the cell centers. So, which value of $w$ do we choose at the edges? To answer this question we use a left cell-edge as an example. If the density of mobile platelets in cell A is higher than that in cell B, then the platelets should normally diffuse from left to right, or from cell A into cell B. Thus, we want to use the value of $w$ in cell B just in case there are bound platelets there that the mobile platelets cannot diffuse through. Similarly, if the density of mobile platelets in cell A is lower than that of cell B, the mobile platelets would diffuse from right to left, and so we choose $w$ in cell A so that the mobile platelets in cell B will be hindered by any bound platelets that may lie in cell A. Using this logic, we use the following rules to set $\hat{D}$ at the left edge (for example):

$$\hat{D}_{i-\frac{1}{2}j} = \begin{cases} w_{ij} D, & P_{i-1j} > P_{ij} \\ w_{i-1j} D, & P_{i-1j} \leq P_{ij}. \end{cases}$$

We make this choice for each cell edge in the domain and then proceed in the same way that we did for the chemical diffusion.

## 7.4 Convergence Study

There is no analytic solution to the system of equations that we examine in this dissertation. In order to make sure that our numerical method converges, we compare the differences of the numerical solutions between three successive grids to see how the error decreases as the grids become finer. For this convergence study, due to the computational expense of computing on a fine grid, we use a physical domain that is approximately 60 $\mu$m in height and 120 $\mu$m in length, half the size of the domain used in Chapter 3. The

three grids that we use are $32 \times 64$, $64 \times 128$, and $128 \times 256$. We report the convergence at 25 different timesteps for two platelet-bound chemicals, two fluid-phase chemicals, one subendothelium-bound chemical, bound platelets, the fluid velocities and pressure. Neither the cell-centered scalar quantities or the edge-centered fluid velocities overlap on successive grids with this specified refinement ratio (i.e., the grid spacing is halved), so to compare the solutions on successive grids requires averaging. Figure 7.3 shows how the averaging was done for both the cell-centered and MAC grid. The subendothelium-bound chemicals, however, do overlap and the errors we report for these solutions are calculated at the overlapping spatial points.

After averaging, the points between successive grids, $g_i$ and $g_{i+1}$, are compared to obtain the error between the grids. We report how the error decreases as the grid becomes finer using both the two-norm, $E_{i,2} = ||g_i - g_{i+1}||_2$ and the max-norm, $E_{i,\infty} = ||g_i - g_{i+1}||_\infty$ of the error. With three successive grids, we obtain two errors in two different norms. We report the slope that arises between these errors when plotted against the grid-size on a log-log plot. This slope estimates the rate of convergence of our method.

Figures 7.4 and 7.5 show plots of these slopes as a function of time for the two platelet-

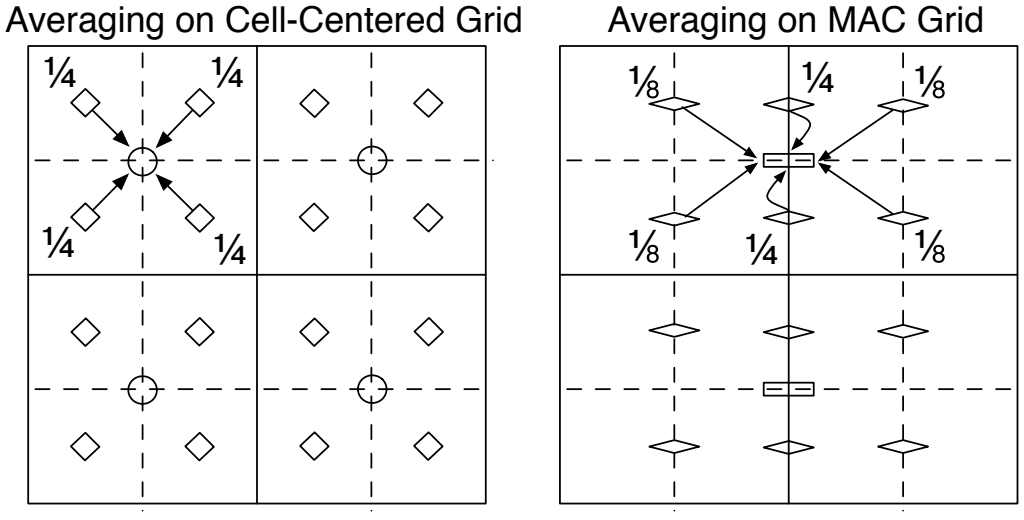


**Figure 7.3**. Averaging schemes for comparing numerical solutions on two successive grids. Dashed lines indicate the edges of the fine grid and solid lines indicated edges of the coarse and fine grid. Left: four spatial points on the finer grid (diamonds) are equally averaged to compare to the solution at a point the coarser grid (circle) using a cell-centered grid. Right: six spatial points on the finer grid (squished diamonds) are unequally averaged to compare to the solution at a point the coarser grid (rectangle) using a MAC grid. This MAC grid is an example of the velocity, $u$, but we use a similar scheme for the velocity, $v$.

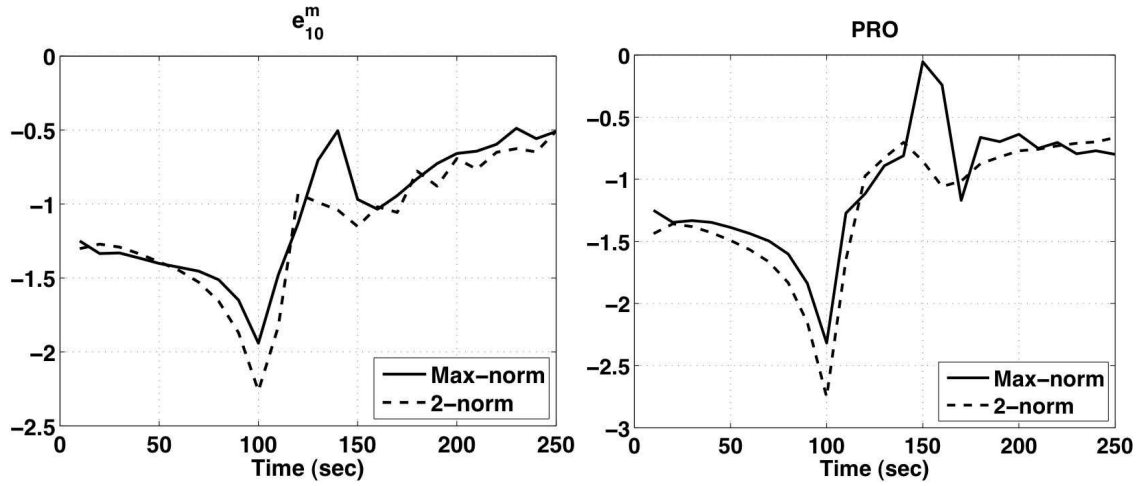


**Figure 7.4**. Rates of convergence as a function of time for the platelet-bound chemicals, $e_{10}^m$ and prothrombinase. A value of $-1$ indicates first order convergence.

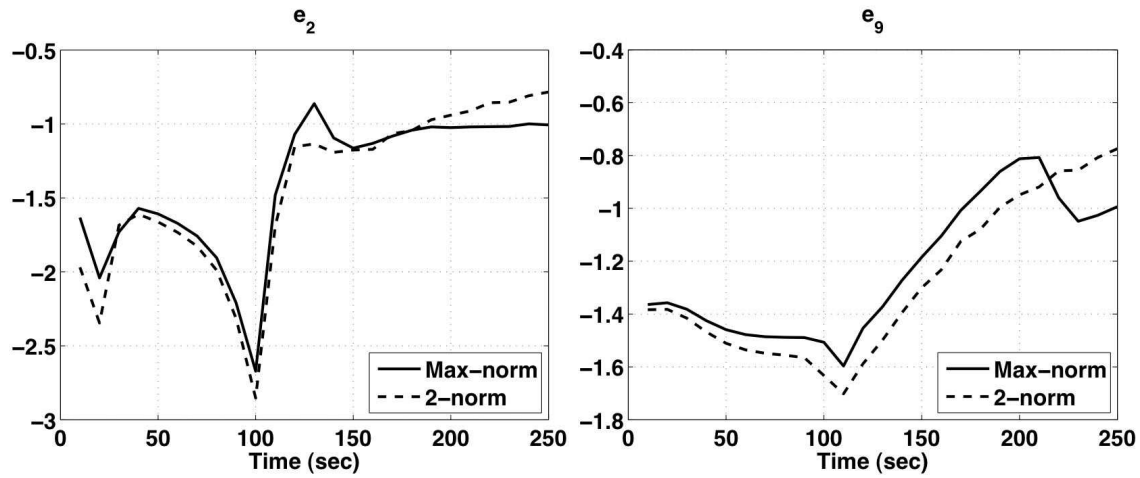


**Figure 7.5**. Rates of convergence as a function of time for the fluid-phase chemicals, $e_2$ and $e_9$. A value of $-1$ indicates first order convergence.

bound chemicals $e_{10}^m$ and prothrombinase and the two fluid-phase chemicals, $e_2$ and $e_9$. At approximately 100 seconds, thrombin production begins to increase rapidly which leads to platelet activation and thus more thrombin production and growth of the thrombus. It is clear from the figures that in the first 100 seconds of the simulation, when some of these chemicals are found in low quantities, the convergence in better than first-order. Once the thrombus begins to grow, the convergence of all species begins to decrease.

Figure 7.6 displays the error slopes for bound activated platelets and the subendothelium-

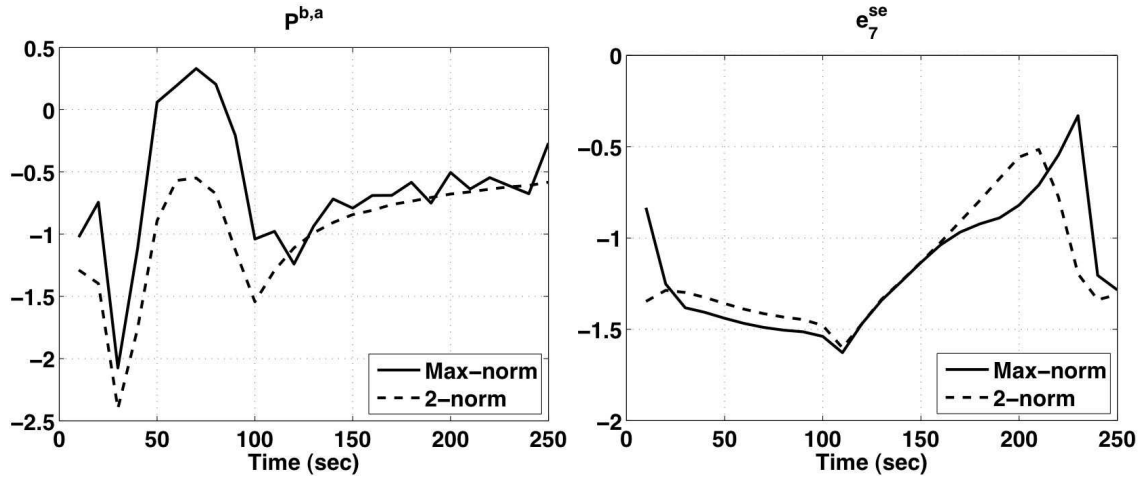


**Figure 7.6**. Rates of convergence as a function of time for the bound activated platelets and the subendothelium-bound chemcal, $e_7^{se}$. A value of $-1$ indicates first order convergence.

bound chemical $e_7^{se}$. One major difference in these plots is that for the times between 50 and 100 seconds, slopes calculated with the max-norm grow positive indicating that the method doesn't converge. However, the measurement using the max-norm picks out specific points on the corners of the growing thrombus and does not represent the majority of the spatial domain. Since the method converges in the two-norm during that time interval, we consider the method to be convergent during all times.

Finally, Figures 7.7 and 7.8 show the slopes for the fluid velocities and pressure. From these figures we conclude that, on average, the method we use to solve for the fluid velocities and pressure converges approximately first order or better.

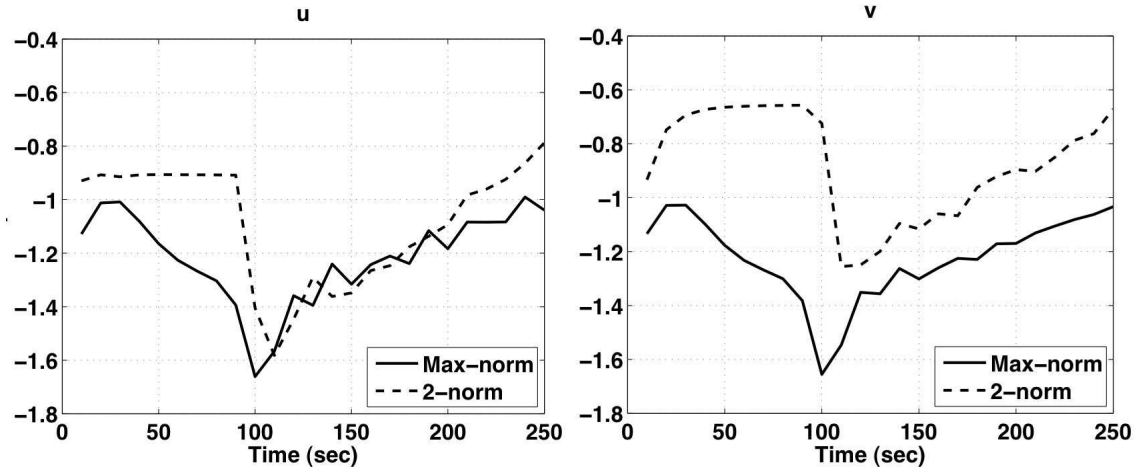


**Figure 7.7**. Rates of convergence as a function of time for the fluid velocities, $u$, and $v$. A value of $-1$ indicates first order convergence.

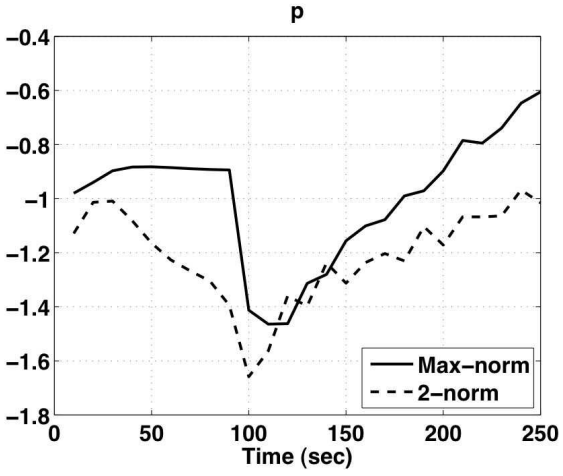


**Figure 7.8**. Rate of convergence as a function of time for the pressure, $p$. A value of $-1$ indicates first order convergence.

# CHAPTER 8

# FUTURE DIRECTIONS

In the studies described in this dissertation, we do not distinguish between the activation state of platelets activated in different ways. In reality, ADP, thrombin, and subendothelial collagen elicit different subsets of the full range of platelet activation responses [31]. For example, ADP-activated platelets are not procoagulant without further stimulus, and there is some evidence that platelets activated by both collagen and thrombin are more procoagulant than platelets activated by either collagen or thrombin alone [50]. Assuming the latter is true, this would be another cause for spatial heterogeneity within a thrombus, as only platelets close to the injured wall could be activated by collagen. There is also increasing indication that unactivated platelets may be able to bind, if only transiently, to a growing thrombus [30, 64]. By increasing the time that a platelet is in the vicinity of a developing thrombus, such binding would increase the platelet's time of exposure to chemical agonists and this would possibly lead to more activation and faster thrombus growth.

The experimental studies conducted at the Nemerson lab [26] that gave experimental support to the hypothesis that platelets adhering to the subendothelium cover and so physically inhibit subendothelial-bound enzymes, also explored the transport characteristics of FXa within a thrombus in the presence of platelets and fibrin. They found that there was physical impedance on FXa transport imposed by platelets.

In the following sections, we describe our ideas for incorporating some of these behaviors into the LF model.

## 8.1 New Platelet Species

In addition to the four species of platelets in the LF model ($P^{m,a}$, $P^{m,u}$, $P^{b,a}$, $P^{se,a}$), we will include three new species of platelets. The first species, $P^{b,u}$, represents platelets that are not yet chemically activated, but have temporarily (reversibly) attached to another

bound platelet. We assume that both the attachment and detachment have functional forms that depend on the local shear rate, $\gamma_f$ .

We will also introduce two species of ADP-activated platelets, mobile ADP-activated platelets $P^{m,adp}$ and bound ADP-activated platelets $P^{b,adp}$. The former are activated by ADP in the fluid while mobile. The latter are produced when mobile ADP-activated platelets bind to the thrombus, or when bound, unactivated platelets ($P^{b,u}$) are activated by ADP. The bound platelets partially activated by ADP may subsequently become fully activated by thrombin.

### 8.1.1 Bound Unactivated Platelets, $P^{b,u}$

The bound, unactivated platelets are a function of $\mathbf{x}$ and $t$, and their evolution equation is:

$$\begin{aligned}\frac{\partial P^{b,u}}{\partial t} &= k^{(2)}_{coh}(\gamma_f)P^{m,u}g(\eta) - k^{(2)}_{det}(\gamma_f)P^{b,u} \\ &\quad - (k^{b,u}_{act}A_{e_2}(e_2) + k^{adp}_{act}A_{adp}(ADP))P^{b,u} \\ &\quad - k^{(2)}_{adh}(\mathbf{x})(P_{max} - P^{se,a})P^{b,u}.\end{aligned} \tag{8.1}$$

The terms in this equation describe mobile unactivated platelets cohering at a local-shear-rate dependent rate $k^{(2)}_{coh}(\gamma_f)$, and for bound unactivated platelets their detachment at a local shear rate dependent rate $k^{(2)}_{det}(\gamma_f)$, their activation by thrombin and/or ADP at a rate $k^{b,u}_{act}A_{e_2}(e_2) + k^{adp}_{act}A_{adp}(ADP)$ and their adhesion to the subendothelium.

### 8.1.2 ADP-Activated Platelets, $P^{m,adp}$ and $P^{b,adp}$

The mobile and bound platelets partially activated by ADP are functions of $\mathbf{x}$ and $t$, and their evolution equations are:

$$\begin{aligned}\frac{\partial P^{m,adp}}{\partial t} &= -\nabla \cdot W(\phi^T)(\mathbf{u}(\mathbf{x})P^{m,adp} + D\nabla P^{m,adp}) \\ &\quad - k^{(3)}_{coh}(\gamma_f)g(\eta)P^{m,adp} - k^{(3)}_{adh}(\mathbf{x})(P_{max} - P^{se,a})P^{m,adp} \\ &\quad + k^{adp}_{act}A_{adp}(ADP)P^{m,u} - k^{m,adp}_{act}A_{e_2}(e_2)P^{m,adp},\end{aligned} \tag{8.2}$$

$$\begin{aligned}\frac{\partial P^{b,adp}}{\partial t} &= k^{(3)}_{coh}(\gamma_f)g(\eta)P^{m,adp} - k^{(4)}_{adh}(\mathbf{x})(P_{max} - P^{se,a})P^{b,adp} \\ &\quad - k^{b,adp}_{act}A_{e_2}(e_2)P^{b,adp} + k^{adp}_{act}A_{adp}(ADP)P^{b,u}.\end{aligned} \tag{8.3}$$

These mobile platlets are transported in the same way that mobile platelets in the LF model are transported: by platelet-density-dependent advection and diffusion. The terms in Equation 8.2 describe full activation by thrombin, cohering to other bound platelets, adhering to

the subendothelium, and lastly, mobile, unactivated platelets becoming partially activated by ADP. The terms in Equation 8.3 describe activation of bound, unactivated platelets by ADP, binding of mobile, partially activated platelets, full activation by thrombin, and adhering directly to the subendothelium.

### 8.1.3 Changes to old equations

We account for the new additions (underlined) in the old equations for $P^{m,a}$, $P^{m,u}$, $P^{b,a}$, and $P^{se,a}$ in the following way:

$$\begin{aligned}\frac{\partial P^{m,u}}{\partial t} &= -\nabla \cdot W(\phi^T)(\mathbf{u}(\mathbf{x})P^{m,u} + D\nabla P^{m,u}) \\ &- \underline{k_{act}^{m,u} A_{e_2}(e_2) + k_{act}^{m,adp} A_{adp}(ADP))P^{m,u}} \\ &- k_{adh}(\mathbf{x})(P_{max}^{se} - P^{se,a})P^{m,u} \\ &- \underline{k_{coh}^{(2)}(\gamma_f)P^{m,u}g(\eta) + k_{det}^{(2)}(\gamma_f)P^{b,u}}\end{aligned} \tag{8.4}$$

$$\begin{aligned}\frac{\partial P^{m,a}}{\partial t} &= -\nabla \cdot W(\phi^T)(\mathbf{u}(\mathbf{x})P^{m,a} + D\nabla P^{m,a}) \\ &+ \underline{k_{act}^{m,u} A_{e_2}(e_2)P^{m,u} + k_{act}^{m,adp} A_{e_2}(e_2)P^{m,adp}} \\ &- k_{adh}(\mathbf{x})(P_{max} - P^{se,a})P^{m,a} - \underline{k_{coh}(\gamma_f)g(\eta)P^{m,a}}\end{aligned} \tag{8.5}$$

$$\begin{aligned}\frac{\partial P^{b,a}}{\partial t} &= \underline{k_{coh}(\gamma_f)g(\eta)P^{m,a}} - k_{adh}(\mathbf{x})(P_{max} - P^{se,a})P^{b,a} \\ &+ \underline{k_{act}^{b,adp} A_{e_2}(e_2)P^{b,adp} + k_{act}^{b,u} A_{e_2}(e_2)P^{b,u}}\end{aligned} \tag{8.6}$$

$$\begin{aligned}\frac{\partial P^{se,a}}{\partial t} &= k_{adh}(\mathbf{x})(P_{max} - P^{se,a})(P^{m,a} + P^{m,u} + P^{b,a}) \\ &+ \underline{k_{adh}^{(2)}(\mathbf{x})(P_{max} - P^{se,a})P^{b,u} + k_{adh}^{(3)}(\mathbf{x})(P_{max} - P^{se,a})P^{m,adp}} \\ &+ \underline{k_{adh}^{(4)}(\mathbf{x})(P_{max} - P^{se,a})P^{b,adp}}.\end{aligned} \tag{8.7}$$

ADP is released in a time-dependent manner; after each quarter of a second, the number of new bound platelets in a specific location is calculated and used to figure out how much ADP will be released at that same location over the next five seconds. In the LF model, this number is figured as follows:

$$P^{b,new} = P^{b,new} + P^{se,a} + P^{b,a} - P^{b,old}. \tag{8.8}$$

In this current version, we will use:

$$P^{b,new} = P^{b,new} + P^{se,a} + P^{b,a} + P^{b,adp} - P^{b,old}. \tag{8.9}$$

The new bound platelet fraction, total platelet fraction are:

$$\phi^B = \frac{P^{b,a} + P^{se,a} + P^{b,u} + P^{b,adp}}{P_{max}} \tag{8.10}$$

$$\phi^T = \frac{P^{b,a} + P^{se,a} + P^{b,u} + P^{m,a} + P^{m,u} + P^{m,adp} + P^{b,adp}}{P_{max}}. \tag{8.11}$$

The new equation for the virtual substance, $\eta$, is:

$$\frac{\partial \eta}{\partial t} = D_\eta \Delta \eta - \gamma \eta + \gamma \frac{(P^{b,a} + P^{se,a} + P^{b,u} + P^{b,adp})}{P_{max}}. \tag{8.12}$$

We ran a few simulations in which the cohesion and detachment functions, $k^{(2)}_{coh}(\gamma_f)$ and $k^{(2)}_{det}(\gamma_f)$, were left as constants, but were assigned different values than the cohesion rates for the mobile activated species. We found that the cohesion rate for the unactivated platelets had to be at least 100-fold smaller than that used for the mobile activated platelets in the LF model. If this cohesion rate was larger than this, a thrombus would form, radiating from the upstream edge, and quickly grow upstream and into the lumen mostly occluding the vessel. We would like to do some systematic testing of these rates to better understand how they each affect the model's results. For simplicity, we can test cohesion rates as functions of shear rate using the LF model's setup, but just modify the single cohesion term.

## 8.2 A Simpler Model for Shear Rate-Dependent Cohesion

The constitutive equation for an incompressible Newtonian fluid is given by:

$$\sigma = -p\mathbf{I} + 2\mu\mathbf{E} \tag{8.13}$$

where $\sigma$ is the stress tensor, $p$ is the hydrostatic pressure, $\mu$ is the dynamic viscosity and $\mathbf{E}$ is the rate of deformation tensor. If we let the velocity $\mathbf{u} = (u, v)$, then the rate of deformation tensor is given by:

$$\mathbf{E} = \begin{bmatrix} \sigma_{11} & \sigma_{12} \\ \sigma_{21} & \sigma_{22} \end{bmatrix} = \begin{bmatrix} \frac{\partial u}{\partial x} & \frac{1}{2}\left(\frac{\partial v}{\partial x} + \frac{\partial u}{\partial y}\right) \\ \frac{1}{2}\left(\frac{\partial v}{\partial x} + \frac{\partial u}{\partial y}\right) & \frac{\partial v}{\partial y} \end{bmatrix}$$

The viscous stress is proportional to the rate-of-deformation tensor. Using the fact that the fluid is incompressible the eigenvalues are:

$$\lambda_\pm = \pm\sqrt{\sigma_{12}^2 - \sigma_{11}\sigma_{22}} = \pm\sqrt{\sigma_{12}^2 + \sigma_{11}^2}$$

We use the positive eigenvalue of the rate of deformation tensor as the independent variable for the function, that will represent the cohesion of mobile activated platelets. We denote

this function $W_{coh} = W_{coh}(2\mu\lambda_+)$ where $\mu$ is the dynamic viscosity of the fluid. Figure 8.1 shows four different functions that we tried to specify the way the cohesion rate depends on the shear stress within the fluid. The first two curves, $W^1$ and $W^2$ represent a cohesion rate that is constant with the same value as used in the LF model until $2\mu\lambda = 20$ and 25, respectively, and then drops to zero. For the curve $W^3$, we assume that this drop occurs at a higher shear of 30, and that the shear rate is zero for lower levels of shear and gradually increases. Finally, $W^4$ also represents the idea that at low shear there is no cohesion, but at a medium level of shear, the cohesion becomes 10-fold higher than that used in the LF model.

The thrombi that develop using these choices for the cohesion rates in the model are shown in Figure 8.2. The left and right columns show the concentration of bound platelets after 600 and 1200 seconds of clotting activity, respectively. From this figure, we observe that the thrombi do not have as much upstream growth when the cohesion function is zero up to some level of shear. We can also see that each thrombus has a flat region on its top (luminal) side which was not seen in any of the other simulations described in this dissertation. Finally, there seems to be a relationship between the overall size and density of the thrombus and the level of shear at which the cohesion function is dropped to zero. It appears that as this level of shear is increased, the overall size of the thrombus is smaller but the density is increased (see Figure 8.2 and read from top to bottom). While these preliminary results are interesting, we must do further studies to understand or make

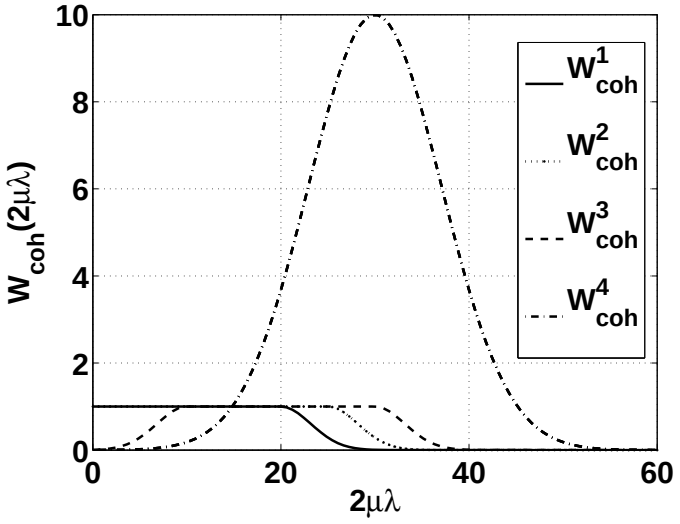


**Figure 8.1**. Four different relationships for cohesion and shear.

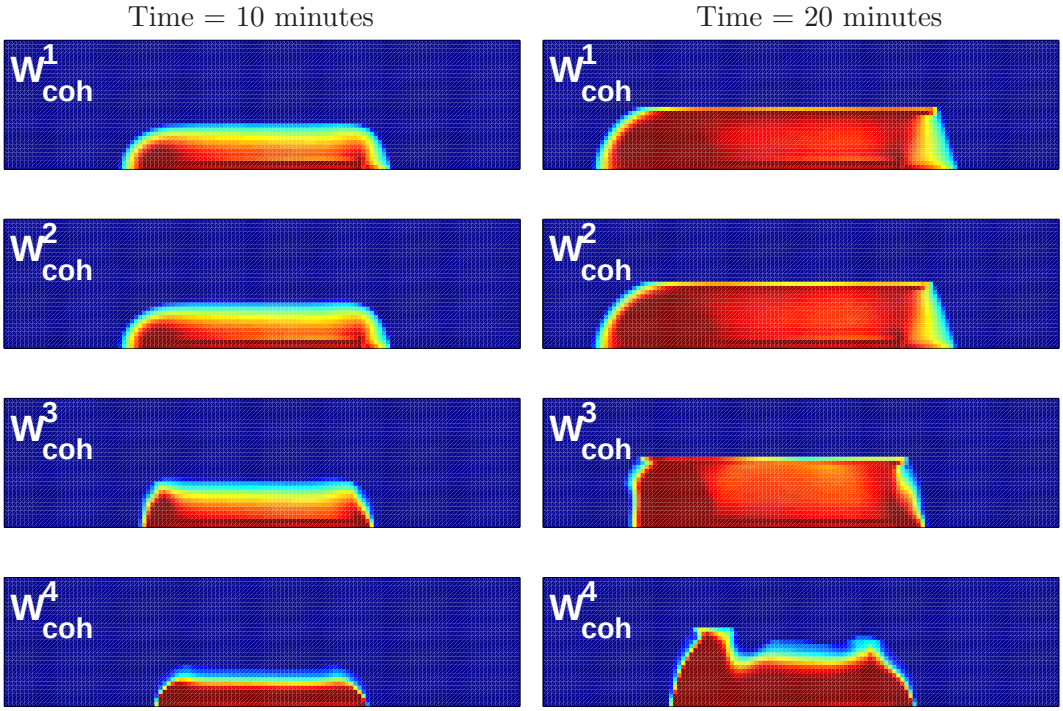


**Figure 8.2**. Spatial concentration of bound platelets after 600 (left) and 1200 (right) seconds of clotting activity using shear dependent cohesion rates.

conclusions about the complex connection between rate of cohesion and thrombus growth.

## 8.3 Platelet-Density-Dependent Diffusion

As previously mentioned, the experimental studies conducted at the Nemerson lab found that there was physical impedance on FXa transport imposed by platelets [26]. Although these experiments were done on thrombi that has be forming for hours (much longer than any of our simulations), we thought it would be interesting to try to capture some of this behavior using the LF model but including platelet-density-dependent diffusion.

As a first attempt, we make a modification to the diffusion coefficient (already set up to be spatially dependent) in the LF model. We use a similar function to that used for the platelet-density-dependent advection. We do not want the diffusion to be completely hindered, so we modify the function $W(\phi^T)$ to drop to a finite level rather than to zero. Figure 8.3 shows the new functions $D_2(\phi^T)$ and $D_3(\phi^T)$ that drop to 0.1 and 0.01, respectively, representing a 10-fold and 100-fold drop in the diffusion coefficient when the total platelet fraction is at its maximum. We assume that $D_1$ is the constant diffusion coefficient as used in the LF model.

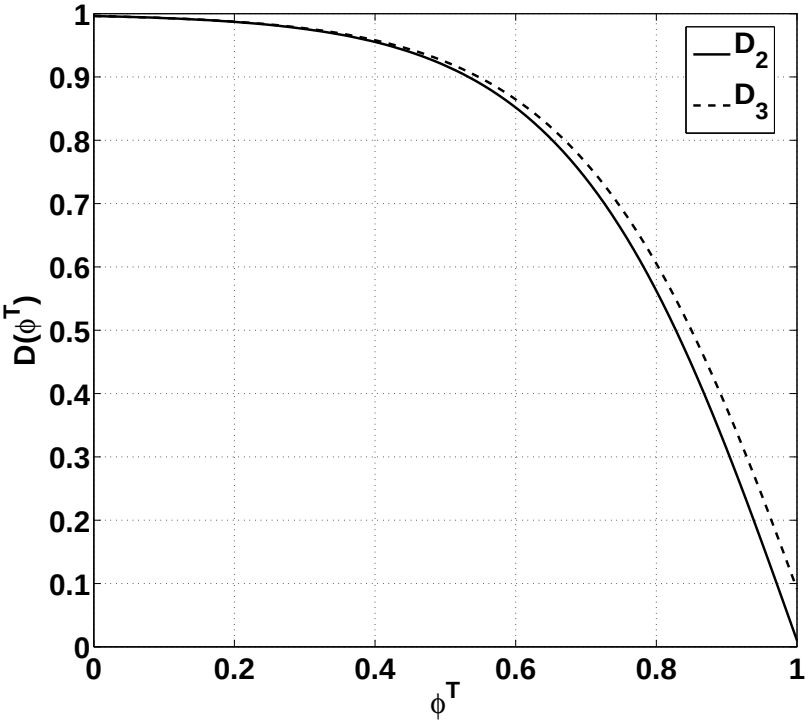


**Figure 8.3**. The diffusion coefficient as a function of total platelet function.

Using these choices for the diffusion coefficients in the model, we obtain the thrombi shown in Figure 8.4. The figure shows the concentration of bound platelets after 1120 seconds of clotting activity. From this figure, we observe that the thrombi do not have as much upstream growth when the diffusion coefficient is hindered by the total platelet fraction. It appears that for a smaller diffusion coefficient, the overall size of the thrombus is smaller but primarily at the upstream end of the clot, and the density is relatively unchanged. We hypothesize that since the upstream edge is the densest area of the clot, the thrombin and ADP that are produced in that area can no longer diffuse out and upstream of the growing thrombi to activate platelets before they actually reach the injury site. While these preliminary results are also interesting, we want to do more studies to fully understand and make conclusions about the relationship between hindered diffusion of chemical species and thrombus growth.

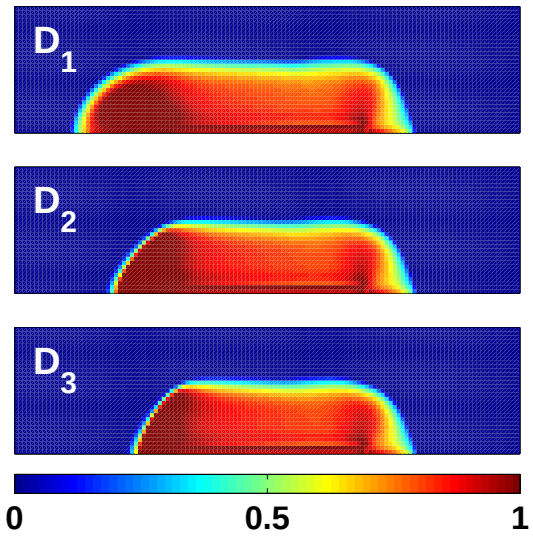


**Figure 8.4**. Spatial concentration of bound platelets after 1120 seconds of clotting activity using platelet-density-dependent diffusion.

# APPENDIX

# MODEL EQUATIONS AND PARAMETERS

$Z_i$ and $E_i$ refer to zymogen $i$ and enzyme $i$ in solution. Superscripts indicate membrane-bound versions of these proteins (e.g., $E_7^{se}$ refers to the TF:VIIa complex and $E_5^m$ refers to Factor Va bound to the platelet surface). Concentrations are denoted in a similar way but with lower-case $z$ and $e$. Concentrations of binding sites on bound platelets for prothrombin/thrombin, factors V/Va, X/Xa, VIII/VIIIa, and IX/IXa are denoted: $N_i^b P^{b,a} + N_i^s P^{se,a}$, where $N_2^b$, $N_5^b$, $N_{10}^b$, $N_8^b$, and $N_9^b$ refer to the number of binding sites for the zymogen-enzyme pairs expressed on the surface of a bound platelet (similar notation ${N_i}^s$ describes these quantities for a platelet bound directly to the subendothelium). A complex of $Z_i$ and $E_j$ is denoted $Z_i : E_j$ and its concentration is denoted $[Z_i : E_j]$. Special symbols are used for the platelet-bound 'tenase' VIIIa:IXa and 'prothrombinase' Va:Xa complexes, $TEN$ = VIIIa:IXa and $PRO$= Va:Xa, and $[TEN]$ and $[PRO]$ denote their respective concentrations. The special symbol $TFPIa$ is used for the fluid-phase complex TFPI:Xa, and $[TFPIa]$ denotes its concentration. The inhibitors are denoted $APC$ and $TFPI$ and their concentrations are denoted $[APC]$ and $[TFPI]$.

## A.1 Subendothelium-bound Chemicals

$$\begin{aligned}\frac{\partial z_7^{se}}{\partial t} &= k_7^{\text{on}} z_7([TF] - e_7^{setot} - z_7^{setot}) - k_7^{\text{off}} z_7^{se} - k^+_{z_7^{se}:e_{10}} z_7^{se} e_{10} \\ &\quad + k^-_{z_7^{se}:e_{10}}[Z_7^{se} : E_{10}] - k^+_{z_7^{se}:e_2} z_7^{se} e_2 + k^-_{z_7^{se}:e_2}[Z_7^{se} : E_2] \\ &\quad - k_{adh}(\mathbf{x}) z_7^{se}(P^{m,a} + P^{m,u} + P^{b,a})\end{aligned} \tag{A.1}$$

$$\begin{aligned}\frac{\partial e_7^{se}}{\partial t} &= k_7^{\text{on}} e_7([TF] - e_7^{setot} - z_7^{setot}) - k_7^{\text{off}} e_7^{se} \\ &+k^{\text{cat}}_{z_7^{se}:e_{10}}[Z_7^{se} : E_{10}] + k^{\text{cat}}_{z_7^{se}:e_2}[Z_7^{se} : E_2] \\ &+(k^{-}_{z_{10}:e_7^{se}} + k^{\text{cat}}_{z_{10}:e_7^{se}})[Z_{10} : E_7^{se}] - k^{+}_{z_{10}:e_7^{se}} z_{10} e_7^{se} \\ &+(k^{-}_{z_9:e_7^{se}} + k^{\text{cat}}_{z_9:e_7^{se}})[Z_9 : E_7^{se}] - k^{+}_{z_9:e_7^{se}} z_9 e_7^{se} \\ &-k^{+}_{tfpia:e_7^{se}}[TFPIa] e_7^{se} + k^{-}_{tfpia:e_7^{se}}[TFPIa : E_7^{se}] \\ &-k_{adh}(\mathbf{x}) e_7^{se}(P^{m,a} + P^{m,u} + P^{b,a})\end{aligned} \tag{A.2}$$

$$\begin{aligned}\frac{\partial [Z_7^{se} : E_2]}{\partial t} &= k^{+}_{z_7^{se}:e_2} z_7^{se} e_2 - (k^{-}_{z_7^{se}:e_2} + k^{\text{cat}}_{z_7^{se}:e_2})[Z_7^{se} : E_2] \\ &-k_{adh}(\mathbf{x})[Z_7^{se} : E_2](P^{m,a} + P^{m,u} + P^{b,a})\end{aligned} \tag{A.3}$$

$$\begin{aligned}\frac{\partial [Z_7^{se} : E_{10}]}{\partial t} &= k^{+}_{z_7^{se}:e_{10}} z_7^{se} e_{10} - (k^{-}_{z_7^{se}:e_{10}} + k^{\text{cat}}_{z_7^{se}:e_{10}})[Z_7^{se} : E_{10}] \\ &-k_{adh}(\mathbf{x})[Z_7^{se} : E_{10}](P^{m,a} + P^{m,u} + P^{b,a})\end{aligned} \tag{A.4}$$

$$\begin{aligned}\frac{\partial [Z_9 : E_7^{se}]}{\partial t} &= k^{+}_{z_9:e_7^{se}} z_9 e_7^{se} - (k^{-}_{z_9:e_7^{se}} + k^{\text{cat}}_{z_9:e_7^{se}})[Z_9 : E_7^{se}] \\ &-k_{adh}(\mathbf{x})[Z_9 : E_7^{se}](P^{m,a} + P^{m,u} + P^{b,a})\end{aligned} \tag{A.5}$$

$$\begin{aligned}\frac{\partial [Z_{10} : E_7^{se}]}{\partial t} &= k^{+}_{z_{10}:e_7^{se}} z_{10} e_7^{se} - (k^{-}_{z_{10}:e_7^{se}} + k^{\text{cat}}_{z_{10}:e_7^{se}})[Z_{10} : E_7^{se}] \\ &-k_{adh}(\mathbf{x})[Z_{10} : E_7^{se}](P^{m,a} + P^{m,u} + P^{b,a})\end{aligned} \tag{A.6}$$

$$\begin{aligned}\frac{\partial [TFPIa : E_7^{se}]}{\partial t} &= -k^{-}_{tfpia:e_7^{se}}[TFPIa : E_7^{se}] + k^{+}_{tfpia:e_7^{se}}[TFPIa] e_7^{se} \\ &-k_{adh}(\mathbf{x})[TFPIa : E_7^{se}](P^{m,a} + P^{m,u} + P^{b,a})\end{aligned} \tag{A.7}$$

$$\frac{\partial [TF]}{\partial t} = -k_{adh}(\mathbf{x})[TF](P^{m,a} + P^{m,u} + P^{b,a}) \tag{A.8}$$

## A.2 Platelet-bound Chemicals

$$\begin{aligned}\frac{\partial z_2^m}{\partial t} &= k_2^{\text{on}} z_2 (N_2^b P^{b,a} + N_2^{se} P^{se,a} - z_2^{mtot} - e_2^{mtot}) - k_2^{\text{off}} z_2^m \\ &\quad - k^+_{z_2^m:pro} z_2^m [PRO] + k^-_{z_2^m:pro} [Z_2^m : PRO]\end{aligned} \tag{A.9}$$

$$\begin{aligned}\frac{\partial e_2^m}{\partial t} &= k_2^{\text{on}} e_2 (N_2^b P^{b,a} + N_2^{se} P^{se,a} - z_2^{mtot} - e_2^{mtot}) \\ &\quad - k_2^{\text{off}} e_2^m + k^{\text{cat}}_{z_2^m:pro} [Z_2^m : PRO] \\ &\quad + (k^{\text{cat}}_{z_5^m:e_2^m} + k^-_{z_5^m:e_2^m}) [Z_5^m : E_2^m] - k^+_{z_5^m:e_2^m} z_5^m e_2^m \\ &\quad + (k^{\text{cat}}_{z_8^m:e_2^m} + k^-_{z_8^m:e_2^m}) [Z_8^m : E_2^m] - k^+_{z_8^m:e_2^m} z_8^m e_2^m\end{aligned} \tag{A.10}$$

$$\begin{aligned}\frac{\partial z_5^m}{\partial t} &= k_5^{\text{on}} z_5 (N_5^b P^{b,a} + N_5^{se} P^{se,a} - z_5^{mtot} - e_5^{mtot}) - k_5^{\text{off}} z_5^m \\ &\quad - k^+_{z_5^m:e_{10}^m} z_5^m e_{10}^m + k^-_{z_5^m:e_{10}^m} [Z_5^m : E_{10}^m] \\ &\quad - k^+_{z_5^m:e_2^m} z_5^m e_2^m + k^-_{z_5^m:e_2^m} [Z_5^m : E_2^m]\end{aligned} \tag{A.11}$$

$$\begin{aligned}\frac{\partial e_5^m}{\partial t} &= k_5^{\text{on}} e_5 (N_5^b P^{b,a} + N_5^{se} P^{se,a} - z_5^{mtot} - e_5^{mtot}) - k_5^{\text{off}} e_5^m \\ &\quad + k^{\text{cat}}_{z_5^m:e_{10}^m} [Z_5^m : E_{10}^m] + k^{\text{cat}}_{z_5^m:e_2^m} [Z_5^m : E_2^m] + k^-_{\text{pro}} [PRO] \\ &\quad - k^+_{\text{pro}} e_5^m e_{10}^m - k^+_{apc:e_5^m} [APC] e_5^m + k^-_{apc:e_5^m} [APC : E_5^m]\end{aligned} \tag{A.12}$$

$$\begin{aligned}\frac{\partial z_8^m}{\partial t} &= k_8^{\text{on}} z_8 (N_8^b P^{b,a} + N_8^{se} P^{se,a} - z_8^{mtot} - e_8^{mtot}) - k_8^{\text{off}} z_8^m \\ &\quad - k^+_{z_8^m:e_{10}^m} z_8^m e_{10}^m + k^-_{z_8^m:e_{10}^m} [Z_8^m : E_{10}^m] \\ &\quad - k^+_{z_8^m:e_2^m} z_8^m e_2^m + k^-_{z_8^m:e_2^m} [Z_8^m : E_2^m]\end{aligned} \tag{A.13}$$

$$\begin{aligned}\frac{\partial e_8^m}{\partial t} &= k_8^{\text{on}} e_8 (N_8^b P^{b,a} + N_8^{se} P^{se,a} - z_8^{mtot} - e_8^{mtot}) - k_8^{\text{off}} e_8^m \\ &\quad + k^{\text{cat}}_{z_8^m:e_{10}^m} [Z_8^m : E_{10}^m] + k^{\text{cat}}_{z_8^m:e_2^m} [Z_8^m : E_2^m] + k^-_{\text{ten}} [TEN] \\ &\quad - k^+_{\text{ten}} e_8^m e_9^m - k^+_{apc:e_8^m} [APC] e_8^m + k^-_{apc:e_8^m} [APC : E_8^m]\end{aligned} \tag{A.14}$$

$$\frac{\partial z_9^m}{\partial t} = k_9^{\text{on}} z_9 (N_9^b P^{b,a} + N_9^{se} P^{se,a} - z_9^{mtot} - e_9^{mtot}) - k_9^{\text{off}} z_9^m \tag{A.15}$$

$$\frac{\partial e_9^m}{\partial t} = k_9^{\text{on}} e_9 (N_9^b P^{b,a} + N_9^{se} P^{se,a} - z_9^{m\,tot} - e_9^{m\,tot}) - k_9^{\text{off}} e_9^m \quad (A.16)$$
$$+k_{\text{ten}}^- [TEN] - k_{\text{ten}}^+ e_8^m e_9^m$$

$$\frac{\partial z_{10}^m}{\partial t} = k_{10}^{\text{on}} z_{10} (N_{10}^b P^{b,a} + N_{10}^{se} P^{se,a} - e_{10}^{m\,tot} - z_{10}^{m\,tot}) - k_{10}^{\text{off}} z_{10}^m \quad (A.17)$$
$$+k_{z_{10}^m:ten}^- [Z_{10}^m : TEN] - k_{z_{10}^m:ten}^+ z_{10}^m [TEN]$$
$$+k_{z_{10}^m:ten}^- [Z_{10}^m : TEN^*] - k_{z_{10}^m:ten}^+ z_{10}^m [TEN^*]$$

$$\frac{\partial e_{10}^m}{\partial t} = k_{10}^{\text{on}} e_{10} (N_{10}^b P^{b,a} + N_{10}^{se} P^{se,a} - e_{10}^{m\,tot} - z_{10}^{m\,tot}) - k_{10}^{\text{off}} e_{10}^m \quad (A.18)$$
$$+(k_{z_5^m:e_{10}^m}^- + k_{z_5^m:e_{10}^m}^{\text{cat}})[Z_5^m : E_{10}^m] - k_{z_5^m:e_{10}^m}^+ z_5^m e_{10}^m$$
$$+(k_{z_8^m:e_{10}^m}^- + k_{z_8^m:e_{10}^m}^{\text{cat}})[Z_8^m : E_{10}^m] - k_{z_8^m:e_{10}^m}^+ z_8^m e_{10}^m$$
$$+k_{\text{pro}}^- [PRO] - k_{\text{pro}}^+ e_5^m e_{10}^m + k_{z_{10}^m:ten}^{\text{cat}} [Z_{10}^m : TEN]$$
$$+k_{z_{10}^m:ten}^{\text{cat}} [Z_{10}^m : TEN^*]$$

$$\frac{\partial [TEN]}{\partial t} = k_{\text{ten}}^+ e_8^m e_9^m - k_{\text{ten}}^- [TEN] - k_{z_{10}^m:ten}^+ z_{10}^m [TEN] \quad (A.19)$$
$$+(k_{z_{10}^m:ten}^{\text{cat}} + k_{z_{10}^m:ten}^-)[Z_{10}^m : TEN]$$

$$\frac{\partial [PRO]}{\partial t} = k_{\text{pro}}^+ e_5^m e_{10}^m - k_{\text{pro}}^- [PRO] - k_{z_2^m:pro}^+ z_2^m [PRO] \quad (A.20)$$
$$+(k_{z_2^m:pro}^{\text{cat}} + k_{z_2^m:pro}^-)[Z_2^m : PRO]$$

$$\frac{\partial [Z_2^m : PRO]}{\partial t} = k_{z_2^m:pro}^+ z_2^m [PRO] - (k_{z_2^m:pro}^- + k_{z_2^m:pro}^{\text{cat}})[Z_2^m : PRO] \quad (A.21)$$

$$\frac{\partial [Z_5^m : E_2^m]}{\partial t} = k_{z_5^m:e_2^m}^+ z_5^m e_2^m - (k_{z_5^m:e_2^m}^- + k_{z_5^m:e_2^m}^{\text{cat}})[Z_5^m : E_2^m] \quad (A.22)$$

$$\frac{\partial [Z_5^m : E_{10}^m]}{\partial t} = k_{z_5^m:e_{10}^m}^+ z_5^m e_{10}^m - (k_{z_5^m:e_{10}^m}^- + k_{z_5^m:e_{10}^m}^{\text{cat}})[Z_5^m : E_{10}^m] \quad (A.23)$$

$$\frac{\partial [Z_8^m : E_2^m]}{\partial t} = k_{z_8^m:e_2^m}^+ z_8^m e_2^m - (k_{z_8^m:e_2^m}^- + k_{z_8^m:e_2^m}^{\text{cat}})[Z_8^m : E_2^m] \quad (A.24)$$

$$\frac{\partial [Z_8^m : E_{10}^m]}{\partial t} = k_{z_8^m:e_{10}^m}^+ z_8^m e_{10}^m - (k_{z_8^m:e_{10}^m}^- + k_{z_8^m:e_{10}^m}^{\text{cat}})[Z_8^m : E_{10}^m] \quad (A.25)$$

$$\frac{\partial[Z_{10}^m : TEN]}{\partial t} = k^+_{z_{10}^m:ten} z_{10}^m [TEN] - (k^-_{z_{10}^m:ten} + k^{\text{cat}}_{z_{10}^m:ten})[Z_{10}^m : TEN] \quad \text{(A.26)}$$

$$\frac{\partial[APC : E_5^m]}{\partial t} = k^+_{apc:e_5^m} [APC] e_5^m - (k^-_{apc:e_5^m} + k^{\text{cat}}_{apc:e_5^m})[APC : E_5^m] \quad \text{(A.27)}$$

$$\frac{\partial[APC : E_8^m]}{\partial t} = k^+_{apc:e_8^m} [APC] e_8^m - (k^-_{apc:e_8^m} + k^{\text{cat}}_{apc:e_8^m})[APC : E_8^m] \quad \text{(A.28)}$$

$$\begin{aligned} \frac{\partial e_9^{m,*}}{\partial t} = {} & k_9^{on} e_9^m (N_{9*}^b P^{b,a} + N_{9*}^{se} P^{se,a} - e_9^{m,*} \\ & -[TEN^*] - [Z_{10}^m : TEN^*]) - k_9^{off} e_9^{m,*} \\ & + k^-_{ten}[TEN^*] - k^+_{ten} e_8^m e_9^{m,*} \end{aligned} \quad \text{(A.29)}$$

$$\begin{aligned} \frac{\partial[TEN^*]}{\partial t} = {} & k^+_{ten} e_8^m e_9^{m,*} - k^-_{ten}[TEN^*] - k^+_{z_{10}^m:ten} z_{10}^m [TEN^*] \\ & + (k^-_{z_{10}^m:ten} + k^{\text{cat}}_{z_{10}^m:ten})[Z_{10}^m : TEN^*] \end{aligned} \quad \text{(A.30)}$$

$$\begin{aligned} \frac{\partial[Z_{10}^m : TEN^*]}{\partial t} = {} & k^+_{z_{10}^m:ten} z_{10}^m [TEN^*] \\ & - (k^-_{z_{10}^m:ten} + k^{\text{cat}}_{z_{10}^m:ten})[Z_{10}^m : TEN^*] \end{aligned} \quad \text{(A.31)}$$

## A.3 Fluid-phase Chemicals

$$\begin{aligned} \frac{\partial z_2}{\partial t} = {} & -\nabla \cdot (\mathbf{u} z_2 - D \nabla z_2) \\ & - k_2^{\text{on}} z_2 (N_2^b P^{b,a} + N_2^{se} P^{se,a} - z_2^{mtot} - e_2^{mtot}) + k_2^{\text{off}} z_2^m \end{aligned} \quad \text{(A.32)}$$

$$\begin{aligned} \frac{\partial e_2}{\partial t} = {} & -\nabla \cdot (\mathbf{u} e_2 - D \nabla e_2) \\ & - k_2^{\text{on}} e_2 (N_2^b P^{b,a} + N_2^{se} P^{se,a} - z_2^{mtot} - e_2^{mtot}) + k_2^{\text{off}} e_2^m \\ & + (k^{\text{cat}}_{z_5:e_2} + k^-_{z_5:e_2})[Z_5 : E_2] - k^+_{z_5:e_2} z_5 e_2 \\ & + (k^-_{z_7:e_2} + k^{\text{cat}}_{z_7:e_2})[Z_7 : E_2] - k^+_{z_7:e_2} z_7 e_2 \\ & + (k^{\text{cat}}_{z_8:e_2} + k^-_{z_8:e_2})[Z_8 : E_2] - k^+_{z_8:e_2} z_8 e_2 - k_2^{\text{in}} e_2 \end{aligned} \quad \text{(A.33)}$$

$$\frac{\partial z_5}{\partial t} = -\nabla\cdot(\mathbf{u}z_5 - D\nabla z_5) - k_5^{\text{on}} z_5(N_5^b P^{b,a} + N_5^{se} P^{se,a} - z_5^{mtot} - e_5^{mtot}) \quad \text{(A.34)}$$
$$+k_5^{\text{off}} z_5^m - k^+_{z_5:e_2} z_5 e_2 + k^-_{z_5:e_2}[Z_5 : E_2] + N_5 \frac{\partial(P^{b,a} + P^{se,a})}{\partial t}$$

$$\frac{\partial e_5}{\partial t} = -\nabla\cdot(\mathbf{u}e_5 - D\nabla e_5) - k_5^{\text{on}} e_5(N_5^b P^{b,a} + N_5^{se} P^{se,a} - z_5^{mtot} - e_5^{mtot}) \quad \text{(A.35)}$$
$$+k_5^{\text{off}} e_5^m + k^{\text{cat}}_{z_5:e_2}[Z_5 : E_2]$$

$$\frac{\partial z_7}{\partial t} = -\nabla\cdot(\mathbf{u}z_7 - D\nabla z_7) - k^+_{z_7:e_{10}} z_7 e_{10} + k^-_{z_7:e_{10}}[Z_7 : E_{10}] \quad \text{(A.36)}$$
$$+k^-_{z_7:e_2}[Z_7 : E_2] - k^+_{z_7:e_2} z_7 e_2$$

$$\frac{\partial e_7}{\partial t} = -\nabla\cdot(\mathbf{u}e_7 - D\nabla e_7) + k^{\text{cat}}_{z_7:e_{10}}[Z_7 : E_{10}] + k^{\text{cat}}_{z_7:e_2}[Z_7 : E_2] \quad \text{(A.37)}$$

$$\frac{\partial z_8}{\partial t} = -\nabla\cdot(\mathbf{u}z_8 - D\nabla z_8) - k_8^{\text{on}} z_8(N_8^b P^{b,a} + N_8^{se} P^{se,a} - z_8^{mtot} - e_8^{mtot}) \quad \text{(A.38)}$$
$$+k_8^{\text{off}} z_8^m - k^+_{z_8:e_2} z_8 e_2 + k^-_{z_8:e_2}[Z_8 : E_2]$$

$$\frac{\partial e_8}{\partial t} = -\nabla\cdot(\mathbf{u}e_8 - D\nabla e_8) \quad \text{(A.39)}$$
$$-k_8^{\text{on}} e_8(N_8^b P^{b,a} + N_8^{se} P^{se,a} - z_8^{mtot} - e_8^{mtot})$$
$$+k_8^{\text{off}} e_8^m + k^{\text{cat}}_{z_8:e_2}[Z_8 : E_2]$$

$$\frac{\partial z_9}{\partial t} = -\nabla\cdot(\mathbf{u}z_9 - D\nabla z_9) \quad \text{(A.40)}$$
$$-k_9^{\text{on}} z_9(N_9^b P^{b,a} + N_9^{se} P^{se,a} - z_9^{mtot} - e_9^{mtot}) + k_9^{\text{off}} z_9^m$$

$$\frac{\partial e_9}{\partial t} = -\nabla\cdot(\mathbf{u}e_9 - D\nabla e_9) \quad \text{(A.41)}$$
$$-k_9^{\text{on}} e_9(N_9^b P^{b,a} + N_9^{se} P^{se,a} - z_9^{mtot} - e_9^{mtot})$$
$$-k_9^{on} e_9^m(N_{9*}^b P^{b,a} + N_{9*}^{se} P^{se,a} - e_9^{m,*} - [TEN^*] - [Z_{10}^m : TEN^*])$$
$$-k_9^{\text{in}} e_9 + k_9^{\text{off}} e_9^m + k_9^{off} e_9^{m,*}$$

$$\frac{\partial z_{10}}{\partial t} = -\nabla \cdot (\mathbf{u} z_{10} - D\nabla z_{10}) \\ -k_{10}^{\text{on}} z_{10}(N_{10}^{b} P^{b,a} + N_{10}^{se} P^{se,a} - e_{10}^{m\,tot} - z_{10}^{m\,tot}) + k_{10}^{\text{off}} z_{10}^{m} \tag{A.42}$$

$$\frac{\partial e_{10}}{\partial t} = -\nabla \cdot (\mathbf{u} e_{10} - D\nabla e_{10}) \\ -k_{10}^{\text{on}} e_{10}(N_{10}^{b} P^{b,a} + N_{10}^{se} P^{se,a} - e_{10}^{m\,tot} - z_{10}^{m\,tot}) \\ +k_{10}^{\text{off}} e_{10}^{m} - k_{tfpia:e_{10}}^{+}[TFPI]e_{10} + k_{tfpia:e_{10}}^{-}[TFPIa] \\ +(k_{z_7:e_{10}}^{-} + k_{z_7:e_{10}}^{\text{cat}})[Z_7 : E_{10}] - k_{z_7:e_{10}}^{+} z_7 e_{10} - k_{10}^{\text{in}} e_{10} \tag{A.43}$$

$$\frac{\partial [Z_5 : E_2]}{\partial t} = -\nabla \cdot (\mathbf{u}[Z_5 : E_2] - D\nabla[Z_5 : E_2]) + k_{z_5:e_2}^{+} z_5 e_2 \\ -(k_{z_5:e_2}^{-} + k_{z_5:e_2}^{\text{cat}})[Z_5 : E_2] \tag{A.44}$$

$$\frac{\partial [Z_7 : E_2]}{\partial t} = -\nabla \cdot (\mathbf{u}[Z_7 : E_2] - D\nabla[Z_7 : E_2]) + k_{z_7:e_2}^{+} z_7 e_2 \\ -(k_{z_7:e_2}^{-} + k_{z_7:e_2}^{\text{cat}})[Z_7 : E_2] \tag{A.45}$$

$$\frac{\partial [Z_7 : E_{10}]}{\partial t} = -\nabla \cdot (\mathbf{u}[Z_7 : E_{10}] - D\nabla[Z_7 : E_{10}]) + k_{z_7:e_{10}}^{+} z_7 e_{10} \\ -(k_{z_7:e_{10}}^{-} + k_{z_7:e_{10}}^{\text{cat}})[Z_7 : E_{10}] \tag{A.46}$$

$$\frac{\partial [Z_8 : E_2]}{\partial t} = -\nabla \cdot (\mathbf{u}[Z_8 : E_2] - D\nabla[Z_8 : E_2]) + k_{z_8:e_2}^{+} z_8 e_2 \\ -(k_{z_8:e_2}^{-} + k_{z_8:e_2}^{\text{cat}})[Z_8 : E_2] \tag{A.47}$$

$$\frac{\partial [APC]}{\partial t} = -\nabla \cdot (\mathbf{u}[APC] - D\nabla[APC]) \\ +(k_{apc:e_5^m}^{-} + k_{apc:e_5^m}^{\text{cat}})[APC : E_5^m] - k_{apc:e_5^m}^{+}[APC]e_5^m \\ +(k_{apc:e_8^m}^{-} + k_{apc:e_8^m}^{\text{cat}})[APC : E_8^m] - k_{apc:e_8^m}^{+}[APC]e_8^m \tag{A.48}$$

$$\frac{\partial [TFPI]}{\partial t} = -\nabla \cdot (\mathbf{u}[TFPI] - D\nabla[TFPI]) \\ -k_{tfpia:e_{10}}^{+}[TFPI]e_{10} + k_{tfpia:e_{10}}^{-}[TFPIa] \tag{A.49}$$

$$\frac{\partial [TFPIa]}{\partial t} = -\nabla \cdot (\mathbf{u}[TFPIa] - D\nabla[TFPIa]) \\ -k_{tfpia:e_{10}}^{-}[TFPIa] + k_{tfpia:e_{10}}^{+}[TFPI]e_{10} \tag{A.50}$$

$$\frac{\partial [ADP]}{\partial t} = -\mathbf{u}\cdot\nabla[ADP] + \nabla\cdot(D[\nabla ADP]) + \sigma_{release} \quad \text{(A.51)}$$

## A.4 Subendothelium Boundary Conditions

$$-D\frac{\partial e_2}{\partial y} = -k^{+}_{z_7^{se}:e_2} z_7^{se} e_2 + (k^{-}_{z_7^{se}:e_2} + k^{\text{cat}}_{z_7^{se}:e_2})[Z_7^{se} : E_2] \quad \text{(A.52)}$$

$$-D\frac{\partial z_7}{\partial y} = -k_7^{on} z_7([TF] - z_7^{se,tot} - e_7^{se,tot}) + k_7^{off} z_7^{se} \quad \text{(A.53)}$$

$$-D\frac{\partial e_7}{\partial y} = -k_7^{on} e_7([TF] - z_7^{se,tot} - e_7^{se,tot}) + k_7^{off} e_7^{se} \quad \text{(A.54)}$$

$$-D\frac{\partial z_9}{\partial y} = -k^{+}_{z_9:e_7^{se}} z_9 e_7^{se} + k^{-}_{z_9:e_7^{se}}[Z_9 : E_7^{se}] \quad \text{(A.55)}$$

$$-D\frac{\partial e_9}{\partial y} = k^{\text{cat}}_{z_9:e_7^{se}}[Z_9 : E_7^{se}] \quad \text{(A.56)}$$

$$-D\frac{\partial z_{10}}{\partial y} = -k^{+}_{z_{10}:e_7^{se}} z_{10} e_7^{se} + k^{-}_{z_{10}:e_7^{se}}[Z_{10} : E_7^{se}] \quad \text{(A.57)}$$

$$-D\frac{\partial e_{10}}{\partial y} = -k^{+}_{z_7^{se}:e_{10}} e_{10} z_7^{se} + k^{\text{cat}}_{z_{10}:e_7^{se}}[Z_{10} : E_7^{se}] + (k^{-}_{z_7^{se}:e_{10}} + k^{\text{cat}}_{z_7^{se}:e_{10}})[Z_7^{se} : E_{10}] \quad \text{(A.58)}$$

$$-D\frac{\partial [TFPIa]}{\partial y} = -k^{+}_{tfpia:e_7^{se}}[TFPIa] e_7^{se} + k^{-}_{tfpia:e_7^{se}}[TFPIa : E_7^{se}] \quad \text{(A.59)}$$

## A.5 Kinetic and Physical Parameters

**Table A.1**. Diffusion coefficients for platelets and mobile chemical species. (a) From [72]. (b) From [24]. (c) From [80].

| | | |
|---|---|---|
| Platelets | $2.5\times10^{-7}$ cm$^2$/s | a |
| ADP | $5\times10^{-6}$ cm$^2$/s | b |
| All Other Chemical Species | $5\times10^{-7}$ cm$^2$/s | c |

**Table A.2**. Normal concentrations and surface binding site numbers. (a) From [47]. (b) From [45]. (c) [52] suggests that normal plasma concentration of fVIIa is about 1% of the normal fVII concentration. (d) From [56]. (e) From [76]. (f) From [10]. (g) From [75]. (h) From [54]. (i) From [2]. (j) From [46].

| | | |
|---|---|---|
| PROTHROMBIN | 1.4 $\mu$M | a |
| FACTOR V | 0.01 $\mu$M | b |
| FACTOR VII | 0.01 $\mu$M | a |
| FACTOR VIIa | 0.1 nM | c |
| FACTOR VIII | 1.0 nM | a |
| FACTOR IX | 0.09 $\mu$M | a |
| FACTOR X | 0.17 $\mu$M | a |
| TFPI | 2.5 nM | d |
| PLATELETS, $P_0$ | $2.5(10)^5/\text{mm}^3$ | e |
| $N_2^b, N_2^{se}$ | 2000 | f |
| $N_5^b, N_5^{se}$ | 3000 | g |
| $N_8^b, N_8^{se}$ | 450 | h |
| $N_9^b, N_9^{se}$ | 500 | i |
| $N_{10}^b, N_{10}^{se}$ | 2700 | j |

**Table A.3**. Reactions of subendothelium. (a) $k^{\text{cat}}_{z_7^{se}:e_{10}} = 5.0$ sec$^{-1}$ and $K_M = 1.2 \cdot 10^{-6}$ M [13]. (b) $k^{\text{cat}}_{z_7^{se}:e_2} = 6.1 \cdot 10^{-2}$ sec$^{-1}$ and $K_M = 2.7 \cdot 10^{-6}$ M [13]. (d) $k^{\text{cat}}_{z_{10}:e_7^{se}} = 1.15$ sec$^{-1}$ and $K_M = 4.5 \cdot 10^{-7}$ M [47]. (d) We assume that the reaction constants for TF:VIIa activation of fIX are the same as for TF:VIIa activation of fX. (e) $K_d = 1.0 \cdot 10^{-10}$ M [53].

| Reaction | Reactants | Complex | Product | $\text{M}^{-1}\text{sec}^{-1}$ | $\text{sec}^{-1}$ | $\text{sec}^{-1}$ | Note |
|---|---|---|---|---|---|---|---|
| Activation (of-,by-) | | | | | | | |
| (TF:VII,Xa) | $E_{10}$, $Z_7^{se}$ | $Z_7^{se} : E_{10}$ | $E_7^{se}$ | $k^+_{z_7^{se}:e_{10}}$=$5.0 \cdot 10^6$ | $k^-_{z_7^{se}:e_{10}}$=1.0 | $k^{\text{cat}}_{z_7^{se}:e_{10}}$=5.0 | a |
| (TF:VII,IIa) | $E_2$, $Z_7^{se}$ | $Z_7^{se} : E_2$ | $E_7^{se}$ | $k^+_{z_7^{se}:e_2}$=$3.92 \cdot 10^5$ | $k^-_{z_7^{se}:e_2}$=1.0 | $k^{\text{cat}}_{z_7^{se}:e_2}$=$6.1 \cdot 10^{-2}$ | b |
| (X,TF:VIIa) | $E_7^{se}$, $Z_{10}$ | $Z_{10} : E_7^{se}$ | $E_{10}$ | $k^+_{z_{10}:e_7^{se}}$=$8.95 \cdot 10^6$ | $k^-_{z_{10}:e_7^{se}}$=1.0 | $k^{\text{cat}}_{z_{10}:e_7^{se}}$=1.15 | c |
| (IX,TF:VIIa) | $E_7^{se}$, $Z_9$ | $Z_9 : E_7^{se}$ | $E_9$ | $k^+_{z_9:e_7^{se}}$=$8.95 \cdot 10^6$ | $k^-_{z_9:e_7^{se}}$=1.0 | $k^{\text{cat}}_{z_9:e_7^{se}}$=1.15 | d |
| Binding (-,with -) | | | | | | | |
| (VII,TF) | $Z_7$, $TF$ | | $Z_7^{se}$ | $k_7^{\text{on}}$=$5.0 \cdot 10^7$ | $k_7^{\text{off}}$=$5.0 \cdot 10^{-3}$ | | e |
| (VIIa,TF) | $E_7$, $TF$ | | $E_7^{se}$ | $k_7^{\text{on}}$=$5.0 \cdot 10^7$ | $k_7^{\text{off}}$=$5.0 \cdot 10^{-3}$ | | e |

**Table A.4**. Reactions in the plasma. (a) $k^{\text{cat}}_{z_7:e_{10}} = 5.0$ sec$^{-1}$ and $K_M = 1.2 \cdot 10^{-6}$ M [13]. (b) $k^{\text{cat}}_{z_7:e_2} = 6.1 \cdot 10^{-2}$ sec$^{-1}$ and $K_M = 2.7 \cdot 10^{-6}$ M [13] (c) $k^{\text{cat}}_{z_5:e_2} = 0.23$ sec$^{-1}$ and $K_M = 7.17 \cdot 10^{-8}$ M [49]. (d) $k^{\text{cat}}_{z_8:e_2} = 0.9$ sec$^{-1}$ [28] and $K_M = 2 \cdot 10^{-7}$ M [42].

| Reaction | Reactants | Complex | Product | $M^{-1}sec^{-1}$ | $sec^{-1}$ | $sec^{-1}$ | Note |
|---|---|---|---|---|---|---|---|
| Activation (of-,by-) | | | | | | | |
| (VII,Xa) | $Z_7$, $E_{10}$ | $Z_7 : E_{10}$ | $E_7$ | $k^+_{z_7:e_{10}}$=5 $\cdot 10^6$ | $k^-_{z_7:e_{10}}$=1.0 | $k^{\text{cat}}_{z_7:e_{10}}$=5.0 | a |
| (VII,IIa) | $Z_7$, $E_2$ | $Z_7 : E_2$ | $E_7$ | $k^+_{z_7:e_2}$=3.92 $\cdot 10^5$ | $k^-_{z_7:e_2}$=1.0 | $k^{\text{cat}}_{z_7:e_2}$=6.1 $\cdot 10^{-2}$ | b |
| (V,IIa) | $Z_5$, $E_2$ | $Z_5 : E_2$ | $E_5$ | $k^+_{z_5:e_2}$= $1.73 \cdot 10^7$ | $k^-_{z_5:e_2}$=1.0 | $k^{\text{cat}}_{z_5:e_2}$=0.23 | c |
| (VIII,IIa) | $Z_8$, $E_2$ | $Z_8 : E_2$ | $E_8$ | $k^+_{z_8:e_2}$=$2.64 \cdot 10^7$ | $k^-_{z_8:e_2}$=1.0 | $k^{\text{cat}}_{z_8:e_2}$=0.9 | d |

**Table A.5**. Binding to platelet surfaces. (a) For fIX binding to platelets, $K_d = 2.5 \cdot 10^{-9}$ M [2], and for fX binding to platelets, $K_d$ has approximately the same value [75]. For fX binding to PCPS vesicles, the on-rate is about $10^7$ $M^{-1}sec^{-1}$ and the off-rate is about 1.0 $sec^{-1}$ [37] giving a dissociation constant of about $10^{-7}$ M. To estimate on- and off-rates for the higher-affinity binding of fX to platelets, we keep the on-rate the same as for vesicles and adjust the off-rate to give the correct dissociation constant. The rates for fIX binding with platelets are taken to be the same as for fX binding. (b) We assume binding constants for fIXa binding to the specific fIXa binding sites are the same as for shared sites. (c) fV binds with high-affinity to phospholipids (PCPS) [37] and we use the same rate constants reported there to describe fV binding to platelets. (d) The $K_d$ for fVIII binding with platelets is taken from [54]. We set the off-rate $k_8^{\text{off}}$ for fVIII binding to platelets equal to that for fV binding to platelets, and calculate the on-rate $k_8^{\text{on}}$. (e) For prothrombin interactions with platelets, $K_d$ is reported to be $5.9 \cdot 10^{-7}$ M [44]. We choose $k_2^{\text{off}}$ and set $k_2^{\text{on}} = k_2^{\text{off}}/K_d$.

| Reaction | Reactants | Products | $M^{-1}sec^{-1}$ | $sec^{-1}$ | Note |
|---|---|---|---|---|---|
| | | | | | |
| Factors IX | $Z_9$, $P_9$ | $Z_9^m$ | $k_9^{\text{on}}=1.0 \cdot 10^7$ | $k_9^{\text{off}}=2.5 \cdot 10^{-2}$ | a |
| Factors IXa | $E_9$, $P_9$ | $E_9^m$ | $k_9^{\text{on}}=1.0 \cdot 10^7$ | $k_9^{\text{off}}=2.5 \cdot 10^{-2}$ | a |
| Factors IXa | $E_9$, $P_9^*$ | $E_9^{m,*}$ | $k_9^{\text{on}}=1.0 \cdot 10^7$ | $k_9^{\text{off}}=2.5 \cdot 10^{-2}$ | b |
| Factors X | $Z_{10}$, $P_{10}$ | $Z_{10}^m$ | $k_{10}^{\text{on}}=1.0 \cdot 10^7$ | $k_{10}^{\text{off}}=2.5 \cdot 10^{-2}$ | a |
| Factors Xa | $E_{10}$, $P_{10}$ | $E_{10}^m$ | $k_{10}^{\text{on}}=1.0 \cdot 10^7$ | $k_{10}^{\text{off}}=2.5 \cdot 10^{-2}$ | a |
| Factors V | $Z_5$, $P_5$ | $Z_5^m$ | $k_5^{\text{on}}=5.7 \cdot 10^7$ | $k_5^{\text{off}}=0.17$ | c |
| Factors Va | $E_5$, $P_5$ | $E_5^m$ | $k_5^{\text{on}}=5.7 \cdot 10^7$ | $k_5^{\text{off}}=0.17$ | c |
| Factors VIII | $Z_8$, $P_8$ | $Z_8^m$ | $k_8^{\text{on}}=5.0 \cdot 10^7$ | $k_8^{\text{off}}=0.17$ | d |
| Factors VIIIa | $E_8$, $P_8$ | $E_8^m$ | $k_8^{\text{on}}=5.0 \cdot 10^7$ | $k_8^{\text{off}}=0.17$ | d |
| Factors II | $Z_2$, $P_2$ | $Z_2^m$ | $k_2^{\text{on}}=1.0 \cdot 10^7$ | $k_2^{\text{off}}=5.9$ | e |
| Factors IIa | $E_2$, $P_2$ | $E_2$ | $k_2^{\text{on}}=1.0 \cdot 10^7$ | $k_2^{\text{off}}=5.9$ | e |

**Table A.6**. Reactions of platelet surfaces. (a) $k^{\text{cat}}_{z_5^m:e_{10}^m} = 0.046$ sec$^{-1}$ and $K_M = 10.4 \cdot 10^{-9}$ M [48]. (b) The rate constants for thrombin activation of fV on platelets are assumed to be the same as in plasma. (c) $k^{\text{cat}}_{z_8^m:e_{10}^m} = 0.023$ sec$^{-1}$ and $K_M = 2.0 \cdot 10^{-8}$ M [42]. (d) The rate constants for thrombin activation of fVIII on platelets are assumed to be the same as in plasma. (e) The formation of the tenase and prothrombinase complexes is assumed to be very fast with $K_d = 1.0 \cdot 10^{-10}$ M [43]. (f) $k^{\text{cat}}_{z_{10}^m:ten} = 20$ sec$^{-1}$ and $K_M = 1.6 \cdot 10^{-7}$ M [60]. (g) $k^{\text{cat}}_{z_2^m:pro} = 30$ sec$^{-1}$ and $K_M = 3.0 \cdot 10^{-7}$ M [55].

| Reaction | Reactants | Complex | Product | $\text{M}^{-1}\text{sec}^{-1}$ | $\text{sec}^{-1}$ | $\text{sec}^{-1}$ | Note |
|---|---|---|---|---|---|---|---|
| Activation (of-,by-) | | | | | | | |
| (V,Xa) | $Z_5^m$, $E_{10}^m$ | $Z_5^m : E_{10}^m$ | $E_5^m$ | $k^+_{z_5^m:e_{10}^m}$=$1.0 \cdot 10^8$ | $k^-_{z_5^m:e_{10}^m}$=1.0 | $k^{\text{cat}}_{z_5^m:e_{10}^m}$=$4.6 \cdot 10^{-2}$ | a |
| (V,IIa) | $Z_5^m$, $E_2^m$ | $Z_5^m : E_2^m$ | $E_5^m$ | $k^+_{z_5^m:e_2^m}$=$1.73 \cdot 10^7$ | $k^-_{z_5^m:e_2^m}$=1.0 | $k^{\text{cat}}_{z_5^m:e_2^m}$= 0.23 | b |
| (VIII,Xa) | $Z_8^m$, $E_{10}^m$ | $Z_8^m : E_{10}^m$ | $E_8^m$ | $k^+_{z_8^m:e_{10}^m}$=$5.1 \cdot 10^7$ | $k^-_{z_8^m:e_{10}^m}$=1.0 | $k^{\text{cat}}_{z_8^m:e_{10}^m}$=$2.3 \cdot 10^{-2}$ | c |
| (VIII,IIa) | $Z_8^m$, $E_2^m$ | $Z_8^m : E_2^m$ | $E_8^m$ | $k^+_{z_8^m:e_2^m}$=$2.64 \cdot 10^7$ | $k^-_{z_8^m:e_2^m}$=1.0 | $k^{\text{cat}}_{z_8^m:e_2^m}$= 0.9 | d |
| (X,VIIIa:IXa) | $Z_{10}^m$, $TEN$ | $Z_{10}^m : TEN$ | $E_{10}^m$ | $k^+_{z_{10}^m:ten}$=$1.31 \cdot 10^8$ | $k^-_{z_{10}^m:ten}$=1.0 | $k^{\text{cat}}_{z_{10}^m:ten}$=20.0 | f |
| (X,VIIIa:IXa$^*$) | $Z_{10}^m$, $TEN^*$ | $Z_{10}^m : TEN^*$ | $E_{10}^m$ | $k^+_{z_{10}^m:ten}$=$1.31 \cdot 10^8$ | $k^-_{z_{10}^m:ten}$=1.0 | $k^{\text{cat}}_{z_{10}^m:ten}$=20.0 | f |
| (II,Va:Xa) | $Z_2^m$, $PRO$ | $Z_2^m : PRO$ | $E_2^m$ | $k^+_{z_2^m:pro}$= $1.03 \cdot 10^8$ | $k^-_{z_2^m:pro}$=1.0 | $k^{\text{cat}}_{z_2^m:pro}$=30.0 | g |
| Binding (-,with -) | | | | | | | |
| (IIIa,IXa) | $E_8^m$, $E_9^m$ | | $TEN$ | $k^+_{\text{ten}}$=$1.0 \cdot 10^8$ | $k^-_{\text{ten}}$=0.01 | | e |
| (VIIIa,IXa$^*$) | $E_8^m$, $E_9^{m,*}$ | | $TEN^*$ | $k^+_{\text{ten}}$= $1.0 \cdot 10^8$ | $k^-_{\text{ten}}$=0.01 | | e |
| (Va,Xa) | $E_5^m$, $E_{10}^m$ | | $PRO$ | $k^+_{\text{pro}}$=$1.0 \cdot 10^8$ | $k^-_{\text{pro}}$=0.01 | | e |

**Table A.7**. Inhibition reactions. (a) We estimate these parameters based on the half-lives of Factors IXa, Xa, IIa in plasma [63]. (b) From [33]. APC is not included in these simulations.

| Reaction | Reactants | Product | $M^{-1}sec^{-1}$ | $sec^{-1}$ | Note |
|---|---|---|---|---|---|
| Inactivation (of-,by-) | | | | | |
| (IXa,ATIII) | $E_9$ | $E_9{}^{,in}$ | | $k_9^{\text{in}}$=0.1 | a |
| (Xa,ATIII) | $E_{10}$ | $E_{10}{}^{,in}$ | | $k_{10}^{\text{in}}$=0.1 | a |
| (IIa,ATIII) | $E_2$ | $E_2{}^{,in}$ | | $k_2^{\text{in}}$=0.2 | a |
| Binding (-,with-) | | | | | |
| (TFPI,Xa) | $TFPI$,$E_{10}$ | $TFPIa$ | $k^+_{tfpia:e_{10}}=1.6\cdot10^7$ | $k^-_{tfpia:e_{10}}=3.3\cdot10^{-4}$ | b |
| ($TFPIa$,TF:VIIa) | $TFPIa$,$E_7^{se}$ | $TFPIa:E_7^{se}$ | $k^+_{tfpia:e_7^{se}}=1.0\cdot10^7$ | $k^-_{tfpia:e_7^{se}}=1.1\cdot10^{-3}$ | b |

**Table A.8**. Platelet transitions. (a) Estimated from data in [71, 73] as described in [38]. (b) Estimated from data in [23] as described in text.

| Transition | Initial State | Final State | $M^{-1}sec^{-1}$ | $sec^{-1}$ | Note |
|---|---|---|---|---|---|
| | | | | | |
| Unactivated platelet adhering to SE | $P^{m,u}$ | $P^{se,a}$ | $k_{adh}$=2 $\cdot 10^{10}$ | | a |
| Bound platelet adhering to SE | $P^{b,a}$ | $P^{se,a}$ | $k_{adh}$=2 $\cdot 10^{10}$ | | a |
| Activated platelet adhering to SE | $P^{m,u}$ | $P^{se,a}$ | $k_{adh}$=2 $\cdot 10^{10}$ | | a |
| Activated platelet cohering to bound platelet | $P^{m,a}$ | $P^{b,a}$ | | $k_{coh} \cdot P_{max} = 1 \cdot 10^4$ | |
| Platelet activation by ADP | $P^{m,u}$ | $P^{m,a}$ | | $k_{adp}^{pla}$=0.34 | b |
| Platelet activation by thrombin | $P^{m,u}$ | $P^{m,a}$ | | $k_{e_2}^{pla}$=0.50 | b |

# REFERENCES


[1] R. Adolph, D. A. Vorp, D. L. Steed, M. W. Webster, M. V. Kameneva, and S. C. Watkins, *Cellular content and permeability of intraluminal thrombus in abdominal aortic aneurysm*, J. Vasc. Surg, 25 (1997), pp. 916–926.

[2] S. S. Ahmad, R. Rawala-Sheikh, and P. N. Walsh, *Comparative interactions of Factor IX and Factor IXa with human platelets*, J. Biol. Chem., 264 (1989), pp. 3244–3251.

[3] L. Alberio and G. L. Dale, *Platelet-collagen interactions: membrane receptors and intracellular signalling pathways.*, Eur. J. Clin. Invest., 29 (1999), pp. 1066–1076.

[4] G. A. Allen, A. S. Wolberg, J. A. Oliver, M. Hoffman, H. R. Roberts, and D. M. Monroe, *Impact of procoagulant concentration on rate, peak and total thrombin in a model system*, J Thromb Haemost, 2 (2004), pp. 402–13.

[5] D. C. Altieri and T. S. Edgington, *Sequential receptor cascade for coagulation proteins on moncytes*, J. Biol. Chem., 264 (1989), pp. 2969–2972.

[6] M. Anand, K. Rajagopal, and K. Rajagopal, *A model incorporating some of the mechanical and biochemical factors underlying clot formation and dissolution in flowing blood.*, J. Theoret. Med., 5 (2003), pp. 183–218.

[7] J. B. Bell, P. Colella, and H. M. Glaz, *A second-order projection method for the incompressible Navier-Stokes equations*, J. Comput. Phys., 85 (1989), pp. 257–283.

[8] E. Beltrami and J. Jesty, *The role of membrane patch size and flow in regulating proteolytic feedback threshold on a membrane: Possible application in blood coagulation*, Mathematical Biosciences, 172 (2001), pp. 1–13.

[9] T. Bodnar and A. Sequeira, *Numerical simulation of the coagulation dynamics of blood*, Comp. and Math. Meth. in Medicine, 9 (2008), pp. 83–104.

[10] L. Brass, M. Ahuja, E. Belmonte, S. P. S, A. Tarver, and J. Hoxie, *The human platelet thrombin receptor. Turning it on and turning it off.*, Ann. N. Y. Acad. Sci., 714 (1994), pp. 1–12.

[11] W. L. Briggs, V. E. Henson, and S. F. McCormick, *A Multigrid Tutorial*, SIAM, Philadelphia, PA, 2000.

[12] D. L. Brown, R. Cortez, and M. L. Minion, *Accurate projection methods for the incompressible navier-stokes equations*, Journal of Computational Physics, 168 (2001), pp. 464–499.

[13] S. Butenas and K. G. Mann, *Kinetics of human Factor VII activation*, Biochemistry, 35 (1996), pp. 1904–1910.

[14] A. Chorin, *Numerical solutions of the navier-stokes equations*, Math. Comput., 22 (1968), pp. 745–762.

[15] A. Chorin, *On the convergence of discrete approximations to the navier-stokes equations*, Math. Comput., 23 (1969), pp. 341–353.

[16] J. W. Demmel, *Applied Numerical Linear Algega*, SIAM, Philadelphia, PA, 1997.

[17] E. C. Eckstein and F. Belgacem, *Model of platelet transport in flowing blood with drift and diffusion terms*, Biophy J, 60 (1991), pp. 53–69.

[18] E. C. Eckstein, A. W. Tilles, and F. J. Millero III, *Conditions for the occurrence of large near-wall excesses of small particles during blood flow*, Microvascular Research, 36 (1988), pp. 31–39.

[19] E. Ermakova, M. Panteleev, and E. Shnol, *Blood coagulation and propagation of autowaves in flow*, Pathophysiol Haemost Thromb, 34 (2005), pp. 135–142.

[20] A. L. Fogelson and R. D. Guy, *Platelet-wall interactions in continuum models of platelet aggregation: Formulation and numerical solution*, Mathematical Biology and Medicine, 21 (2004), pp. 293–334.

[21] ——, *Immersed-boundary-type models of intravascular platelet aggregation*, Comput Meth Appld Mech Eng, 197 (2008), pp. 2087–2104.

[22] A. L. Fogelson and N. Tania, *Coagulation under flow: The influence of flow-mediated transport on the initiation and inhibition of coagulation*, Pathophysiology of Haemostasis and Thrombosis, 34 (2005), pp. 91–108.

[23] A. R. L. Gear, *Platelet adhesion, shape change, and aggregation: rapid initiation and signal transduction events*, Can. J. Physiol. Pharmacol., 72 (1994), pp. 285–94.

[24] E. Grabowski, J. Franta, and P. Didisheim, *Platelet aggregation in flowing blood* in vitro *II. Dependence of aggregate growth rate on ADP concentration and shear rate*, Microvasc. Res., 16 (1978), pp. 183–195.

[25] R. D. Guy, *A Continuum Model of Platelet Aggregation: Closure, Computational Methods and Simulation*, PhD thesis, University of Utah, 2004.

[26] J. J. Hathcock and Y. Nemerson, *Platelet deposition inhibits tissue factor activity: In vitro clots are impermeable to Factor Xa*, Blood, 104 (2004), pp. 123–127.

[27] H. C. Hemker and H. Kessels, *Feedback mechanisms in coagulation*, Haemostasis, 21 (1991), pp. 189–196.

[28] D. C. Hill-Eubanks and P. Lollar, *von Willibrand factor is a cofactor for thrombin-catalyzed cleavage of the Factor VIII light chain*, J. Biol. Chem., 265 (1990), pp. 17854–8.

[29] M. Hockin, K. Jones, S. Everse, and K. G. Mann, *A model for the stoichiometric regulation of blood coagulation*, J. Biol. Chem., 277 (2002), pp. 18322–18333.

[30] S. P. Jackson, *The growing complexity of platelet aggregation*, Blood, 109 (2007), pp. 5087–5095.

[31] L. Jennings, *Mechanisms of platelet activation: Need for new strategies to protect against platelet-mediated atherothrombosis*, Thromb Haemost, 102 (2009), pp. 248–257.

[32] J. Jesty and Y. Nemerson, *The pathways of blood coagulation*, in Williams Hematology, E. Beutler, M. Lichtman, and B. Coller, eds., McGraw-Hill, New York, 5th ed., 1995, pp. 1227–1238.

[33] J. Jesty, T. Wun, and A. Lorenz, *Kinetics of the inhibition of Factor Xa and the Tissue Factor-Factor VIIa complex by the Tissue Factor Pathway Inhibitor in the presence and absence of heparin*, Biochemistry, 33 (1994), pp. 12686–12694.

[34] K. Jones and K. G. Mann, *A model for the Tissue Factor pathway to thrombin. II. A mathematical simulation*, J. Biol. Chem., 269 (1994), pp. 23367–73.

[35] R. Jordan, G. Oosta, W. Gardner, and R. Rosenberg, *The kinetics of hemostatic enzyme-antithrombin interactions in the presence of low molecular weight heparin.*, Journal of Biological Chemistry, 255 (1980), p. 10081.

[36] P. Kamath and S. Krishnaswamy, *Fate of membrane-bound reactants and products during the activation of human prothrombin by prothrombinase*, J. Biol. Chem., 283 (2008), pp. 30164–30173.

[37] S. Krishnaswamy, K. C. Jones, and K. G. Mann, *Prothrombinase complex assembly. Kinetic mechanism of enzyme assembly on phospholipid vesicles*, J. Biol. Chem., 263 (1988), pp. 3823–3834.

[38] A. L. Kuharsky and A. L. Fogelson, *Surface-mediated control of blood coagulation: The role of binding site densities and platelet deposition*, Biophysical Journal, 80 (2001), pp. 1050–1074.

[39] R. J. LeVeque, *High-resolution conservative algorithms for advection in incompressible flow*, SIAM J. Numer. Anal., 33 (1996), pp. 627–665.

[40] A. Lobanov and T. Starozhilova, *"the effect of convective flows on blood coagulation processes"*, Pathophysiol Haemost Thromb, 34 (2005), pp. 121–134.

[41] E. Lobanova, E. Shnol, and F. Athaullakhanov, *"complex dynamics of the formation of spatially localized standing structures in the vicinity of saddle-node bifurcations of waves in the reaction-diffusion model of blood clotting"*, Phys Rev E Stat Nonlin Soft Matter Phys., 70 (2004).

[42] P. Lollar, G. J. Knutson, and D. N. Fass, *Activation of porcine Factor VIII:C by thrombin and Factor Xa*, Biochemistry, 24 (1985), pp. 8056–8064.

[43] K. G. Mann, *The assembly of blood clotting complexes on membranes*, TIBS, 12 (1987), pp. 229–233.

[44] ——, *Prothrombin and thrombin*, in Hemostasis and Thrombosis: Basic Principles and Clinical Practice, R. Colman, J. Hirsh, V. Marder, and E. Salzman, eds., J.B. Lippincott Company, Philadelphia, PA, 3d ed., 1994, pp. 184–199.

[45] K. G. Mann, E. G. Bovill, and S. Krishnaswamy, *Surface-dependent reactions in the propagation phase of blood coagulation.*, Ann. N. Y. Acad. Sci., 614 (1991), pp. 63–75.

[46] K. G. Mann, S. Krishnaswamy, and J. H. Lawson, *Surface-dependent hemostasis*, Semin. Hematol., 29 (1992), pp. 213–26.

[47] K. G. Mann, M. E. Nesheim, W. R. Church, P. Haley, and S. Krishnaswamy, *Surface-dependent reactions of the vitamin K-dependent enzyme complexes*, Blood, 76 (1990), pp. 1–16.

[48] D. D. Monkovic and P. B. Tracy, *Activation of human Factor V by Factor Xa and thrombin*, Biochemistry, 29 (1990), p. 1118.

[49] D. D. Monkovic and P. B. Tracy, *Functional characterization of human platelet-released Factor V and its activation by Factor Xa and thrombin,*, J. Biol. Chem., 265 (1990), pp. 17132–40.

[50] D. Monroe and M. Hoffman, *What does it take to make a perfect clot?*, Arteriosclerosis, Thrombosis, and Vascular Biology, 26 (2006).

[51] D. M. Monroe, H. R. Roberts, and M. Hoffman, *Platelet procoagulant complex assembly in a a tissue factor-initiated system*, British Journal of Haematology, 88 (1994), pp. 364–371.

[52] J. H. Morrissey, *Tissue Factor modulation of Factor VIIa activity: Use in measuring trace levels of Factor VIIa in plasma,*, Thromb. Haemost., 74 (1995), pp. 185–188.

[53] Y. Nemerson, *The Tissue Factor pathway of blood coagulation*, Semin. Hematol., 29 (1992), pp. 170–176.

[54] M. E. Nesheim, D. D. Pittman, J. H. Wang, D. Slonosky, A. R. Giles, and R. J. Kaufman, *The binding of s-labeled recombinant Factor VIII to activated and unactivated human platelets*, J. Biol. Chem., 263 (1988), p. 16467.

[55] M. E. Nesheim, R. P. Tracy, P. B. Tracy, D. S. Boskovic, and K. G. Mann, *Mathematical simulation of prothrominase*, Methods Enzymol., 215 (1992), pp. 316–328.

[56] W. F. Novotny, S. Brown, J. Miletich, D. Rader, and G. Broze, *Plasma antigen levels of the lipoprotein-associated coagulation inhibitor in patient samples*, Blood, 78 (1991), pp. 387–93.

[57] U. Okorie, W. S. Denney, M. S. Chatterjee, K. B. Neeves, and S. L. Diamond, *Determination of surface tissue factor thresholds that trigger coagulation at venous and arterial shear rates: Amplification of 100 fM circulating tissue factor by flow*, Blood, 111 (2008), pp. 3507–13.

[58] C. S. Peskin, *Numerical analysis of blood flow in the heart*, J. Comput. Phys., 25 (1977), pp. 220–252.

[59] R. Peyret and T. D. Taylor, *Computational methods for fluid flow*, Springer-Verlag, New York, 1986.

[60] R. Rawala-Sheikh, S. S. Ahmad, B. Ashby, and P. N. Walsh, *Kinetics of coagulation Factor X activation by platelet-bound Factor IXa*, Biochemistry, 29 (1990), pp. 2606–11.

[61] G. Reed, M. Fitzgerald, and J. Polgar, *Molecular mechanisms of platelet exocytosis: insights into the secrete life of thrombocytes*, Blood, 96 (2000), pp. 3334–3342.

[62] H. Roberts, M. Hoffman, and D. Monroe, *A cell-based model of thrombin generation.*, in Seminars in thrombosis and hemostasis, vol. 32, GEORG THIEME VERLAG, 2006, p. 32.

[63] R. Rosenberg and K. Bauer, *The heparin-antithrombin system: A natural anticoagulant mechanism*, in Hemostasis and Thrombosis: Basic Principles and Clinical Practice, R. W. Colman, J. Hirsh, V. J. Marder, and E. W. Salzman, eds., J.B. Lippincott Company, Philadelphia, PA, 3d ed., 1994, pp. 837–860.

[64] Z. Ruggeri and C. Mendolicchio, *Adhesion mechanics in platelet function*, Circulation Research, 100 (2007), pp. 1673–1685.

[65] J. M. Scandura, S. S. Ahmad, and P. N. Walsh, *A binding site expressed on the surface of activated human platelets is shared by Factor X and prothrombin*, Biochemistry, 35 (1996), pp. 8890–902.

[66] D. M. Stern, C. Esposito, H. Gerlach, M. Gerlach, J. Ryan, D. Handley, and P. Nawroth, *Endothelium and regulation of coagulation.*, Diabetes Care, 14 (1991), pp. 160–166.

[67] G. Tangelder, H. Teirlinck, D. Slaaf, and R. Reneman, *Distribution of blood platelets flowing in arterioles*, American Journal of Physiology, 248 (1985), pp. H318–312.

[68] A. W. Tilles and E. C. Eckstein, *The near-wall excess of platelet-sized particles in blood flow: Its dependence on hematocrit and wall shear rate*, Microvasc. Res., 33 (1987), p. 211.

[69] P. B. Tracy, L. L. Eide, and K. G. Mann, *Human prohrombinase complex assembly and function on isolated peripheral blood cell populations*, J. Biol. Chem., 260 (1985), pp. 2119–2124.

[70] U. Trottenberg, A. Schuller, and C. Oosterlee, *Multigrid*, Academic Press, San Diego, CA, 2000.

[71] V. T. Turitto and H. R. Baumgartner, *Platelet interaction with subendothelium in flowing rabbit blood: Effect of blood shear rate*, Microvasc. Res., 17 (1979), pp. 38–54.

[72] V. T. Turitto and E. F. Leonard, *Platelet adhesion to a spinning surface*, Trans. Amer. Soc. Artif. Int. Organs, 18 (1972), pp. 348–54.

[73] V. T. Turitto, H. J. Weiss, and H. R. Baumgartner, *The effect of shear rate on platelet interaction with subendothelium exposed to citrated human blood*, Microvasc. Res., 19 (1980), pp. 352–365.

[74] V. T. Turitto, H. J. Weiss, H. R. Baumgartner, L. Badimon, and V. Fuster, *Cells and aggregates at surfaces*, 1987. Annals New York Academy of Sciences.

[75] P. N. Walsh, *Platelet-coagulant protein interactions*, in Hemostasis and Thrombosis: Basic Principles and Clinical Practice, R. W. Colman, J. Hirsh, V. J. Marder, and E. W. Salzman, eds., J.B. Lippincott Company, Philadelphia, PA, 3d ed., 1994, pp. 629–651.

[76] H. J. Weiss, *Platelet physiology and abnormalities of platelet function (Part 1)*, New Engl. J. Med., 293 (1975), pp. 531–541.

[77] Z. Xu, N. Chen, M. Kamocka, E. Rosen, and M. Alber, *A multiscale model of thrombus development*, J R Soc Interface, 5 (2008), pp. 705–722.

[78] Z. Xu, N. Chen, S. Shadden, J. Marsden, M. Kamocka, E. Rosen, and M. Alber, *A multiscale model of thrombus development*, Soft Matter, 5 (2009), pp. 769–779.

[79] C. Yeh, A. Calvez, and E. Eckstein, *An estimated shape function for drift in a platelet-transport model*, Biophysical Journal, 67 (1994), pp. 1252–1259.

[80] M. Young, P. Carroad, and R. Bell, *Estimation of diffusion coefficients of proteins*, Biotech. and Bioeng., 22 (1980), pp. 947–955.

[81] V. Zarnitsina, F. Ataullakhanov, A. Lobanov, and O. Morozova, *Dynamics of spatially nonuniform patterning in the model of blood coagulation*, Chaos, 11 (2001), pp. 57–70.